2015

Fabrication and Characterization of Anode-Supported Micro-Tubular Solide Oxide Fuel Cell by Phase Inversion Method

Cong Ren
University of South Carolina - Columbia

FABRICATION AND CHARACTERIZATION OF ANODE-SUPPORTED MICRO-TUBULAR SOLIDE OXIDE FUEL CELL BY PHASE INVERSION METHOD

By

Cong Ren

Bachelor of Engineering
Hefei University of Technology, 2008

Master of Engineering
University of Science and Technology of China, 2011

Submitted in Partial Fulfillment of the Requirements

For the degree of Doctor of Philosophy in

Mechanical Engineering

College of Engineering and Computing

University of South Carolina

2015

Accepted by:

Fanglin (Frank) Chen, Major Professor

Kenneth Reifsnider, Committee Member

Kevin Huang, Committee Member

Qian Wang, Committee Member

Lacy Ford, Vice Provost and Dean of Graduate Studies

ACKNOWLEDGEMENTS

I would like to thank my advisor, Dr. Fanglin (Frank) Chen for his guide, encouragement, patience and support. I would also like to convey my sincerest appreciation to my thesis committee, Dr. Kenneth Reifsnider, Dr. Kevin Huang, and Dr. Qian Wang, for their invaluable advice and continuous help during my Ph.D study.

Specially, I would like to thank Dr. Tong Liu, Dr. Yanxiang Zhang and Dr. Ye Lin for their help on my research. I would also like to thank my colleagues from Dr. Frank Chen's group, Dr. Shumin Fang, Dr. Yu Chen, Dr. Guoliang Xiao, Dr. Yao Wang, Dr. Lei Zhang, Dr. Chenghao Yang, Dr. Zhibin Yang, Dr. Qiang Liu, Dr. Xihui Dong, Dr. Siwei Wang, Libin Lei, and other friends in the Horizon Building.

Finally, I would like to express my great gratitude to my parents for their selfless support and endless love.

ABSTRACT

Nowadays, the micro-tubular solid oxide fuel cells (MT-SOFCs), especially the anode supported MT-SOFCs have been extensively developed to be applied for SOFC stacks designation, which can be potentially used for portable power sources and vehicle power supply. To prepare MT-SOFCs with high electrochemical performance, one of the main strategies is to optimize the microstructure of the anode support. Recently, a novel phase inversion method has been applied to prepare the anode support with a unique asymmetrical microstructure, which can improve the electrochemical performance of the MT-SOFCs. Since several process parameters of the phase inversion method can influence the pore formation mechanism and final microstructure, it is essential and necessary to systematically investigate the relationship between phase inversion process parameters and final microstructure of the anode supports. The objective of this study is aiming at correlating the process parameters and microstructure and further preparing MT-SOFCs with enhanced electrochemical performance.

Non-solvent, which is used to trigger the phase separation process, can significantly influence the microstructure of the anode support fabricated by phase inversion method. To investigate the mechanism of non-solvent affecting the microstructure, water and

ethanol/water mixture were selected for the NiO-YSZ anode supports fabrication. The presence of ethanol in non-solvent can inhibit the growth of the finger-like pores in the tubes. With the increasing of the ethanol concentration in the non-solvent, a relatively dense layer can be observed both in the outside and inside of the tubes. The mechanism of pores growth and morphology obtained by using non-solvent with high concentration ethanol was explained based on the inter-diffusivity between solvent and non-solvent. Solvent and non-solvent pair with larger D_m value is benefit for the growth of finger-like pores. Three cells with different anode geometries was prepared, $La_{0.85}Sr_{0.15}MnO_3$ (LSM) was selected as the cathode. Cells were tested at 800^oC using humidified H_2 as fuel. Cell with anode prepared by using pure water as non-solvent shows a maximum power density up to 437mW/cm^2. By comparing the anode geometry and electrochemical performance, it indicated that microstructure with longer finger-like pores and thinner macrovoid free layer close to the inner side of the tube is benefit to cell performance.

Another factor that can affect the microstructure of anode support is the ratio of solvent and polymer binder. In this research, anode-supported MT-SOFCs have been fabricated by phase inversion method. The effect of the viscosity of the casting slurry on the microstructure of YSZ-NiO anode support has been investigated. The microstructure of the YSZ-NiO support can be effectively controlled by varying the slurry composition with different solvent and polymer binder content. Gas permeation and mechanical strength of the YSZ-NiO support have been measured and four YSZ-NiO anode supports have been chosen for subsequent cell fabrication. The effective conductivity of the different anode supports has been measured at room temperature after reduced. Anode-supported single cells with YSZ electrolyte and LSM/YSZ cathode are fabricated

and tested. Maximum cell power densities of 606 $mWcm^{-2}$, 449 $mWcm^{-2}$, 339 $mWcm^{-2}$ and 253 $mWcm^{-2}$ have been obtained respectively at 750 ^{o}C with humidified hydrogen as fuel and ambient air as oxidant. The correlation between the cell electrochemical performance and anode microstructures has been discussed.

Adjusting the slurry composition by introducing additive is also an effective approach to tailor the microstructure of the anode support. Poly(ethylene glycol) (PEG), which is a common applied polymer additive, was selected to fabricate the YSZ-NiO anode supports. The effect of molecular weight and amount of PEG additive on the thermodynamics of the casting solutions was characterized by measuring the coagulation value. Viscosity of the casting slurries was also measured and the influence of PEG additive on viscosity was studied and discussed. The presence of PEG in the casting slurry can greatly influence the final anode support microstructure. Based on the microstructure result and the measured gas permeation value, two anode supports were selected for cell fabrication. For cell with the anode support fabricated using slurry with PEG additive, a maximum cell power density of 704 $mWcm^{-2}$ is obtained at 750 ^{o}C with humidified hydrogen as fuel and ambient air as oxidant; cell fabricated without any PEG additive shows the peak cell power density of 331 $mWcm^{-2}$. The relationship between anode microstructure and cell performance was discussed.

Anode-supported micro-tubular solid oxide fuel cells (MT-SOFCs) based on $BaZr_{0.1}Ce_{0.7}Y_{0.1}Yb_{0.1}O_{3-\delta}$ (BZCYYb) proton-conducting electrolyte have been prepared using a phase inversion method. Three sulfur-free polymer binder candidates ethyl cellulose (EC), polyvinylidene fluoride (PVDF), polyetherimide (PEI) and sulfur-containing polythersulfone (PESf) were used as polymer binders to fabricate

NiO-BZCYYb anode. The overall influence of polymer binder on the anode supports was evaluated. Sulfide impurity generated from PESf was revealed by XRD and X-ray photoelectron spectroscopy (XPS). The difference in the anode microstructure for samples fabricated by different polymer binders was examined by scanning electron microscope (SEM) and analyzed by measuring the gas permeation data of the reduced samples. Single cells based on different anode supports were characterized in anode-supported MT-SOFCs with the cell configuration of Ni-BZCYYb anode, BZCYYb electrolyte and $La_{0.6}Sr_{0.4}Co_{0.2}Fe_{0.8}O_{3-\delta}$ (LSCF)-BZCYYb cathode at 650 ^{o}C using hydrogen as fuel and ambient air as oxidant. MT-SOFCs of the anode fabricated using PEI show maximum power density of 0.45 Wcm^{-2} compared with 0.35 Wcm^{-2} for cells fabricated with PESf. The difference in cell performance was attributed to the phase purity of the anode fabricated by different polymer binders. Sulfur-free polymer binder PEI exhibits advantages over the commonly applied PESf and other sulfur-free polymer binder candidates.

To eliminate the skin layer formed close to the inner side of the tubular sample when using the phase inversion method. Polyethersulfone (PESf)-polyethylenimine (PEI) blend was employed as the polymer binder to fabricate the micro-tubular solid oxide fuel cells (MT-SOFCs). The potential impurity introduced in the anode support by the polymer binder was examined by XPS and the resulting novel microstructure was analyzed based on the backscattered electron (BSE) images. Cells fabricated with blend polymer binder showed significantly enhanced power output compared with those cells only fabricated with PEI or PESf. The improved cell performance demonstrated that using blend polymer as binder is a promising and versatile approach for MT-SOFC fabrication via phase

inversion method.

Finally, to investigate the effect of the anode microstructure on the total cell performance, two types of anode support with different microstructure were prepared via the phase inversion method at different temperature. Cells fabricated based on these two anode supports were tested at 750 ^{o}C with hydrogen or hydrogen mixture with fuel gas. The measured current density-voltage (I-V) curves were fitted by a polarization model, and several parameters were archived through the modeling process. The influence of the anode support on the total cell performance was discussed based on the calculated result.

TABLE OF CONTENTS

LIST OF TABLES

LIST OF FIGURES

CHAPTER 1 INTRODUCTION

Nowadays, the primary power supply of the world heavily depends on the nonrenewable fossil fuels such as coal, oil and nature gas. However, on one hand the environmental crisis that will be generated from the traditional usage of the fossil fuels and on the other fossil fuels will eventually be depleted. Therefore, exploring renewable and environmentally friendly alternative power sources has been an urgent issue. In recent decades, solid oxide fuel cells (SOFCs) have attract many attentions and been regarded as a promising next generation power source due to their high energy conversion efficiency, low emission and fuel flexibility [1].

1.1 BACKGROUND OF SOLID OXIDE FUEL CELLS

The solid oxide fuel cells (SOFCs) are energy conversion devices that can convert the chemical energy of the fuel gas to electrical energy. Figure 1.1 shows the schematic of the oxygen ion conducting SOFC work principle with hydrogen as fuel and oxygen as the oxidant.

The two porous electrodes are separated by the dense electrolyte layer and the overall reaction of hydrogen and oxygen is divided into two half reactions. The half reactions at each electrode are

$$\frac{1}{2}O_2 + 2e^- \rightarrow O^{2-}(Cathode) \quad (1.1)$$

$$H_2 + O^{2-} \rightarrow H_2O + 2e^-(Anode) \quad (1.2)$$

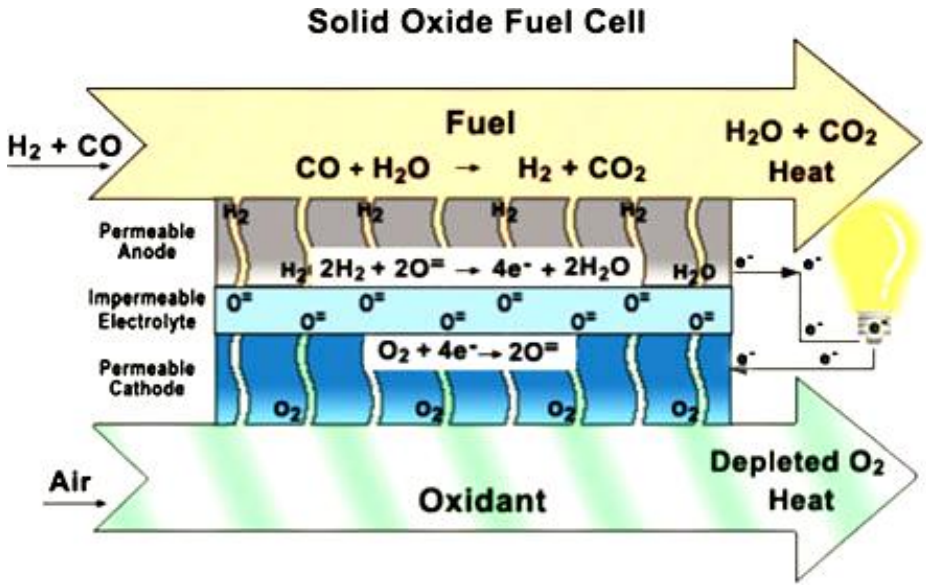

Figure 1.1 Working principle of SOFC [2]

At the cathode side, the oxygen molecular combines two electrons coming from the external circuit and is reduced to oxygen ions. Meanwhile, at the anode side, the hydrogen reacts with the oxygen ions diffusing through the electrolyte to generate water and release electrons to the external circuit.

Depending on the different ambient operating conditions of each part of the SOFC, the requirements of the materials of electrolyte, cathode, and anode are different. For the electrolyte, besides that it should provide high oxygen ion conductivity, it should also show good chemical stability in both oxidizing and reducing atmosphere. The fluorite-structured yttria-stabilized zirconia (YSZ) and cerium based oxide have been widely applied for the electrolyte fabrication [3, 4]. Recently the perovskite structured lanthanum gallate based oxide, especially the lanthanum strontium gallium magnesium

(LSGM) has also been developed for the fabrication of SOFC running at lower temperature (below 700 ^{o}C) [5, 6]. The cathode of SOFC operates in oxidizing atmosphere; high electronic conductivity as well as oxygen ion conductivity is required for the cathode materials. Moreover, the chemical stability, catalytic activity and thermal compatibility with the electrolyte should also be considered. The typical cathode materials include strontium doped lanthanum manganite (LSM) [7] and lanthanum strontium cobaltite ferrite (LSCF) [8]. For the anode material, it should be stable in reducing atmosphere; the high electronic and oxygen ion conductivity and good catalytic activity are also required. Metal anode has been developed at the early stage of SOFCs, while the poor thermal capability with ceramic electrolyte limits its further utilization. Nowadays, nickel oxide (NiO)-YSZ composite anode has been the most common used anode for the SOFCs. The existing of ceramic YSZ in NiO can enhance the oxygen conductivity of anode and improve the connection between anode and electrolyte. Recently, perovskite structured ceramic anode such as $La_{1-x}Sr_xCrO_3$ and $La_{0.75}Sr_{0.25}Cr_{0.5}Mn_{0.5}O_3$, have also been developed for SOFC running with hydrocarbon or sulfur containing fuels [9].

As one of the main configurations of the SOFCs, the tubular was first developed in 1960 and commercialized in 1970 by Westinghouse [10]. This designation improves the problem of sealing and the weakness of suffering with thermal shock, when comparing with the planar SOFC. However, the slower start-up and lower volume power density are still the bottle-neck for this technology. To better solve these problems, in 1990s, K. Kendall proposed the micro-tubular SOFCs (MT-SOFCs) strategy [11]. The tubular supports are on the scale of millimeters and show the enhanced power density and

thermal tolerance properties.

For the single MT-SOFCs fabrication, three types of MT-SOFC were designed, the electrolyte supported, cathode supported and the anode supported. The schematic of electrolyte and anode supported MT-SOFCs were shown in Figure 1.2. Among these designations, the electrolyte and cathode supported MT-SOFCs were not popular investigated, due to their low performance [12, 13]. While for the anode supported MT-SOFCs, the thinner electrolyte and the lower polarization resistance enable them to be a promising candidate for the commercialization of SOFC.

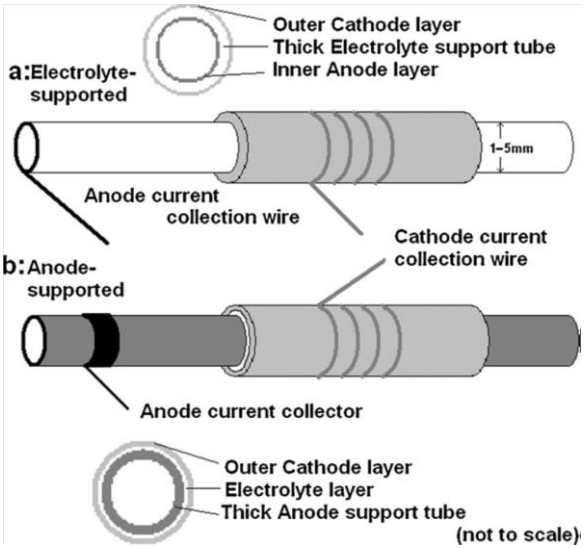

Figure 1.2 Basic micro-tubular fuel cell designs [14]

1.2 PERFORMANCE OF THE SOFCS

1.2.1 Theoretical voltage

The voltage of the SOFC is resulted from the difference of oxygen partial pressure between the cathode and anode, the value of the theoretical voltage can be calculated by the Wagner equation:

$$E = \frac{RT}{4F}\int_{P'_{O_2}}^{P''_{O_2}} t_i d\ln P_{O_2} \quad (1.3)$$

$$t_i = \frac{R_e}{R_i + R_e} \quad (1.4)$$

Where R_i and R_e are the ionic resistance and the electronic resistance of the electrolyte, respectively. The P'_{O2} and P''_{O2} represent the oxygen partial pressure of the cathode and anode side, F is the Faraday constant. When t_i equal to 1, the equation can be simplified as the Nernst equation:

$$E = \frac{RT}{4F} \ln \frac{P'_{O_2}}{P''_{O_2}} \quad (1.5)$$

According to the Nernst equation, the value of the theoretical voltage is determined by the thermodynamic parameters such as oxygen partial pressure and temperature.

1.2.2 Polarization loss

There are three types of polarization loss of the SOFCs, the ohmic polarization, concentration polarization and activation polarization. The ohmic polarization is generated by the transportation of ions through the cell components and their interfaces. It can be described as the equation:

$$\eta_{ohm} = (\rho_e l_e + \rho_c l_c + \rho_a l_a + R_{contact}) i \quad (1.6)$$

Where the ρ_e, ρ_c and ρ_a are the resistivity of electrolyte, cathode and anode, l_e, l_c and l_a are the thickness of the electrolyte, cathode and anode. $R_{contact}$ represents the overall contact potential of the SOFC. Normally, the ohmic polarization resulting from the electrolyte accounts for the main proportion of the total value. Therefore, the SOFC with electrode supported configuration shows advantage to reduce the ohmic polarization loss, due to the thin electrolyte film.

The activation polarization is caused by the electrochemical reaction involved in the SOFC operation. Certain energy barrier should be overcome to enable the reaction to

proceed. The activation polarization is normally related with the charge transfer process including the adsorption and dissociation of the reactant and product on the electrodes as well as the diffusion of atoms to the triple phase boundaries (TPB). The relationship between activation overpotential η_A and the current density j can be described by the well-known Butler-Volmer equation:

$$j = j_o \exp\left(\frac{\alpha \eta_A z F}{RT}\right) - j_o \exp\left(-\frac{(1-\alpha)\eta_A z F}{RT}\right) \quad (1.7)$$

Where α is the charge transfer coefficient (dimensionless), j_0 is the exchange current density, z is the number of electrons involved in the electrode reaction. F, R and T are the Faraday constant, universal gas constant and temperature respectively. When the activation overpotential η_A is low enough (less than 15 mV at room temperature), the Butler-Volmer equation can be expressed as:

$$j = j_o \frac{nF\eta_A}{RT} \quad (1.8)$$

It can be seen that, under low activation polarization, the activation overpotential and the current density show the linear relation. On the other hand, when the activation overpotential is high, the Butler-Volmer equation can be simplified as the Tafel equation:

$$\eta_A = \frac{RT}{\alpha \eta F} \ln j_o + \frac{RT}{\alpha \eta F} \ln j = a + b \ln j \quad (1.9)$$

Chan *et. al.* has calculated and compared the anode and cathode activation polarization of the electrolyte-supported SOFC, the result indicates that the cathode activation polarization is much higher than the anode activation polarization [15]. Thus, the anode-supported SOFC is expected to cause lower activation polarization loss than the cathode-supported SOFC, and shows advantage for the SOFC commercialization.

For the electrode supported SOFCs, as noted above, the ohmic polarization can be significantly reduced by depositing a thin electrolyte film. Moreover, the activation polarization can also be lowered by employing the composite electrode, which can enlarge the TPB from the 2-dimensional line to 3- dimensional network. Therefore, the main contribution of the polarization loss may arise from the concentration polarization due to the thick electrode. The concentration polarization of the cathode and anode can be expressed as:

$$\eta_{conc}^{a} = \frac{RT}{2F}\ln\left(1-\frac{i}{i_{as}}\right)+\frac{RT}{2F}\ln(1+\frac{p_{H_2}i}{p_{H_2O}i_{as}})(Anode) \quad (1.10)$$

$$\eta_{conc}^{c} = -\frac{RT}{4F}\ln\left(1-\frac{i}{i_{cs}}\right)(Cathode) \quad (1.11)$$

Where R is the universal gas constant, i is the current density, i_{as} and i_{cs} are the limit current density of the anode and cathode respectively. The anode and cathode limit current density can be described as the following equations by Kim *et. al.* [16]:

$$i_{as} = \frac{2Fp_{H_2}^{o}D_{a(eff)}}{RTl_a}(Anode) \quad (1.12)$$

$$i_{cs} = \frac{4Fp_{O_2}^{o}D_{c(eff)}}{\left(\frac{p-p_{O_2}^{o}}{p}\right)RTl_c}(Cathode) \quad (1.13)$$

The $D_{a(eff)}$ and $D_{c(eff)}$ are the effective diffusion coefficient on the anode and cathode side, the l_a and l_c are the anode thickness and cathode thickness respectively. $P_{H2}{}^{o}$ is the partial pressure of hydrogen in the fuel (outside of the anode), $P_{O2}{}^{o}$ is partial pressure of oxygen in the oxidant (outside of the cathode). According to the equations, higher limit current density results in lower concentration polarization, while the limit current density is

determined by the effective diffusion coefficient of the reactant gas, which is greatly affected by the microstructure of the electrode. The effective diffusion coefficient can be calculated as

$$D_{eff} = \frac{\rho}{\tau} D \quad (1.14)$$

Where D is the diffusion coefficient of the reactant gas, and the ρ and τ represent the volume fraction porosity and the totuosity factor of the electrode [17]. Normally, due to the smaller molecular weight of the hydrogen, the binary diffusion coefficient of hydrogen and water $D_{H_2\text{-}H_2O}$ is larger than that of oxygen and nitrogen $D_{O_2\text{-}N_2}$. Therefore, anode-supported SOFC would show smaller concentration polarization loss than the cathode-supported SOFC with the identical thickness and microstructure.

By considering all the polarization loss, the typical current density- voltage curve (I-V curve) is shown in Figure 1.3. At low and high current density, the voltage loss is governed by the activation polarization and concentration polarization respectively, while the ohmic polarization results in the linear voltage drop.

As discussed above, the ohmic polarization of the SOFC can be reduced by employing the electrode-supported designation. Further, by comparing with the two types of electrode supported SOFC, the anode-supported designation exhibits merits such as low activation and concentration polarizations. Therefore, in this thesis, we focus on the fabrication of the anode supported SOFC.

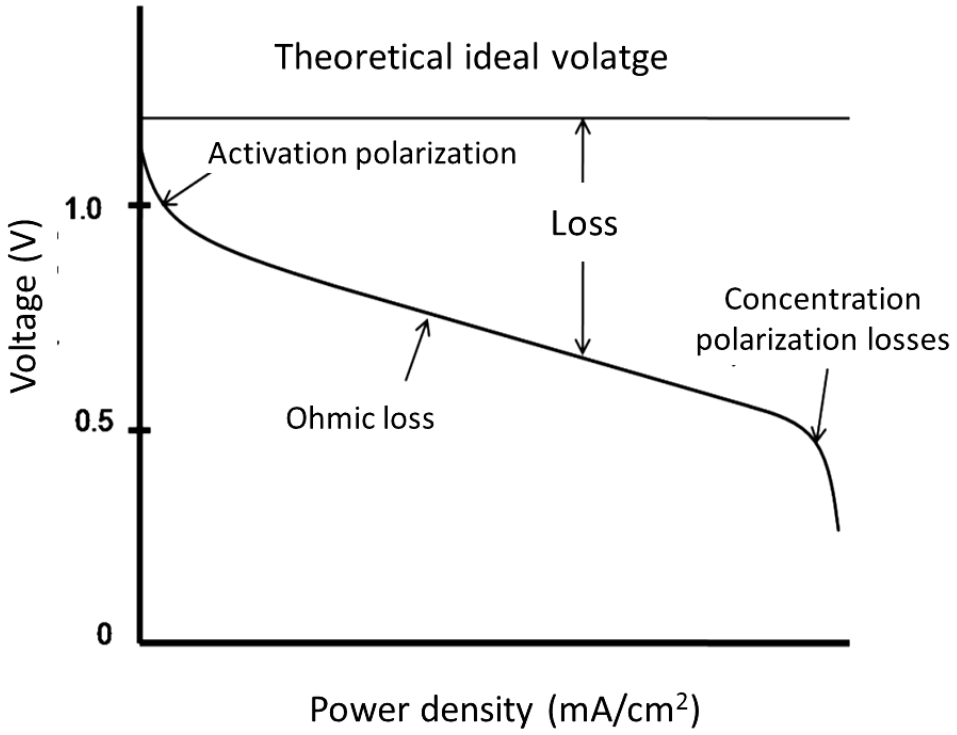

Figure 1.3 Typical polarization curve for solid oxide fuel cells [18]

1.3 PROGRESS OF THE ANODE-SUPPORTED SOFC FABRICATION

The typical electrode of SOFC is consisted of two layers: an active layer and a current collector layer which functions as the mechanical support and the gas diffusion layer [19]. Because of the different functions of the two layers, their microstructures should be different. On one hand, the active layer should be fabricated with high surface area and fine microstructure, therefore, the electrochemical active sites will be increased and the active polarization will be lowered. On the other hand, for the current collector layer, the microstructure should be coarser; it should provide enough porosity to allow the rapid diffusion of reactant and product to or out of the active layer. In Figure 1.4, it shows the cross-sectional SEM image of a typical cell.

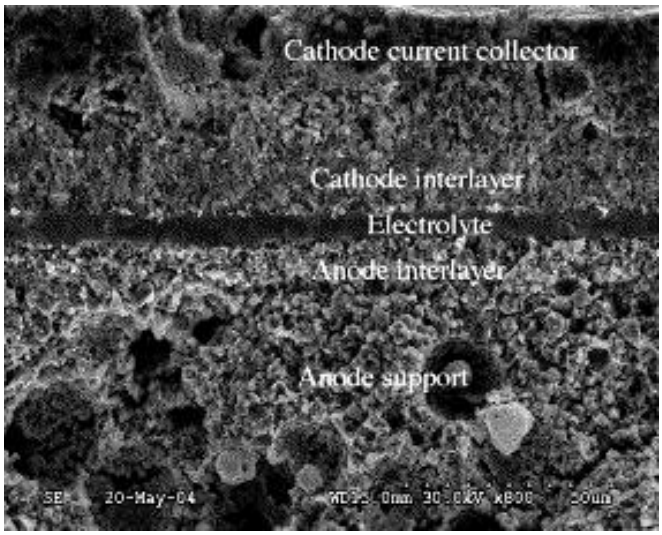

Figure 1.4 An SEM micrograph of a typical cell [19].

For the anode-supported SOFC fabrication, multilayered or graded structured anode has been adopted to meet the different microstructure requirement of the functional layer and the current collector layer. Several approaches have been developed to fabricate anode support with the heterogeneous microstructure such as uni-axially pressing [20], tape-casting [21], phase inversion [22], freeze tape casting [23] etc. Among these methods, the phase inversion can not only result in the anode support with graded microstructure but also provide an efficient way to fabricate the MT-SOFC [24], which shows higher volumetric density, fast start-up and high tolerance of thermal cycling as discussed. For this reason, the thesis is aimed at investigating the application of the phase inversion method to the anode supported MT-SOFC fabrication.

1.3.1 Brief background of phase inversion method

The phase inversion method is invented by Loeb and Sourirajan [25] and has been an efficient method to fabricate polymeric and ceramic membranes [26, 27]. Through this method, several types of microstructure can be achieved as shown in Figure 1.5.

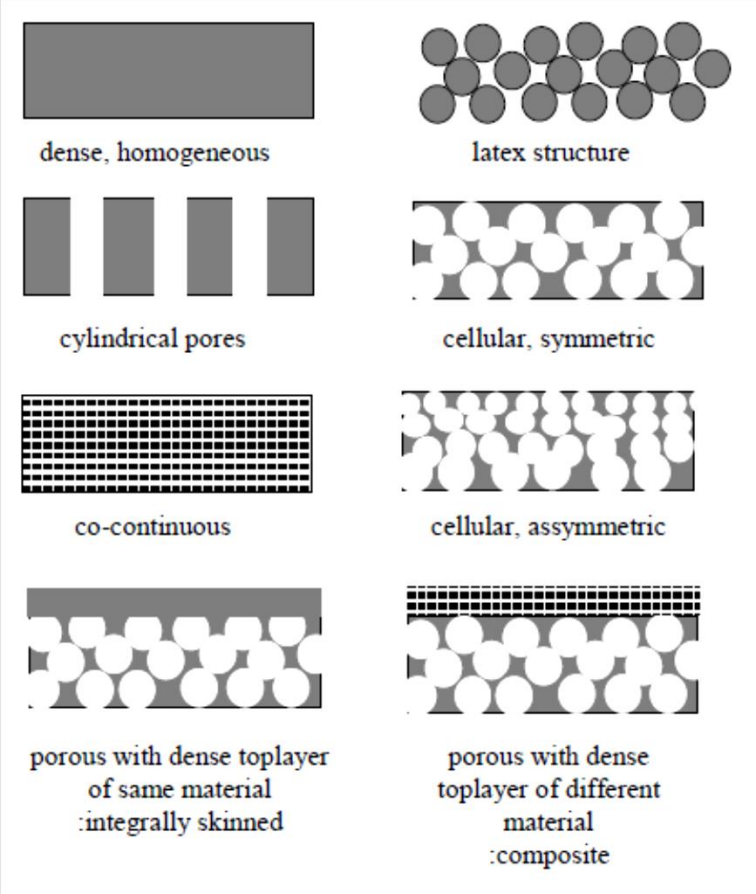

Figure 1.5 Schematic representation of different membrane morphologies [28]

According to the different way to induce the phase separation process, the phase inversion method can be categorized into four main types. (a) Thermally induced phase separation (TIPS), the phase separation is induced by the reduced solvent quantity resulting from the increased temperature. (b) Vapor phase precipitation, the phase separation is induced by the penetration of vapor non-solvent in the casting solution. (c) Air-casting of a polymer solution, the polymer binder is dissolved in a violate solvent and less violate non-solvent mixture, then with the vaporizing of the solvent, the phase separation is triggered. (d) Immersion precipitation, the prepared casing solution is immersed into non-solvent and the precipitation is induced by the interchange of solvent

and non-solvent. Figure 1.6 exhibits the schematic representation of the vapor phase precipitation, air-casting of a polymer solution and immersion precipitation process. Among the four types of phase inversion method, the immersion precipitation shows simple fabrication process and easier microstructure control, thus, it has been a popular approach for the porous membrane preparation.

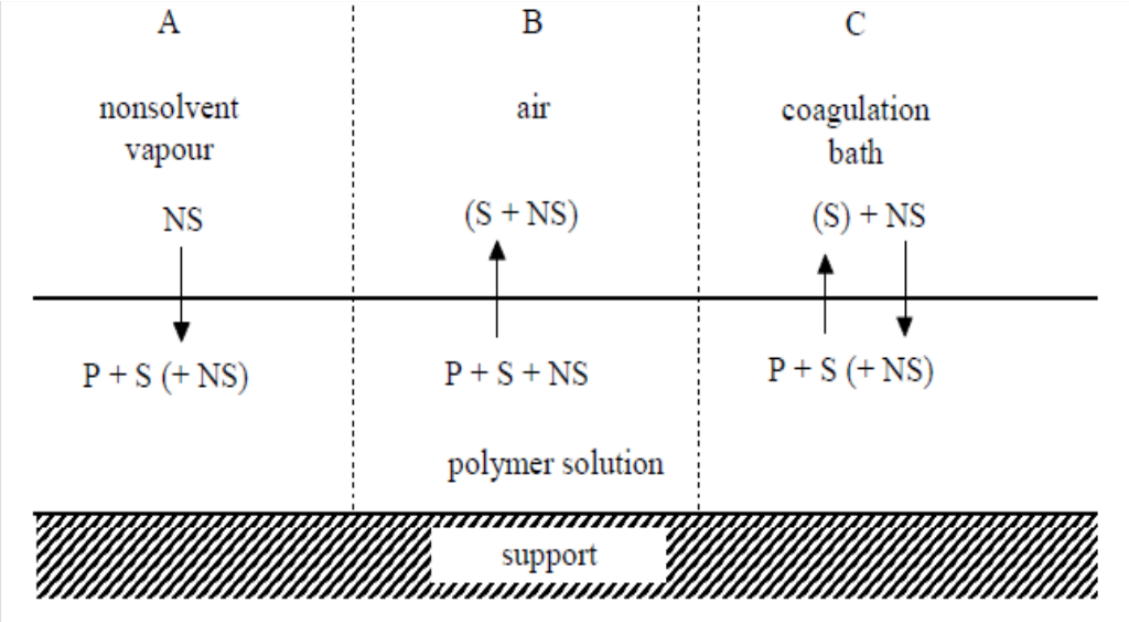

Figure 1.6 Schematic representation of the process: vapor phase precipitation (A), air-casting of a polymer solution (B) and immersion precipitation (C). P is polymer binder, S is solvent and NS represents non-solvent [28].

The microstructure of the polymeric membrane fabricated by phase inversion method can be tailored by the selection of polymer, solvent/non-solvent pair, additives, precipitation time, bath temperature and other process parameters during immersion precipitation [29-35]. For the common used polymer binders, the advantages, disadvantages and structure formula are summarized in Table 1.01. Table 1.02 gives the common used solvent/non-solvent pairs for the polymeric membrane fabrication.

Table 1.1 The common used polymers for the polymeric membrane fabrication

Polymer	Advantage	Disadvantage	Structural Formula
Cellulose Acetate(CA) [36]	• Hydrophilicity • Flexibility in fabrication • Low cost	• Low thermal resistance (<30 ℃) • Low chemical resistance, pH range (2-8) • Poor resistance to chlorine	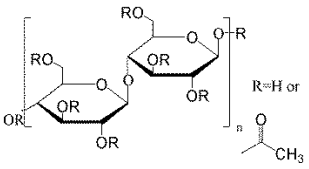
Polysulfone/ Polyethersulfone (PSf/ PESf) [37,38]	• High thermal resistance (up to 75 ℃) • Wide pH tolerances (1-13) • Good chlorine resistance • Flexibility in membrane fabrication (wide range of pore size) • High mechanical characteristics	• Low operating pressure limits • Hydrophobicity	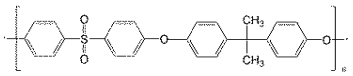 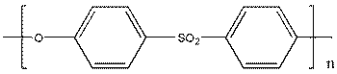
Polyvillidene Fluoride (PVDF) [39]	• High mechanical strength and chemical resistance • High thermal stability (up to 75 ℃)	• Hydrophobicity	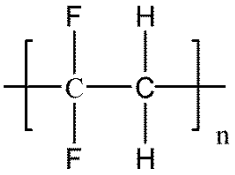
Polyamide [40]	• Wide pH tolerance • High thermal stability • High mechanical properties	• Poor chlorine resistance	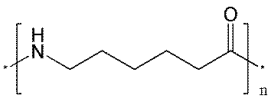

Table 1.2 The solvent/non-solvent pairs used in phase inversion method

Solvent	Non-solvent	Membrane microstructure
Dimethyl sulfoxide (DMSO)[41]	H_2O	Porous skin, macrovoids sublayer
N,N-dimethylacetamide (DMAc)[42]	H_2O	Porous skin, macrovoids sublayer
N,N-dimethylformamide (DMF)[43]	H_2O	Porous skin, macrovoids sublayer
1- methyl-2-pyrrolidone (NMP)[44]	H_2O	Porous skin, macrovoids sublayer
Dioxane[45]	H_2O	Porous skin, macrovoids sublayer
NMP[46]	Methanol, Ethanol, 2-Propanol	Porous skin, macrovoids sublayer
Acetic acid[47]	H_2O	Nonporous skin，cellular sublayer
Triethyl phosphate (TEP)[48]	H_2O	Nonporous skin，cellular sublayer
Tetrahydrofuran (THF)[47]	H_2O	Nonporous skin，cellular sublayer
Acetone[49]	H_2O, Ethanol	Nonporous skin，cellular sublayer
DMAc[46]	Methanol, Ethanol, 2-Propanol, 1-Propanol	Nonporous skin，cellular sublayer
Dichloromethane [50]	Methanol, Ethanol, 2-Propanol	Nonporous skin，cellular sublayer
Triehloroethylene [51]	Methanol, Ethanol, 2-Propanol	Nonporous skin，cellular sublayer
Chloroform[52]	Methanol, Ethanol, 2-Propanol	Nonporous skin，cellular sublayer

1.3.2 Application of phase inversion in MT-SOFC fabrication

Comparing with the conventional plastic extrusion method which was developed by Suzuki *et. al.* [53], through the phase inversion method, anode support with unique asymmetrical microstructure can be prepared. Yang *et al.* [54] fabricated the Ni-YSZ

anode support and investigated the properties such as microstructure, mechanical strength and the electrical conductivity. Later, Yang *et al.* [55] successfully prepared the Ni-YSZ anode supported MT-SOFC by using the phase inversion method. The peak power density of 0.38 Wcm^{-2} was achieved at 800 ^{o}C with LSM-YSZ cathode, the microstructure of the MT-SOFC is shown in Figure 1.7.

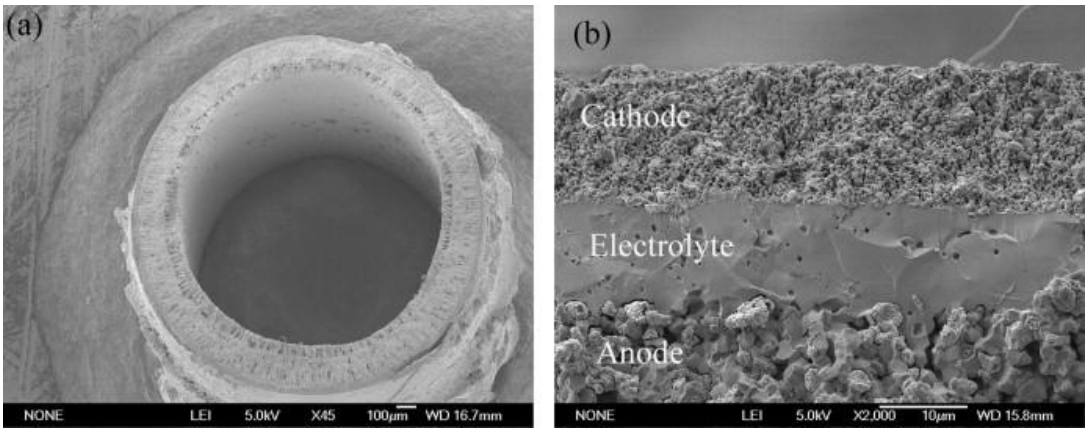

Figure 1.7 The cross-section SEM image of the MT-SOFC fabricated by phase inversion method [55]

To improve the relatively low power density of the MT-SOFC fabricated by phase inversion method, many efforts have been made. Zhang *et al.* employed the $(Pr_{0.5}Nd_{0.5})_{0.7}Sr_{0.3}MnO_{3-\delta}$-YSZ (PNSM-YSZ) [56] and $(La_{0.75}Sr_{0.25})_{0.95}Cr_{0.5}Mn_{0.5}O_3$-$Sm_{0.2}Ce_{0.8}O_{1.9}$-YSZ [57] composite cathode instead of the LSM-YSZ composite cathode and increased the peak power density to 0.48 Wcm^{-2} at 800 ^{o}C. Yang [24] enhanced the power density to 0.78Wcm^{-2} at 800 ^{o}C by infiltrating GDC nano particles in the cathode. Apart from the cathode modification works mentioned above, Zhou [58] employed the NMP as the internal coagulants and prepared anode support with gradient finger-like pores, as shown in Figure 1.8. The electrochemical performance of the MT-SOFC was improved to 0.71Wcm^{-2} at 800 ^{o}C with LSM-YSZ composite cathode.

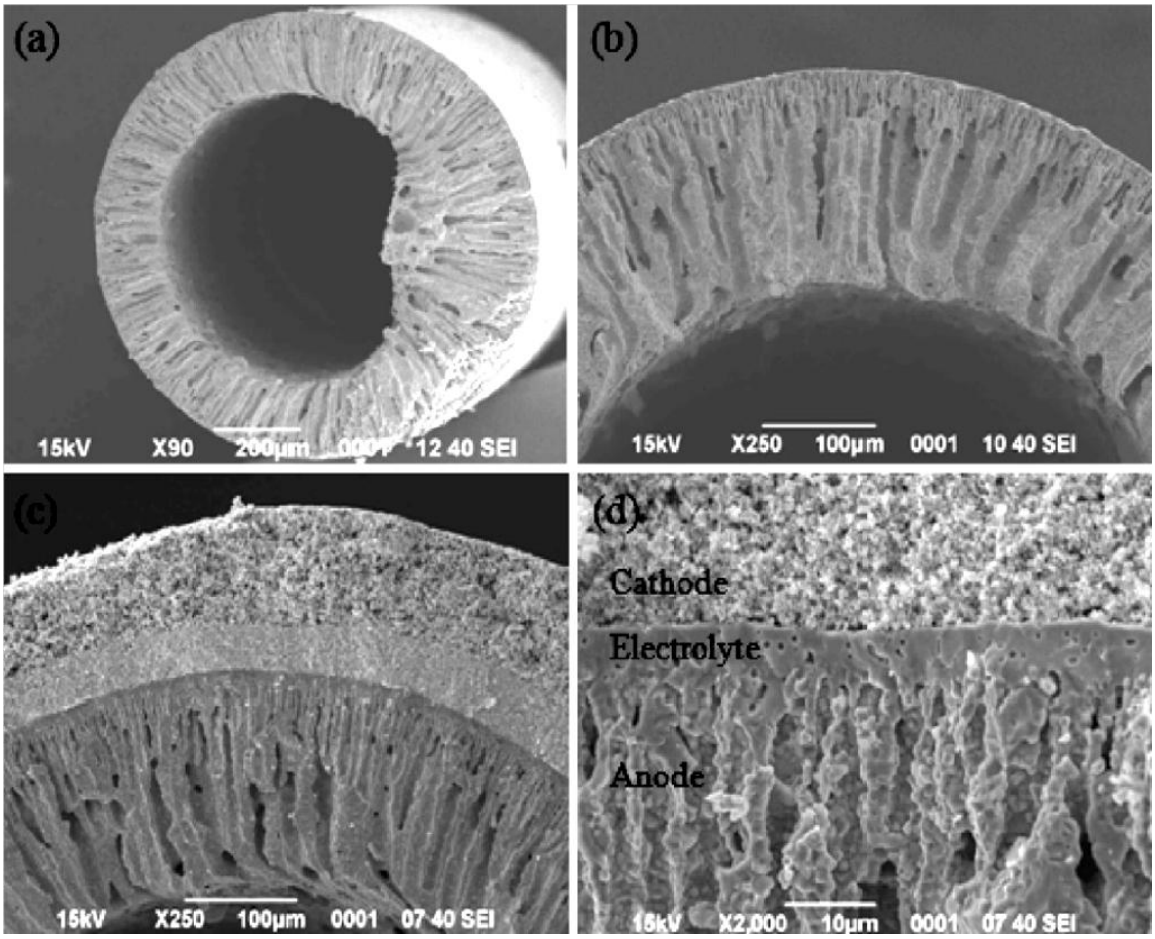

Figure 1.8 The cross-section SEM image of the MT-SOFC fabricated by phase inversion method using NMP as internal coagulant. [58]

Thereafter, Othman *et al.* [59] developed the phase inversion-based extrusion technique to prepare dual layer hollow fiber (CGO electrolyte and Ni-CGO anode) through one step extrusion. Through the co-extrusion method, the cell performance was significantly improved to 2.32 Wcm^{-2} at 650 ^{o}C. The fresh prepared dual layer tubes can be seen in Figure 1.9. Moreover, Peng [60] *et al.* adopted the U-shaped design of the MT-SOFC based on the Ni-YSZ anode support fabricated by phase inversion method, they claim that the U-shaped design can provide excellent thermal cycling performance, even after 64 times thermal cycles, there is no significantly degradation observed.

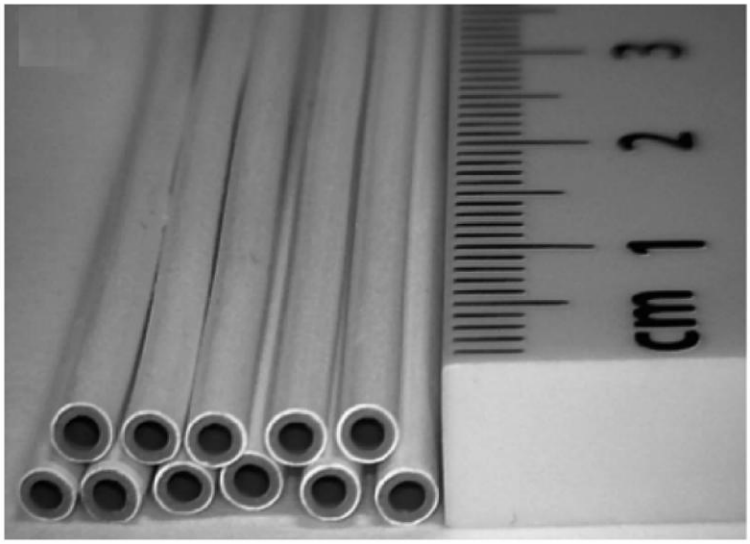

Figure 1.9 The fresh prepared Ni-GDC dual layer tubes fabricated by the phase inversion-based co-extrusion technique [59]

1.4 OBJECTIVE AND STRUCTURE OF THIS PROPOSAL

From what has been discussed above, the performance of the anode supported MT-SOFC is significantly affected by the microstructure of the anode, which can influence the activation and concentration polarizations. Anode support with graded microstructure is expected to facilitate the fuel gas transportation and increase the active sites for the anodic electrochemical reaction; therefore, the performance of the MT-SOFC can be improved. Based on the phase inversion method, which is regarded as an efficient approach for the fabrication of graded structured anode support, we reveal the influence of the process parameters on the anode support microstructure and further improve the performance of the MT-SOFC by optimizing the anode microstructure.

In chapter 2, effect of the non-solvent in external coagulant on the microstructure has been investigated and discussed. The influence of non-solvent is explained mainly based on the inter-diffusivity between solvent and non-solvent. In chapter 3, the influence of casting slurry composition on the microstructure of NiO-YSZ anode support has been

systematically investigated, the ratio of solvent and polymer binder content in the casting slurry was optimized and the electrochemical performance of the cells has been enhanced. In chapter 4, poly(ethylene glycol) (PEG) was introduced in the casting slurry as the polymer additive to modify the microstructure of the anode support. The effect of PEG molecule weight and amount in the casting slurry on the microstructure was investigated in terms of both thermodynamics and kinetics. In chapter 5, proton conducting MT-SOFC was fabricated by using novel polymer binder polyetherimide (PEI) instead of the conventional employed polyethersulfone (PESf). The microstructure and phase composition of the anode support were investigated and the result of cell performance was discussed. In chapter 6, PESf-PEI polymer blend was employed as the polymer binder to fabricate anode supported for MT-SOFC, anode with continuously graded microstructure was prepared. A convenient method to eliminate the skin layer close to the inner side of the tubular sample was developed.

CHAPTER2 INVESTIGATING THE EFFECT OF NON-SOLVENT ON THE MICROSTRUCTURE OF THE NiO-YSZ ANODE SUPPORTED MICROTUBULAR SOFC

2. 1 BACKGROUND

There are two major configurations of solid oxide fuel cells (SOFCs), planar and tubular. Compared with conventional planar SOFCs, tubular SOFCs, especially the micro-tubular SOFCs (MT-SOFCs) show high volumetric density, fast start-up and better tolerance to thermal cycling [61-63]. Tubular anode of conventional anode-supported MT-SOFCs could be fabricated by the extrusion method. However, using this method the microstructure is significantly influenced by the slurry composition and only anode microstructure with uniform porous can be obtained [64]. Recently, the phase inversion which was initially developed by Loeb and Sourirajan for organic membrane preparation [25] was introduced for ceramic membrane fabrication [65, 66]. Through phase inversion process, a unique asymmetric membrane with small pores and finger-like pores can be prepared. Since the anode microstructure is a key factor for electrochemical performance of SOFCs [67] and anode with gradient porosity can favor the cell performance [21], the phase inversion method should be a promising way for anode support fabrication.

Both of planar and tubular anode-supporting SOFCs have been fabricated by phase inversion method [22, 68]. To further modify the anode microstructure, the influence of fabrication parameters on microstructure was investigated. Employing mixture external coagulants was one of the common used strategies to modify the microstructure by phase inversion method. However, the mechanism of the pore formation when using mixture coagulant is still a controversial issue. Jin [22] correlated the microstructure and the non-solvent composition by the solubility criterion which is based on the interaction between solvent and non-solvent. On the other hand, Deshmukh and Li [26] indicated that the solvent and non-solvent interaction was not suitable to explain system with progressive reduction of precipitation rate, by investigating the PVDF-DMAc system, they reached the conclusion that the mass transfer between solvent and non-solvent was the dominate factor to control the pore formation. Thus, for the PESf-NMP system, which is common used for ceramic fabrication, determining the phase separation mechanism when applying mixture external coagulant had been an essential issue.

In this chapter, phase inversion method was employed for the NiO-YSZ hollow fibers fabricated. The formation mechanism of different microstructures was studied and proposed to be mainly based on the inter-diffusivity between solvent and non-solvent. Furthermore, anode-supported MT-SOFCs with different geometries were fabricated and tested. The relationship between anode microstructure and electrochemical performance was also discussed.

2.2 EXPERIMENTAL

2.2.1. Preparation of NiO-YSZ support and tubular cell

NiO-YSZ anodes were fabricated by the phase inversion process. To prepare NiO-YSZ

slurry, polyethersulfone (PESf, Ameco Performance Radel A-300) and 1-methyl-2 pyrrolidone (NMP, HPLC grade, Sigma-Aldrich) were mixed in the weight ratio of 1 to 3 to form a transparent polymer solution. The grinded mixture of nickel oxide (NiO, Sigma-Aldrich, USA) and yttria-stabilized Zirconia (YSZ, 8 mol% Y_2O_3, Tosoh) powders was added into this premixed solution to make a slurry suspension. Then the slurry was subjected to a ball-milling process to make a uniform and stable suspension. Details of tube fabrication processes had been described in the literature [69]. The phase separation was triggered by immersing casting slurry into different non-solvent, the precipitation time was 20 min, and then the solidified NiO-YSZ green tube samples were dried and pre-sintered at 1200^{o}C for 2 hours to obtain enough mechanical strength. In this work, pure water and different composition of water-ethanol mixture were chosen as the non-solvent. To prepare YSZ electrolyte layers on pre-sintered NiO-YSZ tubes, the tubes were dipped into suspensions of YSZ, dried and subsequently sintered at 1500 ^{o}C for 5h to form dense YSZ films. YSZ and $La_{0.85}Sr_{0.15}MnO_3$ (LSM) composite cathode (weight ratio of 50:50) were fabricated on the prepared electrolyte by brush print and then sintered at 1100 ^{o}C for 2 hours. Silver paste was printed on the surface of cathode as the current collector.

2.2.2 Characterization method

Microstructure of the prepared NiO-YSZ anode support was examined by using scanning electron microscopy (SEM, FEI Quanta 200). Single cell performance was tested with humidified H_2 (3 vol% H_2O) at a flow rate of 40 SCCM as fuel, then ambient air as the oxidant for cathode. The electrochemical impedance spectra (EIS) and I-V curve were obtained by VersaStudio electrochemistry analyzer. EIS was measured with

an AC amplitude of 10 mV and frequency range from 100 KHz to 0.1 Hz.

2. 3 RESULT AND DISCUSSION

2.3.1 Morphology study of NiO-YSZ anode support

In phase inversion process, the non-solvent exerts significant effect on the microstructure of the electrode and subsequent cell performance as well. In this work, pure water and different volume mixtures of ethanol and water were employed as non-solvents. The ethanol to water volume ratios for the non-solvent system was chosen as 20%, 50% and 80%. Figure 2.1 shows the effect of non-solvent on the microstructures of NiO-YSZ anodes. When pure water was used as the non-solvent, pore size change with gradient can be observed (Figure 2.1(a)). Close to the inner side of the tube, finger-like pores have a larger diameter while at the outer side of the tube; the diameter of pores becomes smaller. Due to the depletion of solvent in the bottom of casting slurry [70], a condense inner layer was inevitably present as shown in Figure 2.1 (a). When ethanol-water mixture was chosen, with the increase of ethanol volume in the mixture, the circular conformations of the tubular structure were deformed (Figure 2.1 (b) to (d)) as evidenced from deviation from circular structure. At lower alcohol volume ratios (20%), the overall structures of the two samples (Figure 2.1 (b) to Figure 2.1 (d)) resemble to that using water as non-solvent. At higher volume ratios, besides deformations, the inevitable condensed layers became thicker with the increase of alcohol volumes. In addition, the layers consisted of finger-like pores within the anode turned out to be less prominent and the length of finger-like pores reduced.

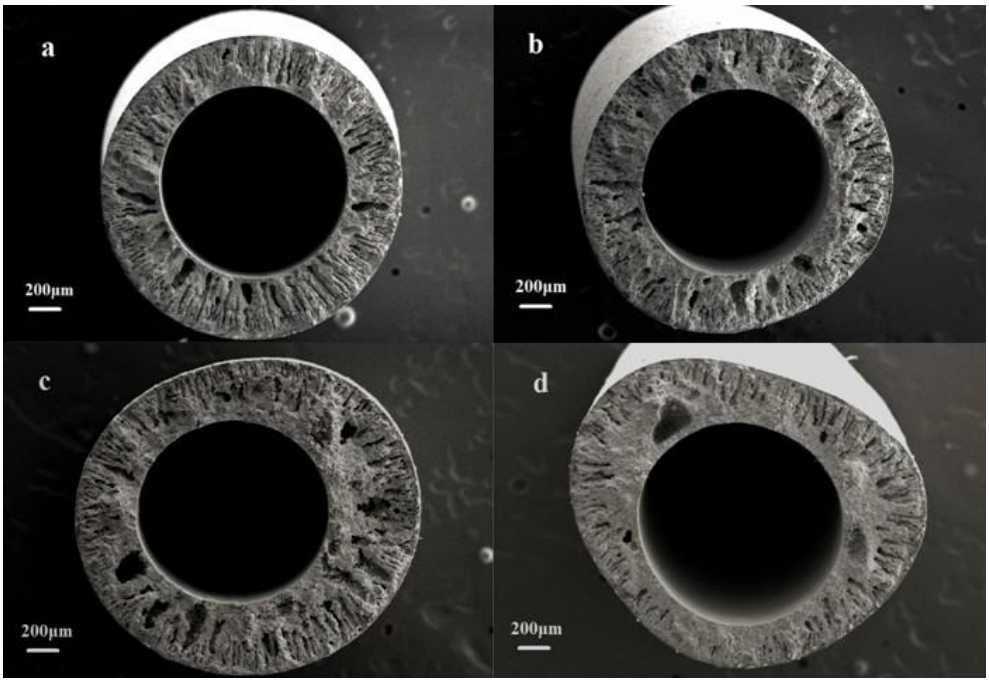

Figure 2.1 Microstructure of NiO-YSZ hollow fiber fabricated with non-solvent composed of (a) pure water, (b) 20% ethanol: 80%water, (c) 50% ethanol: 50%water, (d) 80% ethanol: 20%water.

The above experimental results suggest that mixture with high ethanol content is not a good choice as non-solvent in the phase inversion process to make microtubular NiO-YSZ anode-support SOFCs because both deformation and poor porous structure would deteriorate the cell performance. For the same reason, the 80vol% ethanol sample is not under further investigation.

2.3.2 Influence of non-solvent on microstructure

Bottino *et al.* [48] indicated that many mechanisms can be applied to explain the phase inversion process, depending on their correlated specific fabrication parameters. While in practical system, a few or just one parameters will control the process, thus different system should be explained by different mechanism. Solubility difference between them is an important criterion for the microstructure predication, when considering the interaction between the solvent and non-solvent. So *et al.* [71] studied the effect of

different solvent on microstructure by using water as non-solvent, they concluded that the higher solubility of solvent the higher the water content in the membrane (higher porosity). Therefore, in most cases, smaller solubility difference between solvent and water will favor the tendency of solvent and water mixing and benefit the pore formation. In this work, solubility difference of the selected solvent and non-solvent pair can be calculated by the reported method [22] and the result is shown in Table 2.1. It can be seen that with the increase of ethanol in the non-solvent, the solubility difference decreased, it means that there is higher tendency for NMP and ethanol to mix with each other and it will benefit the pore formation. This explanation obviously conflicts with the result observed in Figure 2.1.

Table 2.1 Differences of solubility parameters of NMP solvent and the different non-solvent

Non-solvent	Solubility parameter ($\sqrt{\sum(\Delta\delta)^2}$) $MPa^{1/2}$
H_2O	35.4
20% ETOH	30.46
50%ETOH	23.7
80%ETOH	17.05

Previously, Deshmukh and Li [26] studied the influence of different ethanol containing non-solvent on microstructure in the PVDF system; they claimed that mass transfer between solvent and non-solvent is also an essential factor for pore formation. Thus in present system, we turn to investigate the influence of mass transfer between solvent and non-solvent, the inter-diffusivity between NMP, pure water and ethanol was estimated by Tyn and Calus method [72] as the following equation:

$$D_{AB} = 8.93\times10^{-8}\frac{V_B^{0.267}}{V_A^{0.433}}\cdot\frac{T}{\eta_B}\left(\frac{\delta_B}{\delta_A}\right)^{0.15} \quad (2.1)$$

where D_{AB} is the diffusivity when A diffuses into B, V_i represents the molar volume at

normal boiling point of solution *i*, η_i represents the viscosity of solution *i*, δ_i is the surface tension of solution *i*, and *T* is the temperature. The calculated result is shown in Table 2.2.

Table 2.2 Diffusion coefficients of NMP and ethanol

Diffusion Coefficient	**D ×10^{-6} (cm^2/s)**
$D_{NMP\text{-}water}$	8.04
$D_{NMP\text{-}ethanol}$	8.51
$D_{water\text{-}NMP}$	14.8
$D_{ethanol\text{-}NMP}$	10.76

It can be seen that $D_{NMP\text{-}water}$ and $D_{NMP\text{-}ethanol}$ are comparatively close to each other and $D_{water\text{-}NMP}$ is larger than $D_{ethanol\text{-}NMP}$, which means the rate of NMP diffusing into water is close to that diffusing into ethanol, and the rate which water diffusing into the casting solution is faster than ethanol. Reuvers et al [49] indicated that the precipitation process can be categorized into two types. One is delayed demixing, in which a relatively small inflow of non-solvent diffuses into the casting solution. The other is instantaneous demixing, if the amount of non-solvent diffusing into casting solution is larger. Comparing the calculated $D_{water\text{-}NMP}$ and $D_{ehtanol\text{-}NMP}$, it can be expected that water is inclined to start an instantaneous demixing, while water-ethanol mixtures might take the delayed demixing process. Thus, immediately after the casting solution immersed into the water, precipitation is triggered and finger-like pores are formed. While for ethanol mixture, precipitation will be detained due to the relative slow diffusion of non-solvent into casting solution. An amount of solvent diffused into the non-solvent bath while no sufficient non-solvent diffuses back into the casting solution, so the localized concentration of polymer will increase and the casting solution will be solidified, for this reason, a dense layer will firstly formed. This dense top layer, as a evidence for delayed demixing, can be observed from Figure 2.2 (b) to Figure 2.2 (d), which are fabricated with 20 vol% , 50 vol% and 80 vol% ethanol mixture respectively, and sample fabricated

with pure water (Figure 2.1 (a)) shows a different porous top layer. According to the diffusion-controlled model [70], the formed dense layer will increase the barrier for inter-diffusion between solvent and non-solvent, so the precipitation rate is further reduced and the formation of finger-like pores is inhibited. As the evidence shown in Figure 2.1, samples fabricated with ethanol mixture have a decreased length of finger-like pores than which was fabricated by pure water. Moreover, change of the diffusion rate between solvent and non-solvent will result in collapsed membrane and eventually cause the shape deformation, which can also be observed from Figure 2.1 (c) to Figure 2.1 (d).

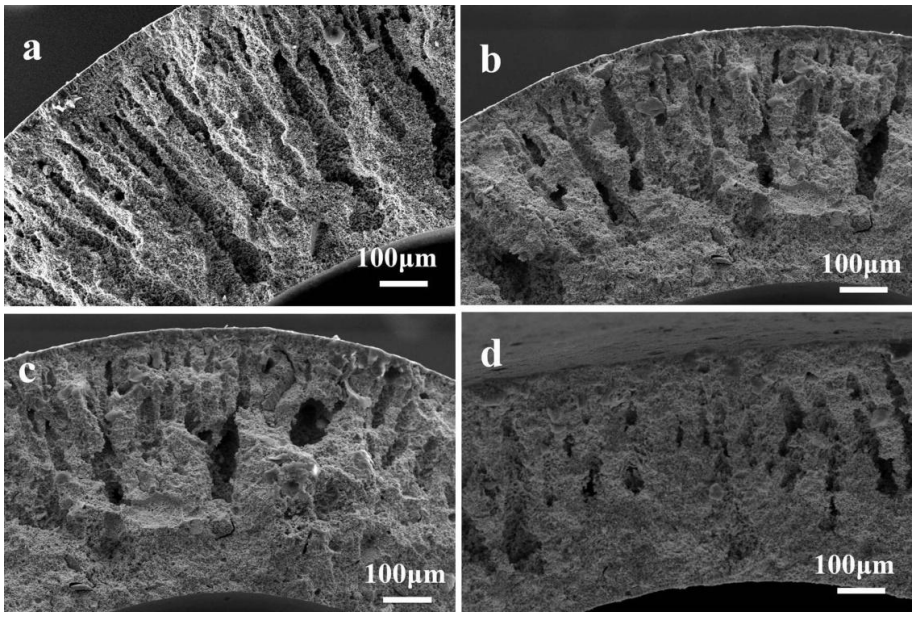

Figure 2.2 Microstructure of YSZ-NiO hollow fiber fabricated with non-solvent composed of (a) pure water, (b) 20% ethanol: 80% water, (c) 50% ethanol: 50% water.

Base on inter-diffusion, Bottino *et al.* [48] suggested introducing the harmonic mean value $D_m=2D_{s\text{-}n}D_{n\text{-}s}/(D_{s\text{-}n}+D_{n\text{-}s})$ between $D_{s\text{-}n}$ and $D_{n\text{-}s}$ to describe the inter-diffusion, where $D_{s\text{-}n}$ is the diffusivity when solvent diffuses into non-solvent and $D_{n\text{-}s}$ is the diffusivity when non-solvent diffuses into solvent. The calculated result is shown in Table 2.3, harmonic mean values of pure water and ethanol can be obtained, and the result is shown in Table 2.3. According to the result discussed above, it can be concluded that in

present system, solvent and non-solvent pair with larger D_m is more beneficial for finger-like pores formation.

Table 2.3 Harmonic mean diffusivity of water and ethanol

D_M	D $\times 10^{-6}$ (cm^2/s)
$D_{M\text{-}water}$	10.41
$D_{M\text{-}ethanol}$	9.50

2.3.3 Electrochemical performance study of NiO-YSZ anode support MT-SOFCs

Three types of MT-SOFCs were fabricated with anode support by using pure water, 20vol% ethanol-water mixture and 50vol% ethanol-water mixture then they were denoted as cell-a, cell-b and cell-c respectively. Tubes prepared with high ethanol content mixture was not chosen for cell fabrication due to the compressed cross-sectional shape. Figure 2.3 is the cross section of cell-a, cell-b and cell-c after tested, anode with gradient finger-like pores can be observed that is similar with the result reported previously [24], and macrovoid free layer close to the inner side of the tubes can be observed from cell-b and cell-c.

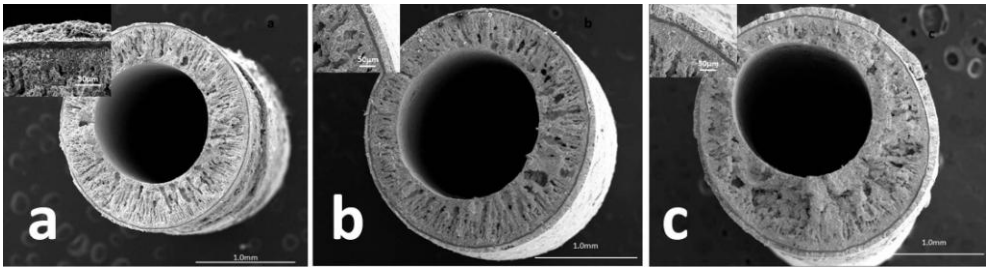

Figure 2.3 Cross-sectional SEM image of the cell-a (a), cell-b (b) and cell-c (c)

Figure 2.4 shows the different electrochemical performance of cell-a, cell-b and cell-c tested at 800 ^{o}C. The open circuit voltages (OCV) of cell-a, cell-b and cell-c are 1.02V, 1.03V and 1.06V respectively. The OCV difference between the three cells has a direct relevance to the electrolyte condition. As described in papers reported [22], anode

substrate surface with low porosity is benefit for electrolyte coating, according to the results shown in Figure 2.3(a) and Figure 2.3(b), anode for cell-c fabrication has less porous surface and it's the ideal condition to fabricate thicker and denser YSZ electrolyte by dip-coating method. At the same testing temperature, cell-a shows the best performance, the peak power density of 437 mW/cm^2, cell-b has the peak power density of 372 mW/cm^2 and cell-c is 292 mW/cm^2.

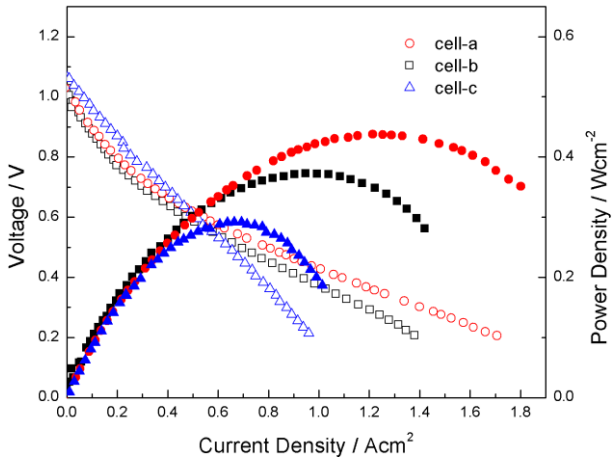

Figure 2.4 I-V curve and I-P curve of three types of cells with different anode structures, using 3% H_2O hydrogen as fuel and ambient air as oxidant at 800^{o}C.

It can be observed in Figure 2.1 and Figure 2.4, anode support prepared by pure water for cell-a fabrication have a longer finger-like pores than other anode supports used for cell-b and cell-c fabrication and anode support fabricated by using pure water shows the thinnest macrovoid free layer on the inner side. According the work published [59], finger-like pores presented in anode can act like microchannels that are beneficial to fuel gas mixture and can lower the impedance caused by gas diffusion, and then adequate fuel gas can be supplied to the functional layer where anodic reaction is occurred. On the other hand, the macrovoid-free layer formed close to the inner side of the tube will hinder the fuel gas diffusing from the gas stream into the anode. Take both of these geometry

factors into consideration, with the same cathode and electrolyte condition, anode prepared with pure water is benefit for cell fabrication. Figure 2.5 shows the polarization resistance, ohimc resistance and total resistance of different cells, cell-a has the smallest polarization resistance comparing with the other two cells, as described above, this result can be attributed to the more efficiently gas diffusion.

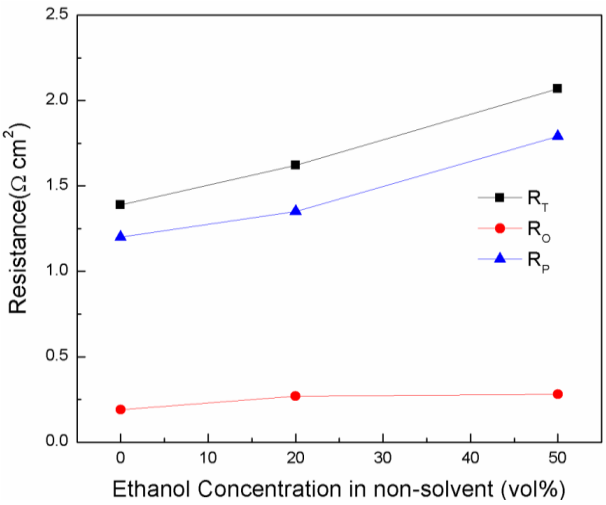

Figure 2.5 Total polarization and ohmic resistance (R_T, R_P and R_O) of three cells with different anode structures using hydrogen (3Vol% H_2O) as fuel and ambient air as oxidant at 800°C

2. 4 SUMMARY

Presence of ethanol in non-solvent is one of the key factors to control the geometry of the hollow fiber in PESf. Finger-like pores will be inhibited as the content of ethanol in non-solvent increasing. Good correlation between solvent inter-diffusivity and the morphology result can be observed and the growth of the finger-like pores can be controlled by the composition of non-solvents. Solvent and non-solvent pair with larger D_m value tends to increase the chance of finger-like pores formation. Three types of anode-supported MT-SOFCs are fabricated and tested corresponding to three anodes with different finger-like length. Maximum power output of 437 mW/cm^2, 372 mW/cm^2 and

291 mW/cm^2 are achieved for these three types of cells, respectively. Cell with longer finger-like pores and thinner macrovoid free layer shows better electrochemical performance.

CHAPTER 3 EFFECT OF CASTING SLURRY COMPOSITION ON ANODE SUPPORT MICROSTRUCTURE AND CELL PERFORMANCE OF MT-SOFCS BY PHASE INVERSION METHOD

3.1 BACKGROUND

Solid oxide fuel cells (SOFCs) have been regarded as promising next-generation power sources due to their high energy conversion efficiency and fuel flexibility [73-75]. Compared with conventional planar SOFCs, tubular SOFCs, especially micro-tubular SOFCs (MT-SOFCs), exhibit faster start-up, better tolerance to thermal cycling and higher volumetric power density [62, 76]. The traditional extrusion method has been the most commonly adopted technique for the fabrication of anode-supported MT-SOFCs [64]. Recently, the phase inversion method, which was initially developed for polymer membrane preparation [25], has been applied for anode-supported MT-SOFCs fabrications [24, 68, 69, 77-79]. Comparing with the conventional extrusion method, phase inversion process can produce a unique asymmetrical microstructure that consists of a top layer with homogenously distributed small pores and a sub-layer with long

finger-like pores. Othman *et al*. have concluded that the presence of finger-like pores in the anode in MT-SOFCs fabricated from the phase inversion method can function as microchannels for fuel gas transport and facilitate the fuel gas mixture inside the anode [59]. In such a case, the fuel oxidation reaction in the anode can be accelerated and the cell performance can be substantially improved. It has been reported that the anode microstructure can significantly affect the cell performance [67]. Therefore, it is crucial to study the correlation between the process parameters and the corresponding microstructure features for SOFC fabrication through the phase inversion method. Although many efforts have been done for phase inversion process parameter optimization [80-82], there is still lack of systemic investigation to reveal the correlation between the casting slurry compositions and the final sample microstructure.

In this chapter, YSZ-NiO anode supports have been prepared by phase inversion method and the microstructure was optimized by employing various casting slurry compositions. Four anode supports with different microstructure were selected for YSZ-NiO/YSZ/YSZ-LSM single cell fabrication. All of the prepared cells were tested at 750 ^{o}C with humidified hydrogen (3% H_2O) as fuel and ambient air as oxidant. The influence of solvent N-Methyl-2-pyrrolidone (NMP) and polymer binder polyethersulfone (PESf) content in the casting slurry on the microstructures was examined, and the correlation between microstructure and cell performance was discussed.

3. 2 EXPERIMENTAL

3.2.1. Fabrication of anode support and anode-supported cells

In this work, phase inversion method was employed to fabricate the anode supports of

MT-SOFCs [69]. Polyethersulfone (PESf, Radel A-300, Ameco Performance, USA) was dissolved into methyl-2-pyrrolidone (NMP, Alfa Aesar, USA) to form stable and transparent polymer solution. NiO (J.T. Baker, USA) and YSZ (TZ-8YZ, TOSOH Corporation, Japan) powders were mixed with a 6:4 weight ratio and then ball milled by a planetary ball mill (QM-3SP2 Nanjing University Instrument Plant, China) for more than 24 hours using ethanol as milling media. After drying, the prepared NiO-YSZ powder was dispersed into the binary polymer solution and also ball milled for 24 hours to form homogenous casting slurry for the subsequent phase inversion process. In this study, tap water was chosen as the external coagulant, which functioned as the non-solvent to trigger the phase separation process and the precipitation time of this experiment was controlled to 10 minutes. After the samples were solidified and dried, they were first sintered at 600 ^{o}C for 2 hours with a heating rate of 2 ^{o}C/min in order to decompose the organic compounds, and then directly heated to 1200 ^{o}C with a heating rate of 1 ^{o}C/min, with a dwelling time of 2 hours at 1200 ^{o}C. The samples were finally cooling down to room temperature at a cooling rate of 2 ^{o}C/min. Through this pre-sintering process, anode supports with adequate mechanical strength for the subsequent electrolyte fabrication process can be obtained.

Thin YSZ film was coated on the pre-sintered anode supports by a dip-coating method [24]. The YSZ/anode bilayers were also heated to 600 ^{o}C for 2 hours with a heating rate of 2 ^{o}C/min, and then sintered at 1450 ^{o}C for 5 hours with a heating rate of 1 ^{o}C/min to form the dense YSZ electrolyte. YSZ and $La_{0.7}Sr_{0.3}MnO_3$ (LSM-P, Fuelcellmaterials, USA) powders were mixed in a weight ratio of 6:4 and then ground with terpineol in an agate mortar and pestle for 2 hours to prepare the cathode paste.

Subsequently, the cathode was brush-painted on the electrolyte and fired at 1100 ^{o}C for 2 hours to obtain porous YSZ-LSM composite cathode.

3.2.2. Characterization of the anode substrate

The microstructure of the YSZ-NiO anode supports was examined by a scanning electron microscope (SEM, Zeiss Ultra plus FESEM). The viscosity η (Pa s) of different casting slurries was measured using a rheometer (DHR-3, TA Instruments, USA) at shear rate between 0.1 s^{-1} and 100 s^{-1} at room temperature (25 ^{o}C). Three-point bending test was employed using a Dynamic Mechanical Analysis machine (DMA, Q800, TA Instruments, USA) to measure the mechanical strength of the tubular samples after they were sintered at 1450 ^{o}C and then reduced at 750 ^{o}C for 5 hours [83]. The bending strength (δ_F) was calculated by the following equation:

$$\delta_F = \frac{8FLD}{\pi(D^4 - d_i^4)} \qquad (3.1)$$

Where F is the measured load (N) when fracture occurs; L, D, d_i are the length (m), outer diameter (m) and inner diameter (m) of the tubular samples, respectively. Gas permeation measurement was performed after the samples were sintered 1450 ^{o}C and reduced at 750 ^{o}C for 2 hours [84]. The effective conductivity of the reduced anode supports was measured by four probe DC method at room temperature using a digital multimeter (Keithley Instruments, USA) [54].

3.2.3 Electrochemical performance evaluation

The YSZ-NiO/YSZ/LSM-YSZ single cells were tested at 750 ^{o}C using 40 SCCM humidified hydrogen (3vol% H_2O) as fuel and ambient air as oxidant. Silver paste was applied to the electrode of cells before test, to ensure a reliable contact between silver lead wire and the electrodes. The electrical impedance spectroscopy (EIS) and

current-voltage curve (I-V curve) were measured using a multi-channel VersaSTAT (Princeton Applied Research). The EIS measurement was performed under open circuit condition and the AC amplitude was 10 mV and the frequency range was from 0.1 Hz to100 KHz.

3.3. RESULT AND DISCUSSION

3.3.1 Effect of NMP content on anode substrate microstructure

To investigate the influence of NMP content on microstructure, five different slurries were applied to fabricate the anode supports, and the detailed compositions are shown in Table 3.1, from A1 to A5. For all of these slurries, the weight ratio of solid powders to PESf was fixed to 10:1.

Table 3.1 Compositions of casting slurry for YSZ-NiO anode support fabrication.

Sample	**Solvent composition** (NMP/YSZ-NiO weight ratio)	**PESf composition** (PESf/YSZ-NiO weight ratio)
A1	5/10	1/10
A2	6.25/10	1/10
A3	7.5/10	1/10
A4	8.75/10	1/10
A5	10/10	1/10
B1	8.75/10	1.35/10
B2	8.75/10	1.65/10
B3	8.75/10	2/10

Figure 3.1 (a1) to Figure 3.1 (e1) shows the cross-sectional SEM images of the prepared samples after pre-sintered at 1200 ^{o}C for 2 hours. The result shows that

increasing the content of NMP in the casting slurry is beneficial to the pore formation process. From Figure 3.1 (a1), it can be observed that samples prepared from the A1 slurry have fairly dense microstructure with homogenously distributed small pores. When employing the A2 slurry that has higher NMP content, pores with axial orientation are formed, and thin finger-like pores can be observed in Figure 3.1 (b1). By further increasing the NMP content in the casting slurry, besides the finger-like pores, interconnected macrovoids emerge in the samples, as shown from Figure 3.1 (c1) to Figure 3.1 (d1). With the highest NMP content in the A5 slurry, the obtained samples show porous microstructure with homogenous sponge-like pores, as shown in Figure 3.1 (e1). The outer surface of the pre-sintered samples was also examined by SEM and the result is shown from Figure 3.1 (a2) to Figure 3.1 (e2). All the samples show similar morphology of the outer surface with lower porosity. For the inner surface, the microstructure is shown from Figure 3.1 (a3) to Figure 3.1 (e3), and it can be seen that the porosity of the inner surface increases with the increase of the NMP content in the slurry.

The observed evolution of pore geometry can be ascribed to the different viscosity of the casting slurries, as shown in Figure 3.2. When slurry A1 is employed to fabricate the sample, the diffusion of non-solvent into the casting slurry slows down due to the high slurry viscosity. Non-solvent introduced into the casting slurry is not enough to trigger extensive phase inversion process; as a result, the formation of nascent pore is inhibited [84]. Further increase in the NMP content in the casting slurry substantially decreases the viscosity value. Therefore, more non-solvent can diffuse into the casting slurry to start the phase separation process and a large number of nascent pores resulting from the

nucleation of polymer-poor phase are formed and subsequently enlarged [30], resulting in microstructure with finger-like pores or macrovoids. However, when excessive solvent is present in the casting slurry, such as slurry A5, substantial amount of non-solvent can easily diffuse into the casting slurry due to the reduced slurry viscosity. In such a case, new nascent pores generate in front of the previous ones, and pores that have already been formed are not able to expand and grow to the finger-like pores, eventually leading to a homogenous microstructure with sponge-like pores [30].

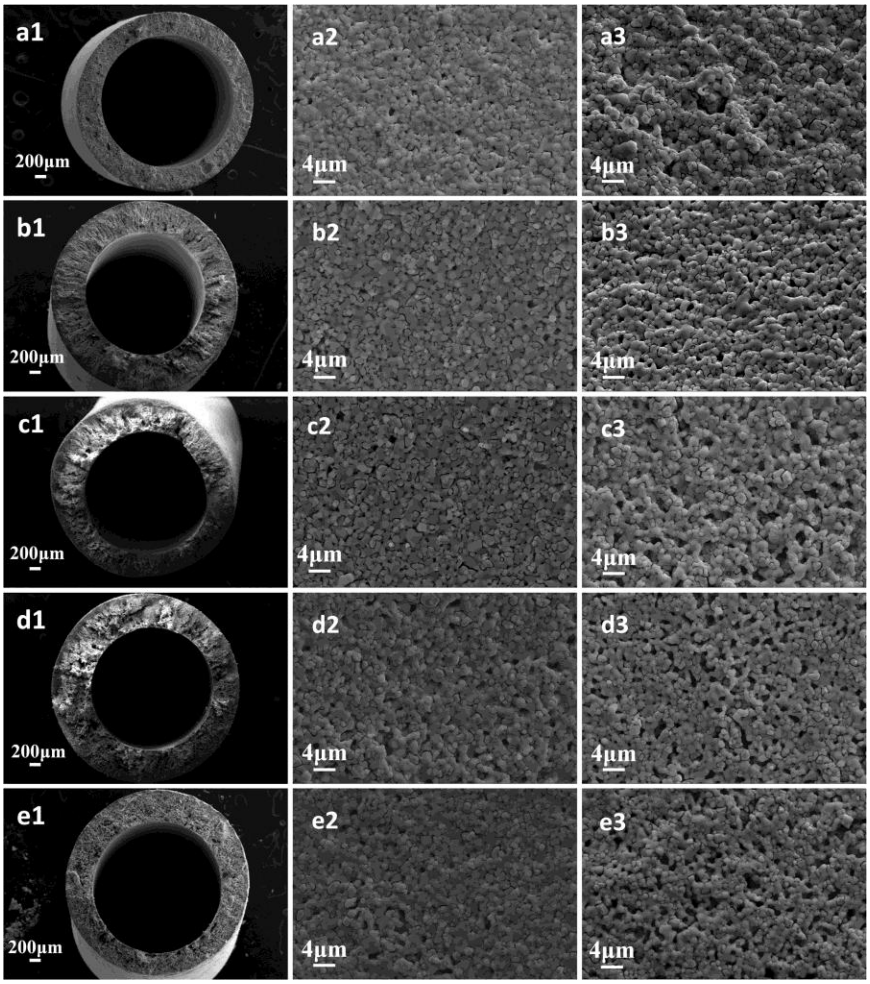

Figure 3.1 SEM micrographs of pre-sintered NiO-YSZ supports prepared by phase inversion method with slurry A1 (a), A2 (b), A3 (c), A4 (d) and A5 (e), respectively. 1, 2 and 3 denote cross-sectional, outer and inner surface microstructures, respectively.

To further characterize the prepared samples, mechanical strength and gas permeance

were measured after the YSZ-NiO support samples were sintered at 1450 ^{o}C for 5 hours and then reduced at 750 ^{o}C. Figure 3.3 shows the gas permeance result. It can be seen that samples fabricated with higher NMP content show better gas permeance performance. The gas permeation data reaches to the peak value for the anode support fabricated with the A4 slurry, but further increasing the NMP content (using the A5 slurry) leads to a slight decrease in the gas permeability. This tendency of gas permeance change correlates well with the microstructure result shown in Figure 3.1. Due to the increased porosity of the inner surface of the samples, higher NMP content in the casting slurry is beneficial for increasing the gas permeance of the prepared anode supports. However, the gas permeability of samples is determined not only by the porosity of the inner and outer surface but also by the cross-sectional microstructure. Therefore, with similar outer and inner surface morphology, samples that have macrovoids are expected to facilitate gas transport, resulting in higher gas permeation value. As shown in Figure 3.3, sample fabricated with the A5 slurry (Figure 3.1(e1)), which has the porous microstructure without macrovoids, shows relatively smaller gas permeance than sample prepared from the A4 slurry (Figure 3.1 (d1)).The mechanical property of sample A1 to sample A5 was measured by three-point bending test and the result is shown in Figure 3.4. As expected, increasing the NMP content in the casting slurry results in decreased mechanical strength. The result can be explained by the different microstructure of the samples, and samples with more porous structure tend to show lower bending strength.

From what has been discussed above, it indicates that increasing the NMP content can increase the porosity and gas permeance of the sample. However, excessive amount of NMP content results in decreased permeation value and lower mechanical strength. By

taking all the factors into consideration, to investigate the polymer content influence on the microstructure, the NMP content was fixed at the A4 slurry composition.

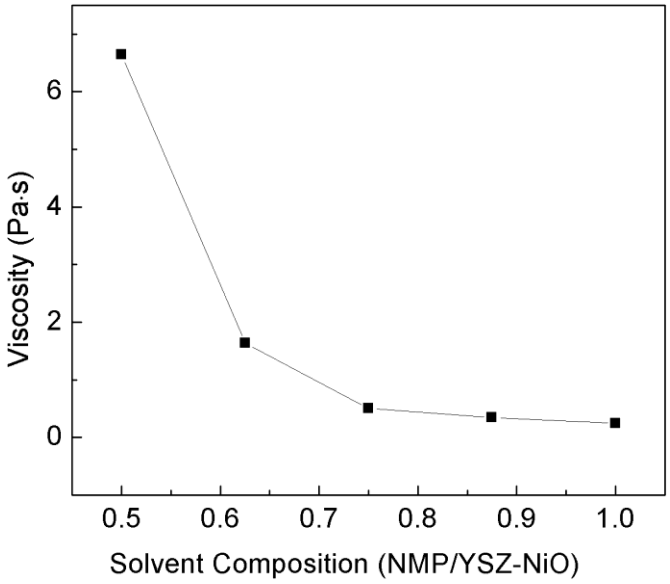

Figure 3.2 Viscosity of casting slurry prepared with different solvent composition at 25 s^{-1}.

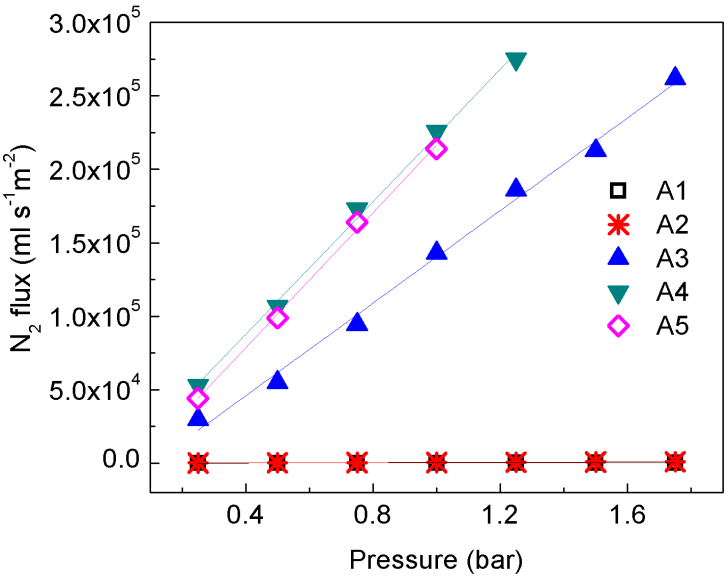

Figure 3.3 Gas permeation data for samples fabricated with different NMP content after sintered at 1450 ^{o}C and then reduced at 750 ^{o}C.

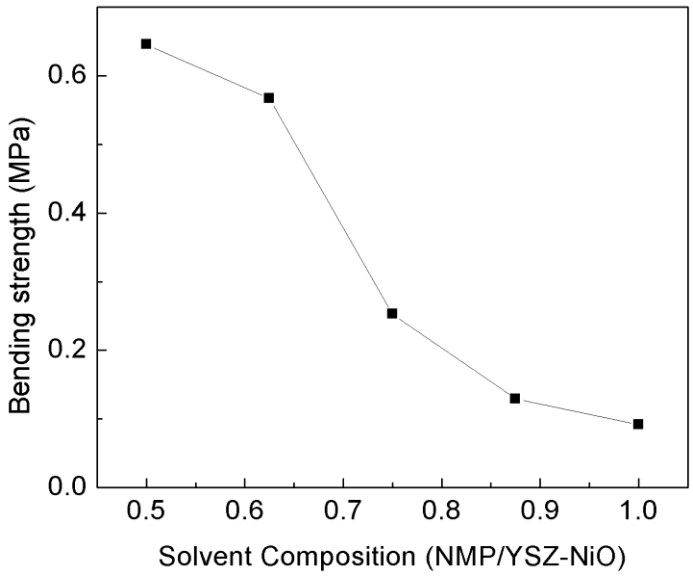

Figure 3.4 Bending strength of samples fabricated with different NMP content after sintered at 1450 ^{o}C and reduced at 750 ^{o}C.

3.3.2 Effect of PESf content on microstructure

The influence of PESf amount on microstructure was investigated by changing the PESf amount based on the A4 slurry composition; and three compositions were investigated (from B1 to B3) besides the A4 slurry. Figure 3.5 shows the microstructure of samples fabricated with different PESf content after sintered at 1200 ^{o}C for 2 hours. It can be observed from Figure 3.5 (a1) to Figure 3.5 (c1) that with the increase of the PESf concentration in the casting slurry, the microstructure of the samples changes from the interconnected macrovoids into finger-like pores with axial orientation. Furthermore, the outer layer of the tube turns to be less porous. However, when excessive PESf is added into the casting slurry, as shown in Figure 3.5 (d1), the formation of finger-like pores is inhibited, and the microstructure becomes less porous with irregular cross-section shape. This result can be explained based on the viscosity difference among the different slurries. Figure 3.6 shows the viscosity value of the casting slurries with different PESf

concentration. Slurry with higher PESf concentration has higher viscosity, and more viscous slurry will lead to slow diffusion of non-solvent into the casting slurry. In such a case, the phase separation process will be delayed and the expansion of nascent pores is also inhibited [30]. Furthermore, Barzin and Sadatnia [85] have indicated that the increased polymer concentration can also enable the gelation process to start earlier, substantially reducing the time for nascent pores to expand. Due to the above two reasons, the formation of finger-like pores is inhibited in the samples fabricated using high PESf concentration in the casting slurry. Shown in Figure 3.5 (a2) to Figure 3.5 (d2) are the outer surface SEM images of the samples fabricated with different PESf content, indicating that they have similar morphology with low porosity. The inner surface of the anode supports are shown in Figure 3.5 (a3) to Figure 3.5 (d3), porous microstructure can be seen for all the samples.

Figure 3.7 shows the gas permeation data of the tubes fabricated with different PESf concentration, indicating that increasing the PESf amount in the casting slurry, the gas permeance of the samples decreases. The gas permeation result is directly correlated to the microstructure of the tubes. Due to similar inner and outer surface morphology in all the samples with different PESf concentration, samples with axial orientation finger-like pores show higher gas permeation values. Compared with sample B1, sample B2 shows microstructure with fully-grown finger-like pores; however, as shown in Figure 3.8, sample B2 has a less porous top layer (Figure 3.8 (b)), which may interfere with gas transport and consequently affect the total gas permeance. The measured bending strength of the samples with different PESf content is shown in Figure 3.9, indicating that samples fabricated with higher PESf concentration have better mechanical strength. The

bending strength of sample B3 was not measured due to its irregular cross-sectional shape. For sample B2, though it shows the microstructure with finger-like pores, the relatively dense top layer, which can be observed in Figure 3.8(b), is beneficial to increasing the mechanical strength of the sample [86]. To summarize, increasing the PESf content in the casting slurry inhibits the formation and growth of the finger-like pores in the membrane and consequently results in a less porous microstructure.

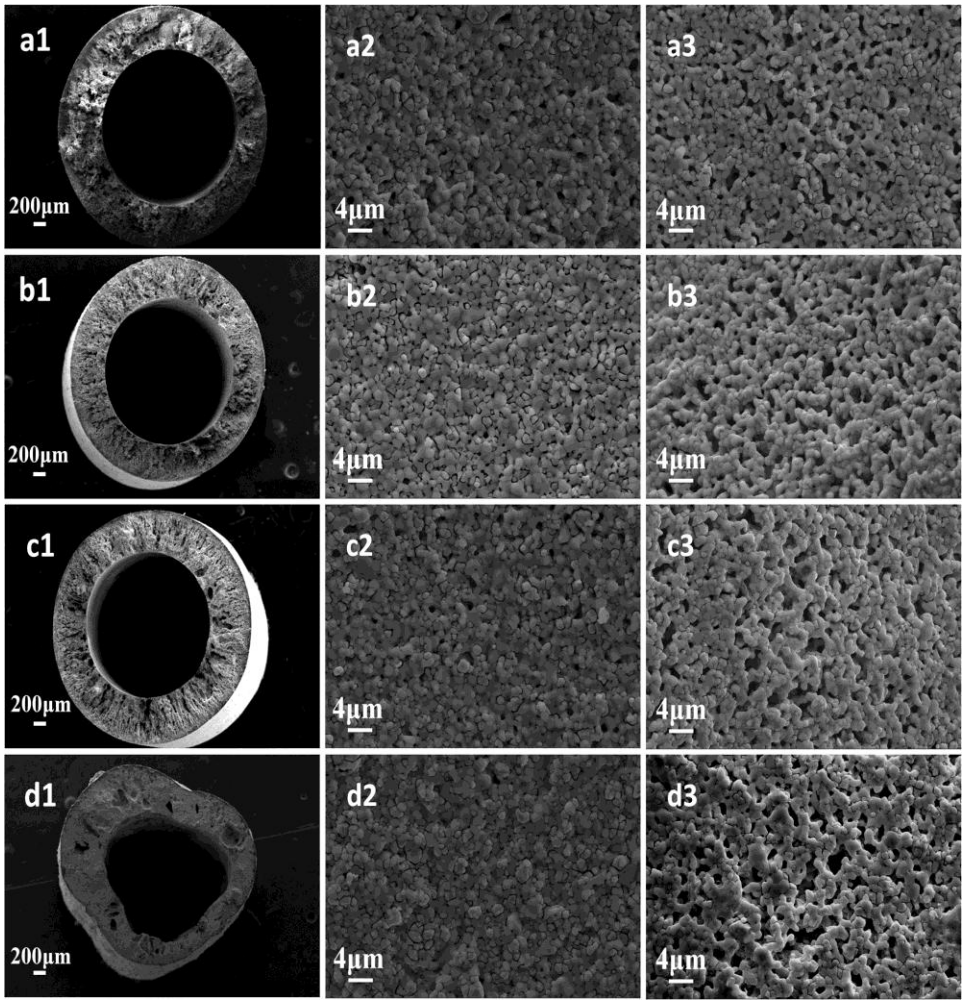

Figure 3.5 SEM micrographs of sintered NiO-YSZ supports prepared by phase inversion method with slurry A4 (a) B1 (b) B2 (c) B3 (d). 1, 2 and 3 denote cross-sectional, outer and inner surface microstructures, respectively.

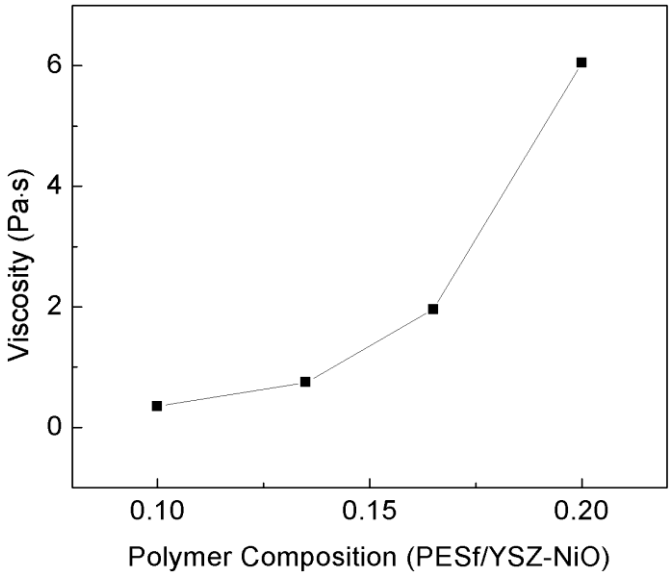

Figure 3.6 Viscosity of casting slurry prepared with different PESf composition at 25 S^{-1}.

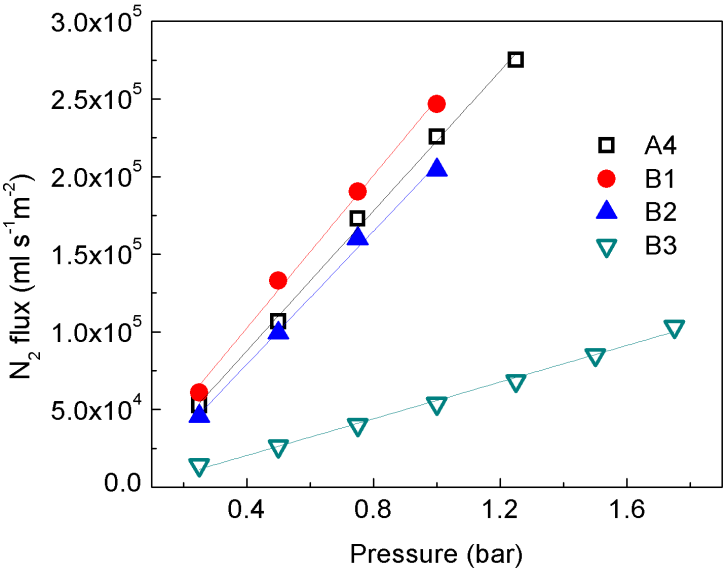

Figure 3.7 Gas permeation data for samples fabricated with different PESf content after sintered at 1450 ^{o}C and reduced at 750 ^{o}C.

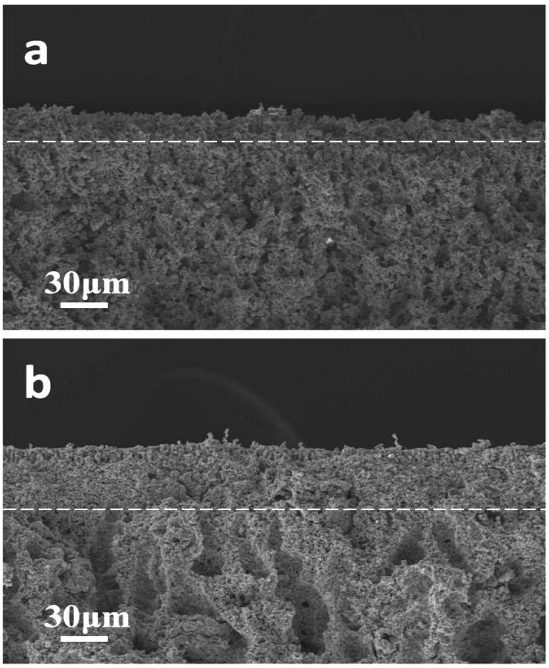

Figure 3.8 SEM of the top layer microstructure of anode support B1 (a) and B2 (b).

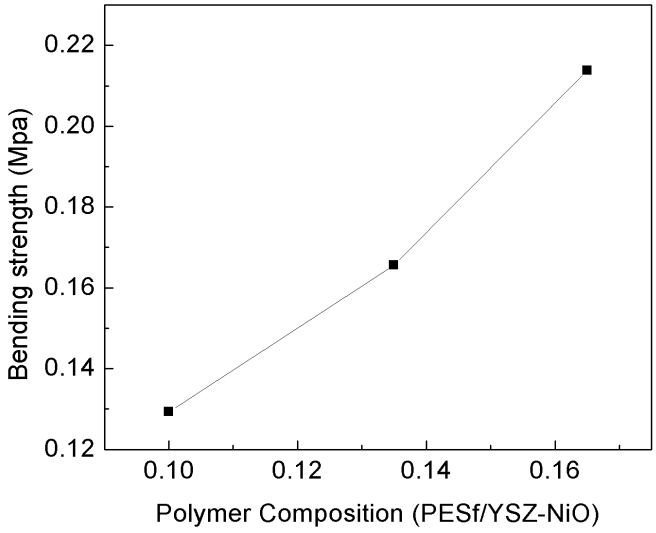

Figure 3.9 Bending strength of samples fabricated with different NMP content after sintered at 1450 ^{o}C and reduced at 750 ^{o}C.

3.3.3 Effect of microstructure on the electrical conductivity

Besides sufficient porosity for facile mass transport and adequate triple phase boundary

(TPB) sites for electrochemical reaction, the anode should also provide sufficient electrical conductivity for current collection. For anode supported SOFCs, especially for the tubular anode supported SOFC, the long electron-conducting path is expected to be the main contribution for ohmic resistance. Therefore, in this work, the effective electrical conductivity of the anode supports fabricated with slurry A1, A4, B1 and B2 were measured using four probe method [54] at room temperature. For these anode supports that were chosen for cell fabrication, B1 shows the best gas permeation value, B2 has microstructure with fully-grown finger-like pores and reasonable gas permeation value, A4 has a porous microstructure and smaller gas permeance value compared with B1, while A1 exhibits the most dense structure and the smallest gas permeation value. Before the electrical conductivity measurement was carried out, all of these samples were firstly sintered at 1450 ^{o}C for 5 hours (the same sintering condition for electrolyte fabrication), and then reduced in hydrogen at 750 ^{o}C for 5 hours. Samples B1, B2, A4 and A1 show electrical conductivity value of 167 S/cm, 100 S/cm, 209 S/cm and 914 S/cm respectively (Table 3.2), and the electrical conductivity data observed in this work is comparable to those reported in the literature [54].

Table 3.2 The conductivity of the anodes at room temperature after sintered at 1450 ^{o}C and reduced at 750 ^{o}C.

A1	A4	B1	B2
914 S/cm	209 S/cm	167S/cm	100 S/cm

Previously, Chen *et al*. [87] claimed that the electrical conductivity of YSZ-NiO tubular anode supports was efficiently affected by the porosity of the sample. It has also been reported that the electrical conductivity of NiO-YSZ sample depends on the

connection between Ni phases [88]. Therefore, sample with lower porosity, which has better Ni phase connection, is expected to show higher electrical conductivity. In this study, sample A1, which displays dense microstructure, shows the highest electrical conductivity. For sample A4, macrovoids present in the microstructure decrease the connectivity of the Ni phase, leading to lower electrical conductivity. Compared with samples A1 and A4, both samples B1 and B2 have the asymmetrical microstructure, the interconnected macrovoids and full-grown finger-like pores can further separate the Ni phase in the samples, and the electrical conductivity is consequently reduced as shown in Table 3.2.

3.3.4 Electrochemical performance of the single cells

Four types of micro-tubular SOFCs were prepared based on the chosen anode supports (A1, A4, B1 and B2). All of these single cells were tested at 750 ^{o}C with 40 SCCM humidified hydrogen (3% H_2O) as fuel and ambient air as oxidant. Figure 3.10 shows the electrochemical performance of the four different types of cells. The open circuit voltages (OCVs) of these cells are all around 1.03 V, close to the theoretical value calculated from the Nernst equation, indicating that the YSZ electrolyte film prepared by dip coating method is dense enough to separate the electrodes and prevent the potential gas leakage. Shown in Figure 3.11 are the cross-sectional SEM images of the tested cells, indicating that dense YSZ electrolyte with a thickness around 20μm can be observed for all the cells. Cells A1, A4, B1 and B2 exhibit peak cell power density of 253 mW/cm^2, 339 mW/cm^2, 449 mW/cm^2 and 606 mW/cm^2 respectively. Since the electrolyte and cathode of all the cells were fabricated at identical conditions, the cell performance difference comes from the different microstructure features of the anode prepared from the phase inversion

method.

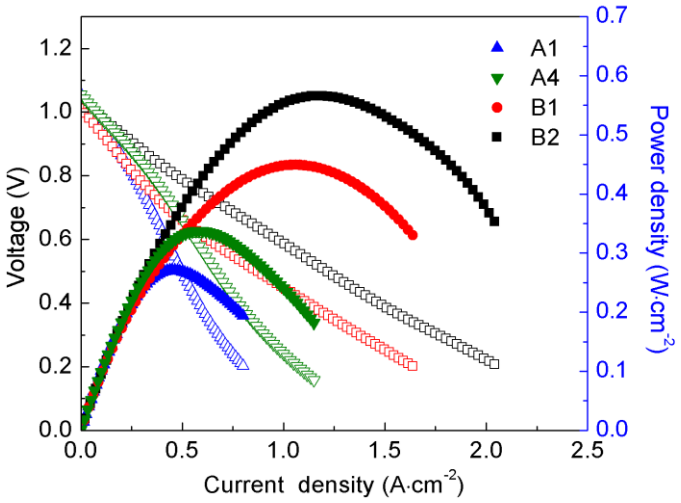

Figure 3.10 Cell performance of four cells at 750 ^{o}C, using wet hydrogen as fuel and ambient air as oxidant.

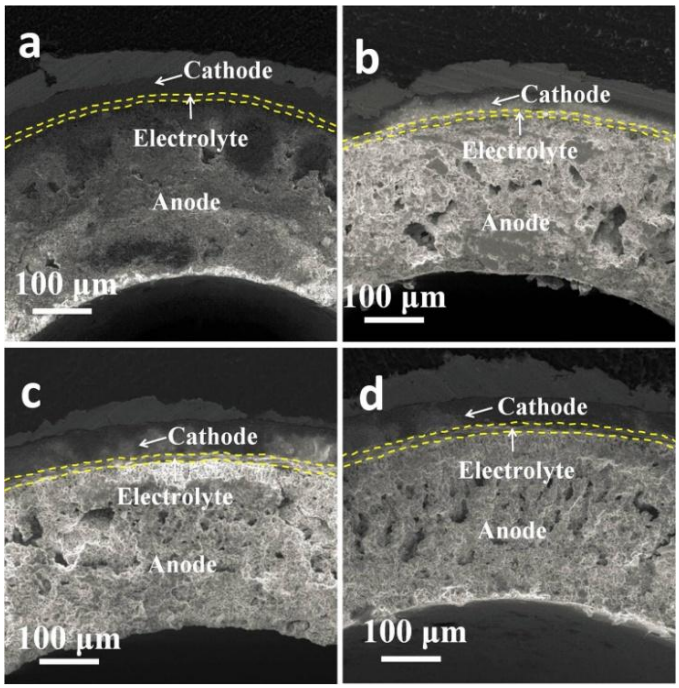

Figure 3.11 Cross-sectional SEM images of four cells fabricated with anode support A1 (a), A4 (b), B1(c) and B2 (d) after the electrochemical test.

For cell A1, the anode support shows the microstructure with homogenous distributed small pores and low gas permeance value even after reduction. Although the anode

support shows high electrical conductivity value, the poor gas transportation capability is considered to lead to the unfavorable overall cell performance. Anode support A4 shows porous microstructure with homogenously small pores combining with macrovoids and much better gas permeability, the improved microstructure and gas permeance enhanced the cell performance. Unlike the fully-grown finger-like pores which are shown in B2 samples, anode support B1 has an asymmetrical structure consisting of interconnected macrovoids. It shows the best gas permeation performance but has a lower cell power density than cells fabricated with anode support B2.The reason for the performance difference is that the top layer of the anode support B2 can perform as the functional layer of the SOFC anode [19, 89] and its less porous microstructure can provide more active sites for the electrochemical reaction in the anode.

Figure 3.12 shows the electrochemical impedance spectra (EIS) of the four types of cells tested under open circuit condition. An equivalent circuit with $R_{ohm}+R_1||Q_1+R_2||Q_2$ was applied to fit the measured EIS data [90], and the fitting result is also shown in Figure 3.12. In the equivalent circuit, the high frequency resistance (R_1) and low frequency resistance (R_2) are ascribed to the activation and concentration polarization respectively [91]. Table 3.3 shows the contribution of different resistance to the total resistance of different cells. It can be observed that the four types of cells show similar ohmic resistance, while the resistance related to the concentration polarization (R_2) decreases from A1 to B2. Cell B2 shows the smallest R_1 value, which is believed to be affected by the activation polarization. The result has a good agreement with what has been discussed above. Cell A4 shows smaller value of R_2 but larger R_1 than cell A1. The reduced R_2 value results from the improved gas permeability and the increased R_1 is

caused by the more porous microstructure adjacent to the electrolyte, which reduces the number of active sites for the electrochemical reaction compared with cell A1. For cell A4 and cell B1, the major difference of their EIS is R_2, which is affected by the different gas permeance. Compared with cell B1, cell B2 has denser top layer, which results in the reduced R_1 value.

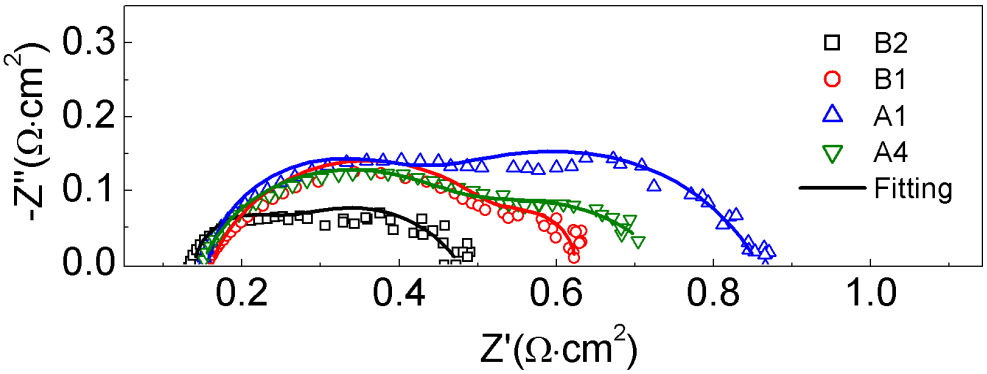

Figure 3.12 Electrochemical impedance spectra of the cells at 750 °C under open circuit condition.

Table 3.3 The area-specific resistance values obtained by fitting the impedance spectra of cells.

Sample	A1	A4	B1	B2
$\mathbf{R_{ohm}}$	0.150 Ωcm²	0.153 Ωcm²	0.156 Ωcm²	0.147 Ωcm²
$\mathbf{R_1}$	0.253 Ωcm²	0.436 Ωcm²	0.419 Ωcm²	0.228 Ωcm²
$\mathbf{R_2}$	0.453 Ωcm²	0.118 Ωcm²	0.073 Ωcm²	0.111 Ωcm²
$\mathbf{R_{total}}$	0.856 Ωcm²	0.707 Ωcm²	0.638 Ωcm²	0.486 Ωcm²

3.4. SUMMARY

The composition of the casting slurry can significantly affect the microstructure of the anode support fabricated by phase inversion method. The effect of the amount of solvent (NMP) and polymer binder (PESf) in the casting slurry on the microstructure of the

anode substrate has been systematically investigated. Increasing the NMP amount in the casting slurry favors the formation of finger-like pores and macrovoids, whereas the presence of excessive NMP in the casting slurry inhibits the finger-like pores formation. On the other hand, with the increase in the PESf amount in the casting slurry, fully grown finger-like pores can be formed instead of the asymmetrical microstructure consisting of interconnected macrovoids. However, too high PESf concentration in the casting slurry will lead to the disappearance of the finger-like pores. Based on the microstructure investigation, four anodes with different microstructure and properties were chosen for the YSZ-NiO/YSZ/YSZ-LSM cell fabrication, and maximum cell power density of 606 mW/cm^2, 449 $mW/cm^{2,}$ 339 mW/cm^2 and 253 mW/cm^2 are achieved at 750 ^oC, respectively. The difference in cell performance results from the variation of the anode support microstructure, and anode support B2 can facilitate mass transport as well as provide enlarged anode electrochemical reaction zone, leading to enhanced cell performance.

CHAPTER4 EFFECT OF PEG ADDITIVE ON ANODE MICROSTRUCTURE AND CELL PERFORMANCE OF ANODE-SUPPORTED MT-SOFCS FABRICATED BY PHASE INVERSION METHOD

4.1. BACKGROUND

Phase inversion method which was firstly developed by Lobe and Sourirajan in 1960s [25] has become one of the most important methods to fabricate polymeric membranes applied in separation process and lithium battery etc. [92, 93]. Recently, this method has been introduced to the fabrication of ceramic membrane and hollow fibers, which were extensively applied in gas separation and solid oxide fuel cells (SOFCs) [68, 94]. For the micro-tubular solid oxide fuel cells (MT-SOFCs) fabrication, anode support with the unique asymmetrical microstructure prepared by phase inversion process is believed to effectively enhance the electrochemical performance. Othman et al [59] claimed that the macrovoids, especially the long finger-like pores existing in the anode facilitated gas transport and further accelerate the anodic electrochemical reaction. Therefore, microstructure modification plays a major role for the application of phase inversion

method in SOFC fabrication. It is well known that the casting slurry composition can significantly influence the microstructure of the prepared samples [84]. Among these approaches employed to adjust the composition of the casting slurry, introducing additive in the casting solution has been proved to be an efficient method [95]. Various chemicals have been adopted as additive for phase inversion process, such as non-solvent, low molecule weight organics, inorganic salts and polymers [96, 97]. Poly(ethylene glycol) (PEG), which is regarded as one of the common used polymer additives for polymeric membrane fabrication can effectively influence the final microstructure [98]. Thermodynamic and kinetic considerations have been given to reveal the influence of PEG additive on the microstructure [99]. However, for ceramic membrane fabrication, although PEG additive has been widely employed [100, 101], there are no reports which have focused on the underlying mechanism of the PEG additive impact on the phase inversion process.

In this chapter, PEG with different molecule weight (M_w = 200, 4000, 10000 g/mole) was introduced into the N-Methyl-2-pyrrolidone (NMP)/ polyethersulfone (PESf) system as additive. The effect of PEG molecule weight and amount in the casting slurry on the microstructure was investigated in terms of both thermodynamics and kinetics. Single MT-SOFCs with the configuration of NiO-YSZ/YSZ/YSZ-LSM were fabricated based on selected anode supports. The cells were tested at 750 ^{o}C and the performances of the cells have been evaluated and discussed.

4.2. EXPERIMENTAL

The NiO-YSZ anode supports were fabricated by phase inversion method [77]. NiO

(J.T.Baker, USA) and YSZ (TZ-8YZ, TOSOH Corporation, Japan) powders were mixed together in a weight ratio of 6:4 and ball milled with ethanol for more than 24 hours using a planetary ball mill (QM-3SP2 Nanjing University Instrument Plant, China). PESf (Radel A-300, Ameco Performance, USA,) and PEG additive were dissolved into NMP (Alfa Aesar, USA) to form stable casting solutions. Subsequently, the dried NiO-YSZ powder was dispersed into the prepared casting solutions and then ball milled to get homogenous casting slurry for the phase inversion process. In this experiment, PEG with molecular weight of 200 g/mole (Sigma Aldrich, USA), 4000 g/mole (Mallinckrodt Chemical, USA) and 10000 g/mole (ChemCruz, USA) were employed as additive. The detailed composition of the casting slurries applied is shown in Table 4.1. For all of the slurries, the weight ratio between PESf and NMP was fixed to 1:5. The coagulation value of the casting solution was determined by the titration method at room temperature using water as non-solvent [99, 102]. The viscosities η (Pa s) of different casting slurries were measured by a rheometer (DHR-3, TA, USA) at room temperature (25 ^{o}C) at shear rate between 0.1 S^{-1} and 100 S^{-1}. The NiO-YSZ precursor was immersed into water bath for 24 hours to ensure a complete precipitation. Then the prepared green tubes were pre-sintered at 1200^{o}C for 2 hours to provide enough mechanical strength for electrolyte fabrication. Scanning electron microscope (SEM, Zeiss Ultra plus FESEM) was employed to examine the microstructure of the pre-sintered tubes. The gas permeation value of the samples was measured after NiO-YSZ tubes were sintered at 1450 ^{o}C and then reduced at 750 ^{o}C for 2 hours [79].

Thin YSZ film was coated on the outer surface of the pre-sintered NiO-YSZ tubes by dip-coating method [68], after sintered at 1400 ^{o}C for 5 hours, anode support with dense

YSZ electrolyte was obtained. The cathode paste, which was prepared by grinding $La_{0.7}Sr_{0.3}MnO_3$ (LSM, Fuelcellmaterials, USA), YSZ and binder (V-006, Heraeus) together, was brush painted on YSZ electrolyte. After sintered at 1100 ^oC for 2 hours, the NiO-YSZ/YSZ/YSZ-LSM single cells were obtained. Silver paste was printed on the electrodes to help collect the current and ensure better contact between electrode and silver lead wire. Cell testing was operated at 750 ^oC with 40 SCCM humidified hydrogen (3% H_2O) as fuel and ambient air as oxidant. The current-voltage curve and electrochemical impedance spectra (EIS) were measured by multi-channel VersaSTAT (Princeton Applied Research). The EIS was performed under open circuit condition with 10 mV AC amplitude and the frequency range of the measurement was from 100 kHz to 0.1 Hz.

4.3. RESULT AND DISCUSSION

4.3.1 Effect of PEG molecular weight on microstructure

NiO-YSZ anode supports were fabricated by slurries listed in Table 4.1 from S0 to S3. Three types of PEG with different molecular weight (M_w = 200 g/mole, 4000 g/mole, 10000 g/mole) were applied as additive. The coagulation value was measured to characterize the thermodynamic stability of the casting solution. It is defined as the minimum amount of nonsolvent introduced into 50g casting solution, when visible turbidity generates and does not dissolve in 24 hours at room temperature [99]. Water was selected as the non-solvent in this experiment.

Figure 4.1 exhibits the effect of PEG additive molecular weight in the casting solution on the coagulation value. It can be seen that the casting solution with larger molecule weight PEG additive shows lower coagulation value. The result suggests that the casting

solution becomes less stable with the introduction of PEG additive and when increasing the PEG additive molecular weight from 200 to 10000. Similar result has been reported by Boom *et al.* [103, 104]. They claim that PEG additive with higher molecular weight functions as stronger non-solvent in the casting solution, which reduces the amount of water that is required to trigger the phase inversion process. Previously, Reuvers and Somlders [49] indicated that instantaneous demixing preferentially occurred in the casting slurry with lower thermodynamic stability, which favored the formation of macrovoids. Therefore, it can be concluded that adding PEG and increasing molecule weight of PEG additive amount in the casting solution is beneficial to phase separation process and the pore formation.

Table 4.1 Compositions of casting slurry for YSZ-NiO anode supports fabrication.

Sample	PEG-200 amount (PEG/YSZ-NiO weight ratio)	PEG-4000 amount (PEG/YSZ-NiO weight ratio)	PEG-10000 amount (PEG/YSZ-NiO weight ratio)
S0	-	-	-
S1	0.01/1	-	-
S2	-	0.01/1	-
S3	-	-	0.01/1
S4	-	0.005/1	-
S5	-	0.02/1	-
S6	-	0.04/1	-

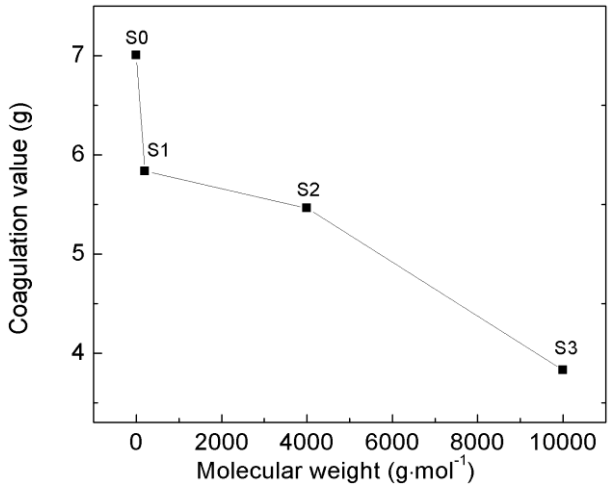

Figure 4.1 Effect of molecular weight of PEG additive on the coagulation value of the casting solution.

The viscosity of the casting slurry is also regarded as a key factor to influence the kinetic process of the phase inversion and to further affect the microstructure of the membrane [84]. To give a comprehensive investigation of the PEG additive on microstructure, the viscosity of the slurries was measured at room temperature. Figure 4.2 shows the viscosity of the slurries with different molecular weight of PEG additives. It can be seen that by adding PEG-200 additive into the casting slurry, there is a slight increase of viscosity value, and then by employing higher molecular weight PEG as additives such as PEG-4000 and PEG-10000, the viscosity changes to 0.803 Pa s and 0.875 Pa s. Previously, Kim et al [99] reported that using higher molecular weight PEG as additive led to a continuous increase of the casting solution viscosity when fabricating the polysulfone (PSF) polymeric membrane. Obviously, their result conflicts with the data observed in Figure 4.2. The discrepancy between literature and this experiment may be due to the presence of the ceramic particles in the casting slurry. On one hand, for the polymeric membrane fabrication, Ohya *et al.* [105] reported that using higher molecular weight PEG additive, longer chain length resulted in stronger entanglement with the

polymer binder chains, and the viscosity of casting solution increased. On the other hand, when ceramic particles are introduced into the casting solution, the PEG molecules can interact not only with the polymer binder molecules but also with the ceramic particles. When proper amount of PEG molecules absorbs onto the ceramic particles, it is expected to increase the repulsive force between the ceramic particles by increasing the particle charge and/or by building up a steric barrier between the ceramic particles [106, 107]. In this instance, the casting slurry is stabilized and the viscosity of the casting slurry is reduced. Thus, for ceramic casting slurry, its apparent viscosity is determined by the interaction between the additive and the polymer binder as well as the additive and the ceramic particles.

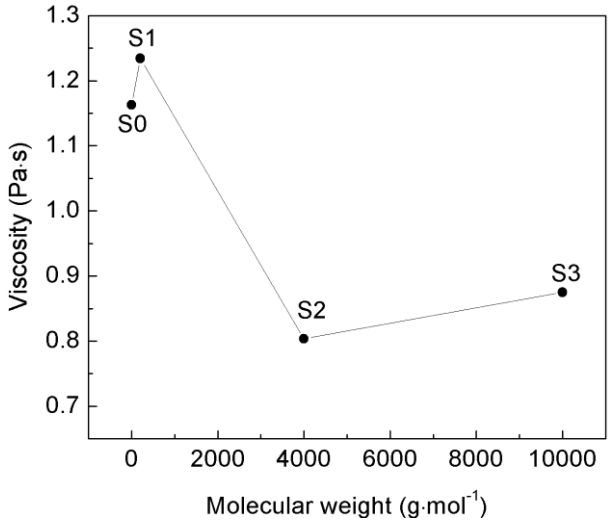

Figure 4.2 Effect of molecular weight of PEG additive on the viscosity of the casting slurry at 25 s^{-1}.

In this study, when PEG additive with smaller molecular weight (200 g/mole) is applied as additive, due to its lower molecular weight, more quantity of PEG-200 molecules will be present in the casting slurry than the heavier PEG additive per unit weight. The surface of ceramic particles can be well covered by the PEG molecules,

which is expected to reduce the viscosity. However, the PEG molecules will also entangle with the PESf chains to offset the effect exerted by the PEG/ceramic particle interaction. Consequently, a net increase of the casting slurry viscosity is observed. When higher molecular weight PEG (PEG-10000) is adopted, the surface of the ceramic particles can not be fully covered by PEG molecules, but the entanglement effect still exists, therefore, the viscosity of the casting slurry increases. From the measured viscosity data, it can be concluded that a good balance between these two effects can be obtained by employing PEG-4000 as additive.

Figure 4.3 shows the microstructure of pre-sintered samples fabricated without PEG additive as well as by employing PEG additive with different molecular weight. As shown in Figure 4.3(a), samples fabricated without PEG additive shows structure with few macrovoids. When PEG-200 is added into the casting slurry, it can be seen in Figure 4.3(b), there are no macrovoids observed in the prepared membrane. The microstructure evolution results from the combined effect of PEG additive on thermodynamic and kinetic aspects. By employing PEG-200 as additive, although the casting slurry can be thermodynamically destabilized, the increased viscosity suppresses the inter-diffusion between species in the casting slurry, thus the formation of macrovoids is inhibited. Figure 4.3 (c) exhibits the sample fabricated with PEG-4000 additive, an asymmetrical structure with long finger-like pores can be observed, and the microstructure result has good agreement with the slurry properties given above. The unstable casting slurry and reduced viscosity favor the formation of macrovoids and finger-like pores. Further, slurry containing PEG-10000 additive (S3) shows similar viscosity and even smaller coagulation value compared with slurry S2 (PEG-4000), the corresponding sample is

expected to have a porous structure as well. However, the result in Figure 4.3(d) shows a less porous microstructure with much fewer number of macrovoids. The divergence is believed to result from the long chain of the PEG-10000 molecule. In this experiment, once the phase separation process is triggered by water, the homogenous casting slurry starts to separate into a polymer rich phase and the polymer poor phase, which is believed to grow to be the nascent pores. During this phase separation process, PEG-10000 is more likely to be trapped in the polymer rich phase due to its large molecular size and strong entanglement with other species of the casting slurry [108]. In such a case, in the nascent pores, which originate from the nucleation of polymer poor phase, there is less PEG-10000 molecules. The local coagulation value in nascent pores is not as small as it is shown apparently and the grown of the pores is delayed and inhibited.

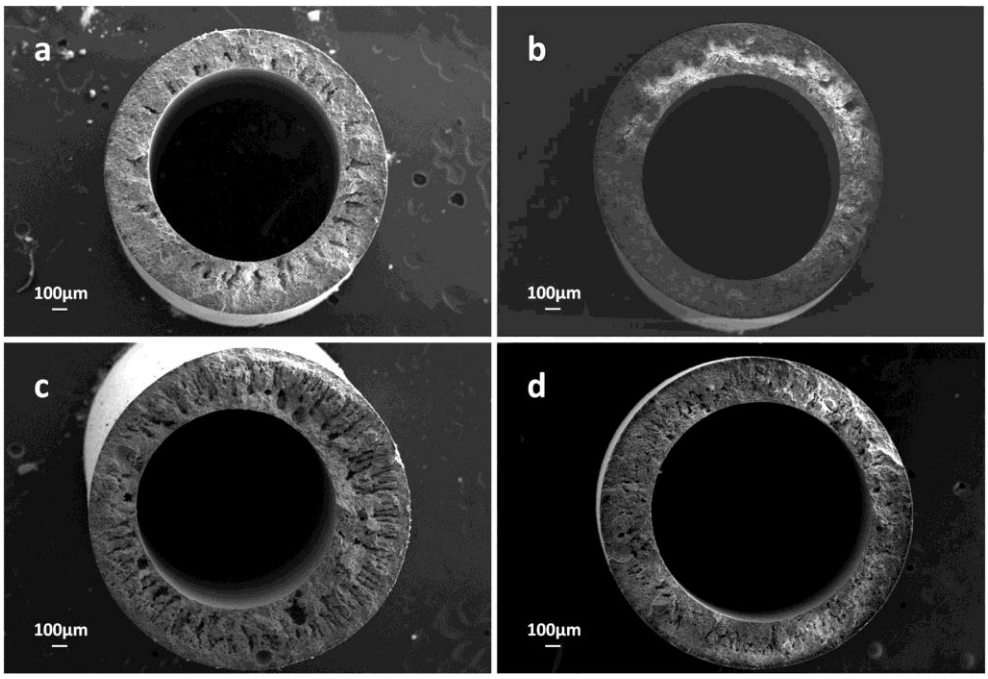

Figure 4.3 Cross-sectional SEM micrographs of pre-sintered NiO-YSZ supports prepared by a phase-inversion method with S0 (a) S1 (b) S2 (c) and S3 (d) slurry, respectively.

4.3.2 Effect of PEG amount on microstructure

From what has been discussed above, PEG-4000 can be regarded as a preferable additive candidate for anode support fabrication. Consequently, PEG-4000 was selected as the additive to investigate the influence of additive amount on microstructure. Besides slurry S2, three more compositions were applied in this study as shown in Table 4.1. Figure 4.4 shows the relationship between PEG additive amount and coagulation value. It can be seen that with the increase of the PEG additive amount in the casting solutions, the coagulation value decreases, indicating that increasing PEG-4000 amount in the casting slurry, the formation of macrovoids is expected to be favored.

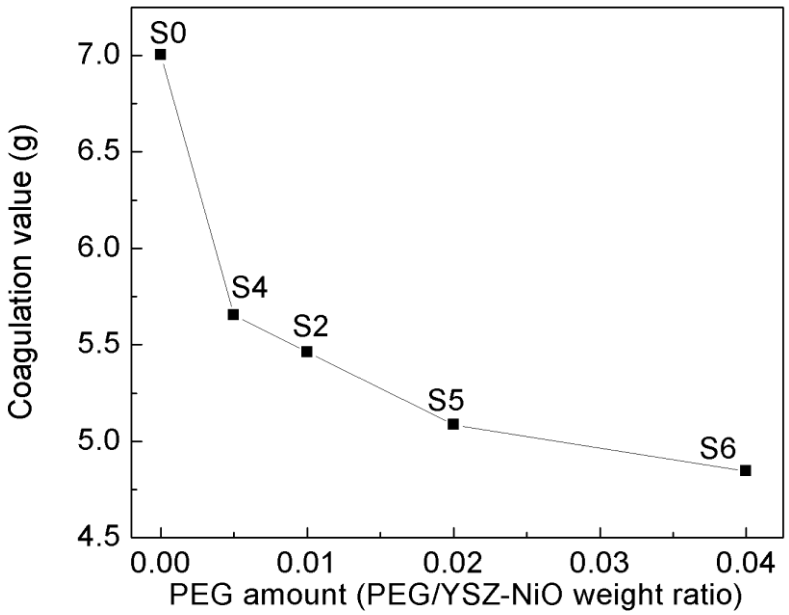

Figure 4.4 Effect of the amount of PEG-4000 additive on the coagulation value of the casting solution.

Figure 4.5 is the viscosity of slurries with different amount of PEG-4000 additive. It shows that with the increase of the PEG amount, the viscosity first increases to 1.214 Pa s and then decreases, while slurry S5 shows the lowest value of 0.336 Pa s. By further increase the PEG amount as in slurry S6, the viscosity increases. The viscosity change also results from the interaction between additive, polymer binder and ceramic particles.

Appropriate amount of PEG additive can provide optimized quantity of PEG molecules which can result in a low viscosity value. However, when excessive or inadequate quantity of PEG molecules is present in the casting slurry, the interaction between additive and polymer binder becomes the dominating factor to influence the casting slurry, the viscosity value is increased. Figure 4.6 exhibits the microstructure result of samples fabricated with different amount of PEG-4000 additive. From Figure 4.6 (a), it can be observed that there is no significant microstructure change when a small amount of PEG-4000 was added into the casting slurry. By further increasing the amount of PEG-4000 additive, it can be seen from Figure 4.6 (b) to Figure 4.6 (c), more finger-like pores are generated in the membrane. Finally, when excess amount of PGE-4000 additive is applied, the formation of macrovoids is inhibited, as shown in Figure 4.6 (d).

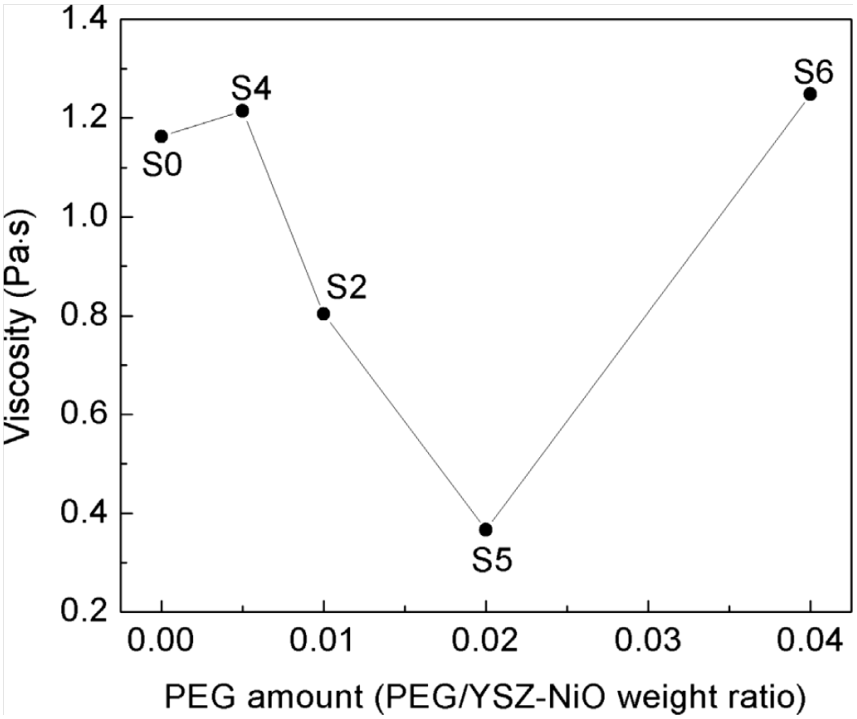

Figure 4.5 Effect of the amount of PEG-4000 additive on the viscosity of the casting solution at 25 s^{-1}.

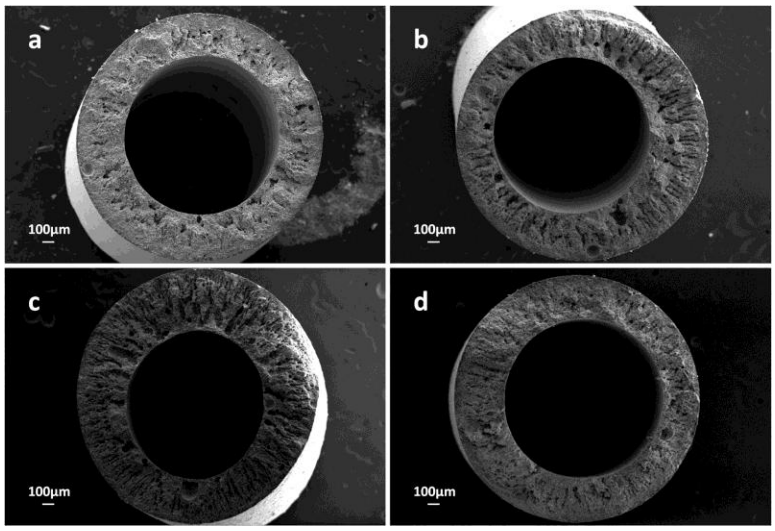

Figure 4.6 Cross-sectional SEM micrographs of pre-sintered NiO-YSZ supports prepared by a phase-inversion method with S4 (a) S2 (b) S5 (c) and S6 (d) slurry, respectively.

The result is determined by the viscosity and thermodynamic stability of the casting slurry. Sample fabricated by slurry S5, which shows low coagulation value and viscosity, exhibits long finger-like pores with axial orientation in the membrane. Moreover, although slurry S6 has a viscosity value close to slurry S4 and even lower coagulation value, the sample fabricated by slurry S6 also exhibits a less porous structure. The result is ascribed to the low concentration of PEG additive in polymer poor phase when phase separation occurs, due to the strong entanglement effect between the excess PEG-4000 molecules and other species in the casting slurry. To summarize, based on the microstructure result, it can be concluded that the kinetics of the precipitation process which is correlated with the casting slurry viscosity is the main factor to affect the pore formation. The molecular size and the quantity of PEG additive can significantly influence the final microstructure of the anode support by affecting the thermodynamic properties in the nascent pores.

4.3.3 Gas permeance of tubular anode supports

During the operation of the supported SOFCs, the anode layer that contributes the

majority of the thickness of the cell should provide adequate mass transport and thus the anode concentration polarization of the cell can be reduced. For anode supports prepared by phase inversion method, the gas transport performance is mainly determined by the thickness of the layer without macrovoids. As a result, the presence of macrovoids in the anode support is expected to favor the gas transportation performance. In this work, to demonstrate gas transport performance of the samples fabricated by phase inversion method, the gas permeation value of the samples was measured after they were sintered at 1450 ^{o}C for 5 hours and reduced at 750 ^{o}C, and the result is shown in Figure 4.7. It can be seen that the anode supports with asymmetrical microstructure show better gas permeation value. Sample fabricated with slurry S5, which shows asymmetrical microstructure with long finger-like pores has the largest gas flux value, while sample S1 exhibits poor gas transport performance due to its absence of macrovoids in the microstructure.

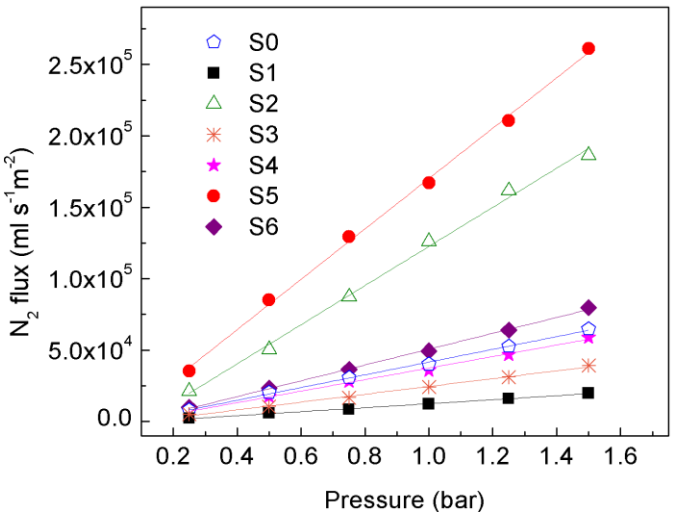

Figure 4.7 Gas permeation data for samples fabricated with PEG additive after sintered at 1450 ^{o}C and reduced at 750 ^{o}C.

4.3.4 *Electrochemical performance of the single cell*

Based on the microstructure and gas permeance performance, anode support fabricated

with slurry S5, which shows long finger-like pores and the high gas permeation value is selected to fabricate the NiO-YSZ/YSZ/YSZ-LSM MT-SOFC. For comparison, single cell with the anode support fabricated by slurry S0, which contains no PEG additive, is also applied for single cell assembling. Both the cells are tested at 750 ^{o}C with 40 SCCM humidified hydrogen (3% H_2) as fuel and ambient air as oxidant. Figure 4.8 shows the current- voltage (I-V) curve and current-power density (I-P) curve of the two types of cells. It can be seen that the open circuit voltage (OCV) value of the cells are above 1.05 V, indicating that the YSZ electrolyte fabricated by dip-coating method can efficiently separate the anode and cathode. For cell fabricated with slurry S5, it shows a peak power density of 704 Wcm^{-2}. While for cell fabricated with S0 anode support (without PEM additive), the cell peak power density can only reach 331 Wcm^{-2}. Due to the identical cathode and electrolyte applied in this study, the anode support is the main factor to influence the cell performance. For anode support fabricated with PEG additive, the long finger-like pores generated by the phase inversion process is beneficial to the mass transport in the anode. Thus, fuel gas can reach to the macrovoid free layer close to the electrolyte, where is regarded as the functional layer of the anode, the electrochemical reaction is accelerated. However, for the cell fabricated without any additive, absence of macrovoids in the anode can not effectively facilitate gas transport and the cell performance can not be enhanced. Figure 4.9 displays the electrochemical impedance spectra (EIS), the ohmic resistance of the two cells is around 0.9 Ωcm^2. According to the result, the difference of EIS is mainly ascribed to the polarization resistance, indicating that the anode prepared by PEG additive has the optimal microstructure for SOFC operation.

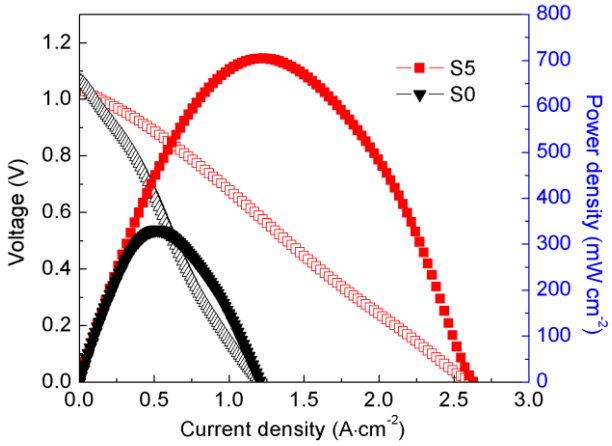

Figure 4.8 Cell performance tested at 750 ^{o}C, using wet hydrogen as fuel and ambient air as oxidant.

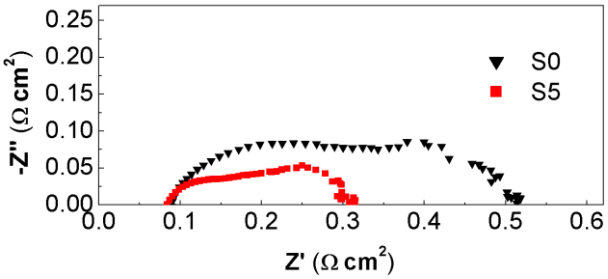

Figure 4.9 Electrochemical impedance spectra of the cells at 750 ^{o}C under open circuit condition

4.4. SUMMARY

Poly (ethylene glycol) was applied as additive in the casting slurry to fabricate the YSZ-NiO anode supports by phase inversion method. The influence of PEG additive on the phase inversion process was discussed from the point of view of kinetics as well as thermodynamics. It is found that the coagulation value of the casting solution is reduced when increasing the molecular weight or the amount of PEG additive, indicating that the casting slurry becomes less thermodynamically stable and the instantaneous demixng of

precipitation type is easier to occur. In such case, the formation of macrovoids is benefited. Moreover, the viscosity of the casting slurries with different PEG additive is also measured to evaluate the precipitation rate of membrane formation kinetically. It shows that by varying the molecular weight or amount of PEG additive in the casting slurry, the viscosity can be effectively affected. The result is different with the previous reported one, due to the interaction between additive and ceramic particles. According to the microstructure result, it can be concluded that the kinetics of precipitation process which is correlated with casting slurry viscosity is the main factor to control the pore formation. Moreover, molecular size and amount of PEG additive can also influence the microstructure. Adding proper amount of PEG-4000 additive in the casting slurry can help generate the finger-like pore, which is proved to increase the gas permeation performance of the sample. Base on the microstructure investigation, two anode supports with different microstructure were selected for cell assembling. Cells with anode supports fabricated by PEG containing slurry show a peak power density of 704 Wcm^{-2}, which is significantly improved comparing with the peak power density of 331 Wcm^{-2} for cells with anode fabricated by slurry containing no PEG additive. The cell performance enhancement can be ascribed to the difference of the anode support microstructure, which results from the presence of PEG additive in the casting slurry.

CHAPTER 5 FABRICATION OF MICRO-TUBULAR SOLIDE OIXDE FUEL CELLS USING SULFUR-FREE POLYER BINDER VIA A PHASE INVERSION METHOD

5.1. BACKGROUND

Recently, phase inversion method, which was initially developed by Loeb and Sourirajan for polymer membrane preparation [25], has been explored to fabricate ceramics for applications such as oxygen separation membranes [65, 109] and micro-tubular solid oxide fuel cells (MT-SOFCs) [110-112]. Comparing with the conventional dry pressing or isostatic pressing method [113-115], phase inversion method can produce a unique asymmetric microstructure, where the macrovoids especially the finger-like pores generated by the phase separation process can facilitate mass transport, which is expected to decrease concentration polarization and enhance the cell performance [59]. To fabricate ceramic membrane by phase inversion method, polyethersulfone (PESf) has been a popular polymer binder, due to its excellent chemical and thermal stability as well as membrane forming properties. PESf has been employed in numerous studies for various applications [84, 116, 117]. However, recently it has been reported that PESf can introduce sulfide into ceramic samples even after high temperature sintering, especially for ceramics containing barium [118]. The formed $BaSO_4$ impurity will cause detrimental effects for the application of the ceramic membrane, especially for

oxygen separation [118].

Previously, phase inversion method has also been successfully employed to fabricate tubular proton conducting solid oxide fuel cell (PC-SOFC) based on the barium containing $BaZr_{0.1}Ce_{0.7}Y_{0.1}Yb_{0.1}O_{3-\delta}$ (BZCYYb) electrolyte using PESf as polymer binder [68]. However, the potential sulfide impurity has not been investigated in that work. It is known that barium based oxide has been regarded as promising electrolyte material for PC-SOFCs [119, 120]. Therefore, considering that the negative influence may be generated by sulfide impurity on anode of PC-SOFC, investigating the sulfur residue resulting from PESf and developing sulfur free polymer binder should be a necessary and inevitable task for the application of phase inversion method to fabricate PC-SOFCs.

In this chapter, we explore three sulfur free polymer binder candidates ethyl cellulose (EC) [121], polyvinylidene fluoride (PVDF) [122] and polyetherimide (PEI) [123] for the BZCYYb based proton conducting MT-SOFCs fabrication. BZCYYb-NiO anode supports were fabricated by phase inversion method with both sulfur containing PESf and sulfur-free polymer binders, respectively. The overall performance of the sulfur-free polymer binders was examined and evaluated, and the relationship between polymer binder employed and the microstructure achieved was discussed. Based on the anode supports prepared, single cells with the cell configuration of BZCYYb-NiO / BZCYYb / $La_{0.6}Sr_{0.4}Co_{0.2}Fe_{0.8}O_{3-\delta}$ (LSCF)-BZCYYb were fabricated. The sulfur impurity was examined by X-ray diffraction (XRD) and X-ray photoelectron spectroscopy (XPS). The cell performance was tested at $650^{o}C$ with humidified hydrogen as fuel gas and ambient air as oxidant. The correlation of polymer binder, anode support property and cell performance was discussed.

5.2. EXPERIMENTAL

5.2.1. Anode support fabrication and characterization

The micro-tubular anode supports were fabricated by the phase inversion method [24]. NiO (Sigma-Aldrich, USA, D (50): 1.73 μm) and $BaZr_{0.1}Ce_{0.7}Y_{0.1}Yb_{0.1}O_{3-\delta}$ (BZCYYb) powders, which were synthesized by the solid state reaction method [119], were mixed together in a weight ratio of 65:35 with ethanol as milling medium, and then ball milled for more than 24 hours and dried. N-methyl-2-pyrrolidone (NMP, Alfa Aesar, USA) was chosen as the solvent to dissolve PESf (Radel A-300, Ameco Performance, USA), EC (Sigma-Aldrich, USA), PVDF (*Alfa Aesar*, USA) and PEI (Sigma-Aldrich, USA) respectively to form the casting solutions. Subsequently, the prepared solid powders were dispersed into the casting solutions to prepare the homogenous casting slurry. The weight ratio of the polymer binder, solvent and ceramic powder is set to 1:7:10. The viscosity η (Pa s) of different casting slurries was measured using a Rheometer (DHR-3, TA Instruments, USA) at the shear rate between 0.1 s^{-1} and 100 s^{-1} at 25 ^{o}C. The phase separation process is triggered using water as non-solvent into which the samples were immersed for more than 24 hours to ensure a complete precipitation. Subsequently, the green tubes were dried and pre-sintered at 1000 ^{o}C for 2 hours to achieve adequate mechanical strength prior to coating the electrolyte. The pre-sintered sample was examined by an X-ray diffractometer (D/MAX-3C) using Cu Kα radiation (λ= 0.15418 nm) with 2^{o} min^{-1} scanning rate in the angle range from 20^{o} to 80^{o}. XPS analysis was also performed using a Kratos Axis Ultra DLD instrument to detect the impurity residue in samples after high temperature sintering. The gas permeation data of the anode supports was measured after they were sintered at 1400 ^{o}C for 5 hours and reduced at 800 ^{o}C for 5

hours, using the reported method [84].

5.2.2. Single mciro-tubular cell fabrication and characterization

Thin BZCYYb electrolyte film was fabricated by a dip-coating process [68] on the pre-sintered micro-tubes. Upon co-sintering at 1400 ^{o}C for 5 hours, micro-tubular anode supports with dense electrolyte were prepared. The cathode was prepared by grinding $La_{0.6}Sr_{0.4}Co_{0.2}Fe_{0.8}O_{3-\delta}$ (LSCF)-BZCYYb mixture powder (with a weight ratio of 1:1) with binder (V-006, Heraeus) to make the cathode slurry, brush-printing the cathode slurry on the electrolyte, and then firing at 1000 ^{o}C for 2 hours. The prepared cells were tested at 650 ^{o}C with 40 SCCM humidified (3 vol% H_2O) hydrogen as fuel and ambient air as oxidant.

The microstructure of the micro-tubular anode-supported cells was characterized by scanning electron microscope (SEM, Zeiss Ultra plus FESEM). The current density-voltage curve (I-V curve) and the impedance spectra of cells were obtained by multi-channel VersaSTAT (Princeton Applied Research).

5.3. RESULT AND DISCUSSION

5.3.1 Microstructure of the anode support

Among the three sulfur-free polymer binder candidates employed, PVDF can not show enough solubility in the NMP solvent when using the fixed polymer binder and solvent ratio. When using EC as the polymer binder, the prepared green sample is mechanically weak, and after sintered at 1200^{o}C, the sample shows small cracks, which is not suitable for the cell fabrication. For the third candidate PEI, the casting slurry shows better processing properties than the others. Therefore, by evaluating the performance of all the three sulfur-free polymer binder candidates, we select PEI for the anode support

fabrication.

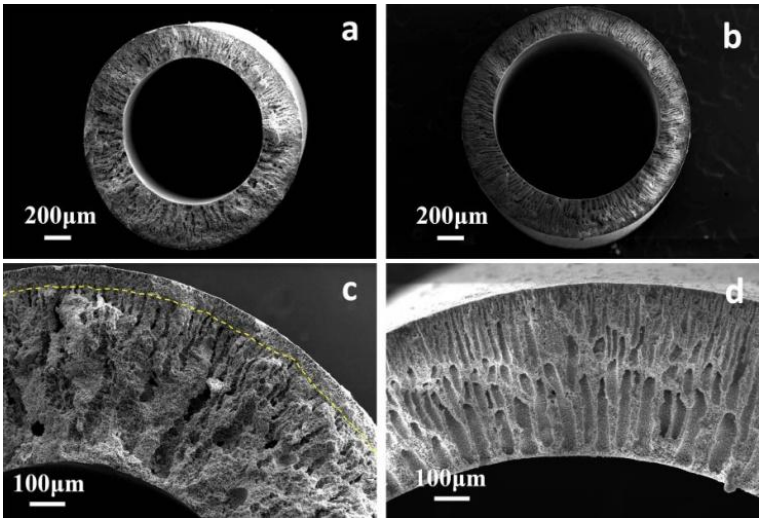

Figure 5.1 Cross-section SEM images of tubular samples after pre-sintered at 1000 ^{o}C for 2 hours fabricated by PESf (a) (c) and PEI (b) (d).

The microstructure of the BZCYYb-NiO anode supports fabricated by PESf and PEI are shown in Figure 5.1 (a) and Figure 5.1 (b) respectively. Both of the anode supports have the typical asymmetrical microstructure generated by the phase inversion process. However, for the large finger-like pores, the geometry is different. The large finger-like pores of samples fabricated with PESf have a tortuous geometry and the individual finger-like pore tends to merge with each other when growing near the inside of the tube. In contrast, for samples fabricated with PEI, they show straight parallel distributed finger-like pores. The solubility parameter difference has been wildly used to estimate the compatibility between the materials involved in the phase inversion method and further to explain the mechanism of pore formation [22]. The value can be calculated by the formula:

$$\Delta\delta_{i-j} = \left[\left({}^{i}\delta_d - {}^{j}\delta_d \right)^2 + \left({}^{i}\delta_p - {}^{j}\delta_p \right)^2 + \left({}^{i}\delta_h - {}^{j}\delta_h \right)^2 \right]^{1/2} \qquad (5.1),$$

Where the δ_d, δ_p and δ_h represent the dispersion, polar, and hydrogen bonding components of the solubility parameter, respectively. Materials with smaller solubility difference value $\Delta\delta$ show better compatibility and are able to interact with each other which will result in dissolution. The solubility parameter of solvent, polymer binders and their difference $\Delta\delta_{s\text{-}p}$ are listed in Table 5.1.

Table 5.1 the solubility parameters of the solvent and polymer binders, and the solubility parameter difference between solvent and polymer binder.

Materials	$\boldsymbol{\delta_d}$	$\boldsymbol{\delta_p}$	$\boldsymbol{\delta_h}$	$\boldsymbol{\Delta\delta_{s\text{-}p}}$	**Ref**
PESf	17.6	10.4	7.8	2.03	[22]
PEI	21.1	7.4	7.1	5.80	[124]
NMP	18.0	12.3	7.2	-	[22]

It can be seen that PEI shows larger solubility parameter difference with solvent NMP than PESf. The result indicates that PEI is less compatible with the solvent, and consequently the phase separation process of PEI/NMP system is easier to be triggered. Based on which, Lai *et. al*. [125] claimed that larger solubility difference between polymer binder and solvent can benefit the phase separation process and pore formation. According to this solubility criterion, sample fabricated by using PEI as the polymer binder is expected to show a more porous microstructure than PESf. The result shown in Figure.5.1 is in agreement with this predication; more quantity of finger-like pores can be observed in Figure 5.1(b), which is fabricated with PEI. Although the solubility difference criterion can be adopted to explain the microstructure result achieved, the formation of different geometry of the finger-like pores can not be well revealed merely depending on the $\Delta\delta_{p\text{-}s}$ value.

Therefore, besides the discussed solubility parameter difference criterion, another key

factor that should be taken into consideration is the viscosity of the casting slurry. Figure 5.2 displays the viscosity of casting slurries using PEI and PESf as the polymer binder, respectively. It can be observed that at room temperature (25 ^{o}C), the casting slurry with PEI shows relatively larger viscosity than PESf. Smolder *et.al*. [30] claimed that the nascent pores formed during the phase separation process resulting from the nucleation of the polymer poor phase, and they also ascribed the growth of the nascent pores to the diffusion of solvent and non-solvent in and out of the pores. Therefore, for the casting slurry with higher viscosity, the diffusional flow of solvent and non-solvent will be hindered, and the growth of the finger-like pores will be inhibited in some extent. In this study, for the casting slurry using PESf as polymer binder, its lower viscosity leads to a faster exchange of solvent and non-solvent between the nascent pores and the surrounding casting slurry. In such a case, the growth of the finger-like pores can be facilitated and the nascent pores are able to expand laterally. The finger-like pores are subsequently merged with each other near the inner side of the micro-tubular sample. Eventually, tortuous pore geometry will be achieved. On the other hand, when using PEI as the polymer binder, the nascent pores can only grow along the radial direction due to the limited diffusional solvent flow from the casting slurry, resulting in the long finger-like pores with gradient. To summarize, the different microstructure achieved by employing PESf and PEI as the polymer binder is due to the difference in viscosity of the casting slurry.

The gas permeance of the prepared anode supports was measured after sintered at 1400 ^{o}C for 5 hours and reduced at 800 ^{o}C for 5 hours; the result is shown in Figure 5.3. It can be seen that the prepared sample using PEI as the polymer binder shows relatively larger

gas permeance value.

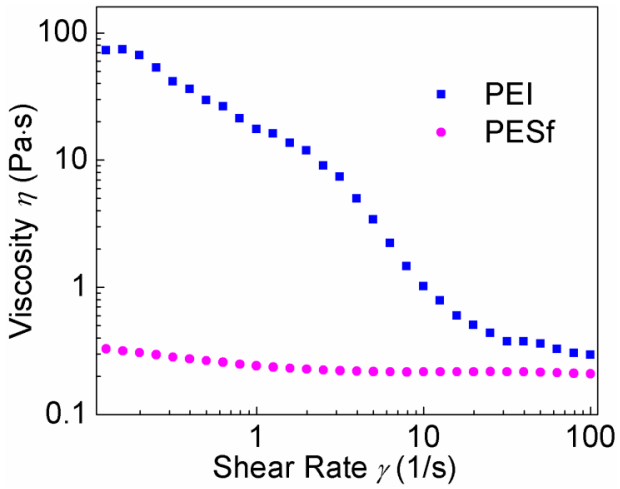

Figure 5.2 Viscosity of casting slurry prepared using PEI and PESf as polymer binder at room temperature (25 °C).

The gas permeance result is affected by the microstructure shown in Figure 5.1(c). A relatively dense layer can be observed for the sample fabricated using PESf as the polymer binder, which increases the overall gas permeance performance of the sample [86].

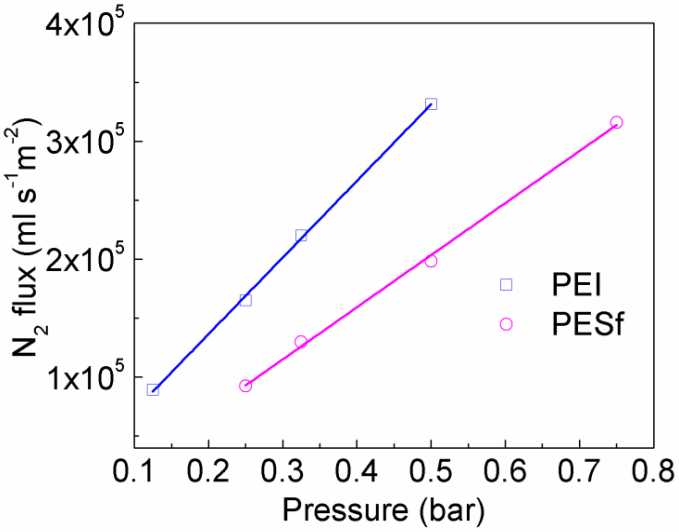

Figure 5.3 Gas permeation data for anode supports fabricated with PEI and PESf, sintered at 1400°C and reduced at 800 °C.

5.3.2 Phase impurities analysis

The impurities in the anode supports that may be introduced by the polymer binder is also an important factor to consider. To investigate the potential impurities of the anode support, BZCYYb-NiO samples fabricated with PESf and PEI were examined by XRD after pre-sintered at 1000 ^{o}C for 2 hours. Figure 5.4 shows that the characteristic peaks of NiO and BZCYYb can be observed for both samples. Additionally, peaks corresponding to barium sulfate ($BaSO_4$) can be observed from the samples fabricated with PESf [118]. The result indicates that when employing PESf as the polymer binder, the sulfide impurity ($BaSO_4$) can be introduced into the pre-sintered anode support. Although high temperature treatment process is required for the cell fabrication to form the dense electrolyte, the formed $BaSO_4$ impurity may not be completely removed.

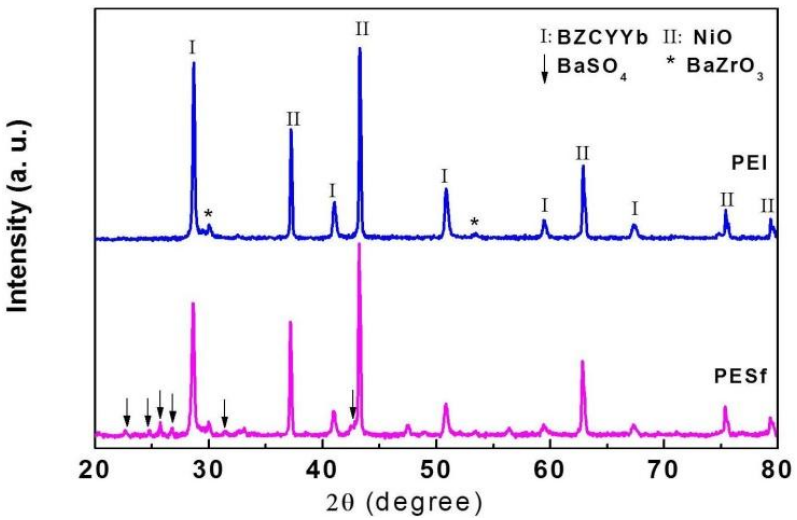

Figure 5.4 XRD patterns for BZCYYb/NiO anode pre-sintered at 1000^{o}C for 2 hours.

To detect the residue of $BaSO_4$ impurity after high temperature treatment, anode supports fabricated with PESf as the polymer binder were analyzed after sintered at 1400 ^{o}C for 5 hours using XPS. High resolution narrow scan was taken of the S region. As it is shown in Figure 5.5, the peak at 168.85 eV corresponds to the SO_4^{2-} ion [126], indicating

that after high temperature sintering process, $BaSO_4$ can not be completely removed in the anode support fabricated with PESf. Due to the existence of the $BaSO_4$ impurity, the composition of BZCYYb will be deviated from the desirable stoichiometry, and the proton conductivity and catalysis activity will be deteriorated. Therefore, the overall cell performance is expected to be decreased.

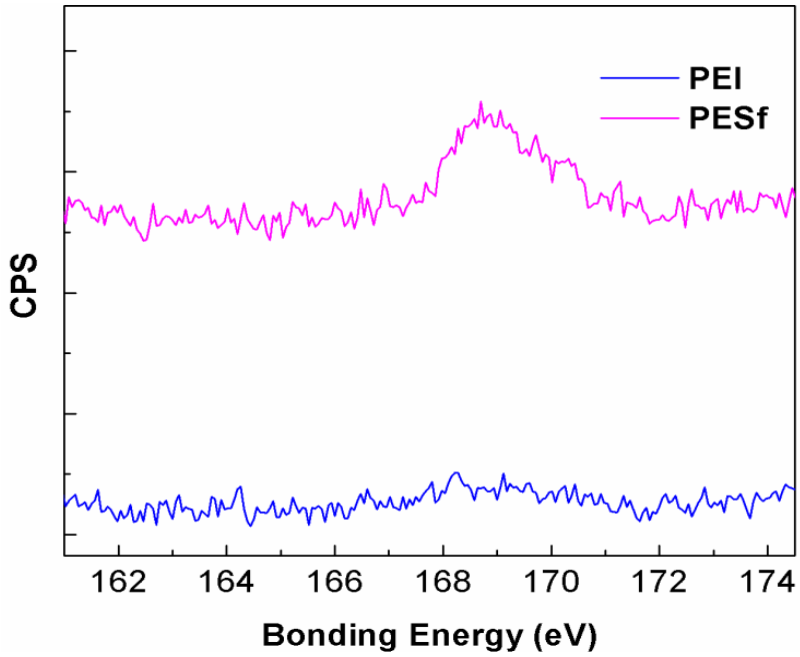

Figure 5.5 XPS spectra characterization of BZCYYb/NiO anode sintered at 1400 ^{o}C for 5 hours.

5.3.3 Electrochemical performance of the MT-SOFCs

The performance of cells was evaluated by measuring the I-V curve and impedance spectra at 650 ^{o}C with 40 SCCM humidified hydrogen (3vol% H_2O) as fuel and ambient air as oxidant. As shown in Figure 5.6, the open circuit voltages (OCVs) of cell-a and cell-b are both around 0.95V, which is consistent with the typical OCVs using BZCYYb electrolyte at similar testing conditions. Maximum cell power densities of 0.35 and 0.45 Wcm^{-2} were obtained for cell-a and cell-b at 650 ^{o}C respectively.

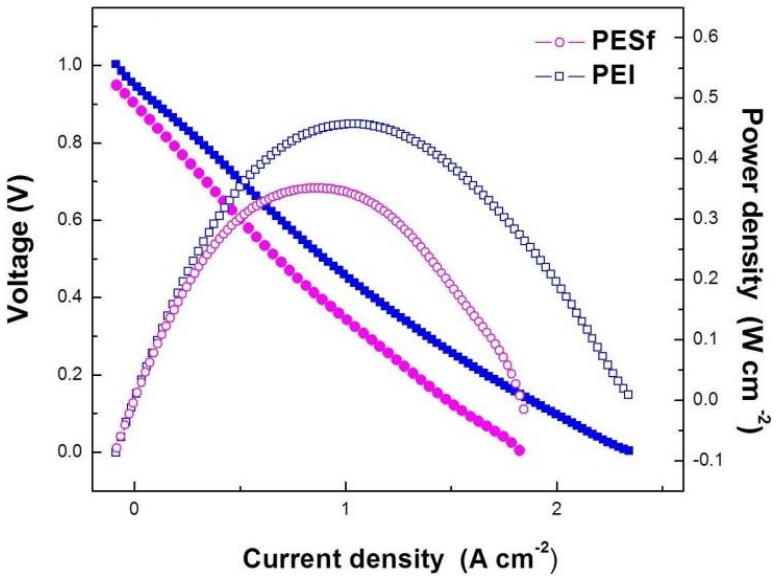

Figure 5.6 Current-voltage and power density curves for cell-a (PESf) and cell-b (PEI), tested at 650 ^{o}C.

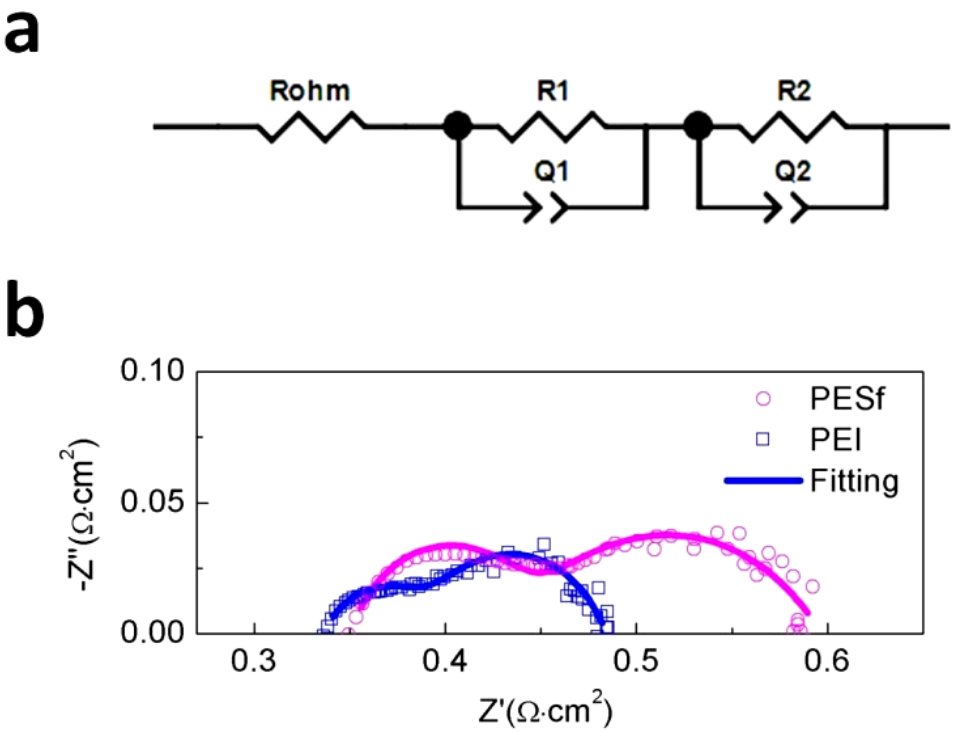

Figure 5.7 Equivalent circuit to fit the impedance spectra data (a) and the impedance spectra for the single cells.

The measured electrochemical impedance spectra (EIS) are shown in Figure 5.7(b).

The cell impedance spectrum is mainly consisted of two distinct arcs. An equivalent

circuit with $R_{ohm}+R_1||Q_1+R_2||Q_2$ configuration was employed to fit the measured EIS data, shown in Figure 5.7 (a). In this circuit, R_{ohm} is the ohmic resistance of the cell, R_1 at the high frequency is related to the activation polarization and the contribution of the low frequency resistance R_2 is due to the concentration polarization [90, 91]. The fitting result is listed in Table 5.2 and it can be seen that the ohmic resistance of both cells is similar. Cell-a (PESf) and cell-b (PEI) also show similar concentration polarization that is related to R_2, which only accounts for a minor portion of the total polarization value. The smaller concentration polarization is resulted from the finger-like pores in the anode support fabricated from phase inversion process. The finger-like pores will function as the transportation channels that can facilitate the diffusion of fuel gas to the anode functional layer. On the other hand, according to the microstructure shown in Figure 5.1, it can be seen that the sample fabricated with PESf shows denser top layer with finer microstructure, which can act as the functional layer of the Ni-YSZ anode and enlarge the triple phase boundaries (TPBs) of the anode. Therefore, cell fabricated with PESf will show smaller activation polarization. However, based on the fitting result, cell fabricated with PEI has lower resistance R_1. Virkar *et. al.* claimed that the activation polarization is related to the charge transfer on the electrode [127]. In this work, the barium sulfide phase in BZCYYb of the Ni-BZCYYb anode is expected to be the key factor to affect the activation polarization. The insulating sulfide impurity introduced by PESf leads to deteriorated catalytic activity of the anode and consequently increases the active polarization resistance. By considering the cell performance and EIS data, it can be concluded that PEI offers a better option as the polymer binder to fabricate ceramic materials using the phase inversion method.

Table 5.2 The area-specific resistance values obtained by fitting the impedance spectra of cells.

Sample	PEI/Ωcm^2	PESf/Ωcm^2
$\mathbf{R_{ohm}}$	0.334	0.348
$\mathbf{R_1}$	0.0560	0.0909
$\mathbf{R_2}$	0.0920	0.107
$\mathbf{R_{total}}$	0.482	0.546

5.4. SUMMARY

BZCYYb based anode-supported MT-SOFCs were successfully fabricated by phase inversion method using PESf and PEI as the polymer binder, respectively. Comparing with PESf, the sulfur-free PEI does not introduce sulfur impurities in the ceramic samples. The anode supports fabricated using PEI show finger-like pores with long graded finger-like pores compared with using PESf as the polymer binder. Anode-supported single cells based on BZCYYb proton conducting electrolyte fabricated using PEI and PESf as the polymer binder show the maximum cell power density of 0.45 Wcm^{-2} and 0.35 Wcm^{-2} at 650 ^{o}C, respectively. The enhanced cell power output using PEI as the polymer binder is attributed to the absence of sulfur-containing impurity phase in the anode and more desirable anode microstructure.

CHAPTER6 CONTINUOSLY GRADED OF MT-SOFC FABRICATED BY PHASE INVERSION METHOD WITH BLEND POLYMER BINDER

6.1 BACKGROUND

Solid oxide fuel cells (SOFCs) have attracted significant attentions due to their high energy conversion efficiency, low emission and fuel flexibility [1, 128]. Performance of SOFCs is governed not only by the intrinsic property of the cell materials but also by the microstructure of the electrolyte and electrodes. For anode supported SOFCs, to minimize the concentration polarization from the thick anode layer, a common strategy is to fabricate the anode with graded microstructures [129]. Graded anode microstructure is expected to not only facilitate gas transportation but also enlarge the triple phase boundaries (TPBs) for the anodic electrochemical reaction. Therefore, it has been an important topic to develop efficient method for the fabrication of anode supports with gradient porosity. Extensive efforts have been made to achieve gradient porosity in the anode, for example using multiple step tape casting [130], phase inversion [22], and freeze tape casting [131]. Among these different approaches reported, anode support with unique asymmetrical microstructure can be prepared through the phase inversion process. Most importantly, phase inversion process enables an efficient way to fabricate anode-supported micro-tubular SOFCs [111]. However, when using phase inversion for the anode fabrication, a skin layer with low porosity is typically generated [70],

which is expected to limit the gas transportation in the anode and lower the cell performance [22]. To eliminate such a skin layer, Tan *et al.* [100] treated the inner surface of the green sample by solvent containing internal coagulants while Chen *et al.* [132] developed a method combing phase inversion with dip-coating of an additional graphite layer. Although the skin layer can be effectively removed through these methods, the complex multiple step operation process will add inconvenience for the anode fabrication and a simple fabrication process will be desirable for practical applications.

In this chapter, for the first time, PESf-PEI blend was employed as the polymer binder to fabricate anode supported MT-SOFC by phase inversion process. Anode with gradient porosity and porous inner surface was obtained. The novel microstructure was characterized by SEM and analyzed based on the BSE images [133]. Potential impurities of anode support that may be introduced by the sulfur-containing PESf binder was examined by XPS. NiO-YSZ/YSZ/LSM-YSZ single cells based on different anode supports were fabricated and tested.

6.2 EXPERIMENTAL

NiO-YSZ anode support was fabricated by phase inversion method [111]. NiO (J.T.Baker, USA) and YSZ (TZ-8YZ, TOSOH Corporation, Japan) powders (6:4 weight ratio) were ball milled for 24 hours in ethanol and then dried. Polymer solution was obtained from polymer binder and N-methyl-2-pyrrolidone (NMP, Alfa Aesar, USA) solvent in a weight ratio of 1:5. In this study, the PESf (Radel A-300, Ameco Performance, USA) - PEI (Sigma-Aldrich Corporation, USA) polymer blend (1:1 weight ratio) was used as the polymer binder. For comparison, PESf and PEI were also applied

as the polymer binder separately for anode support fabrication, respectively. NiO-YSZ powders were dispersed into the polymer solution (1:1 weight ratio) and then ball milled for 24 hours to form a viscous slurry for the phase inversion process. Water was selected as the non-solvent and the precipitation time was 24 hours. The dried green samples were pre-sintered at 1200 ^{o}C for 2 hours to obtain enough mechanical strength for further electrolyte film coating, and the microstructure of the pre-sintered sample was examined by SEM (Zeiss Ultra plus FESEM). To further characterize the microstructure fabricated by the blend polymer binder, NiO-YSZ samples sintered at 1450 ^{o}C for 5 hours and reduced at 750 ^{o}C in hydrogen were immersed into resin (EpoThin Epoxy Resin, BUEHLER, USA) under vacuum for 5 min and hardened in air at room temperature for 12 hours. Subsequently, the prepared Ni-YSZ sample was cut and polished to obtain an even two dimensional surface for the backscattered electrons (BSE) observation. X-ray photoelectron spectroscopy (XPS) analysis was performed using a Kratos Axis Ultra DLD instrument to detect the sulfur impurity residue in the NiO-YSZ samples after the samples were sintered at 1450 ^{o}C for 5 hours.

YSZ electrolyte was fabricated by a dip-coating method [77]. Upon sintering at 1450 ^{o}C for 5 hours, anode supports with dense YSZ electrolyte films were prepared. $(La_{0.80}Sr_{0.20})_{0.95}MnO_{3-x}$ (LSM, Fuelcellmaterials, USA)-YSZ composite cathode was fabricated by brush painting method and sintered at 1100 ^{o}C for 2 hours. Cell test was operated at 750 ^{o}C with 3 vol% H_2O hydrogen as fuel and ambient air as oxidant. The current density-voltage curve (I-V curve) and the impedance spectra of cells were obtained using multi-channel VersaSTAT (Princeton Applied Research).

6.3 RESULT AND DISCUSSION

Blending is a useful strategy to modify the properties of polymer materials and has been widely applied, especially for polymeric membrane fabrication by phase inversion method [134]. In this work, for the first time, we introduce the blend polymer binder to fabricate the NiO-YSZ anode for SOFCs by phase inversion method. Figure 6.1 shows the microstructure of the NiO-YSZ anode substrates fabricated using PESf, PEI and PESf-PEI blend polymer as the binder, respectively. It can be seen that samples fabricated with PEI or PESf polymer binder show the microstructure with few macrovoids and dense inner layer (Figure 6.1 (a) to Figure 6.1 (d)). On the other hand, for the samples fabricated using PESf-PEI polymer blend, they show a microstructure with gradient porosity and porous inner surface (Figure 6.1 (e) and Figure 6.1 (f)). We have previously observed the dense inner layer existing in the NiO-YSZ anode support using PESf polymer binder and found that the dense inner layer would lead to significant concentration polarization since this layer would be exposed to the fuel steam side during SOFC operation [22]. Therefore, comparing with the samples fabricated with PESf-PEI blend polymer binder, the dense inner layer shown in Figure 6.1 (b) and Figure 6.1 (d) are expected to obstruct the transportation of the fuel gas in the anode and lead to large concentration polarization.

To better characterize the microstructure of samples prepared using PESf-PEI polymer blend, the BSE image of the reduced sample (shown in Figure 6.2 (a)) was analyzed based on the different gray level of the pores and solid phase [133]. In Figure 6.2 (b), the different pores in the microstructure are labeled with their radius using different color. It can be seen that pores with larger radius are easier to be found close to the inner side of

the sample. Moreover, Figure 6.2 (c) shows the distribution of the pore centre in the microstructure. It can be observed that the density of the pore centre increases gradually from the inner side of the sample to the outer side. The result indicates that the tubular samples fabricated with PESf-PEI polymer blend have the microstructure with porosity gradient through the cross section of the NiO-YSZ substrate. To further quantify this microstructure, the pore radius distribution against the distance to the centre of the circular cross section has been analyzed based on the BSE image and shown in Figure 6.2 (d), the direction of R in this figure is identified in Figure 6.2 (b).

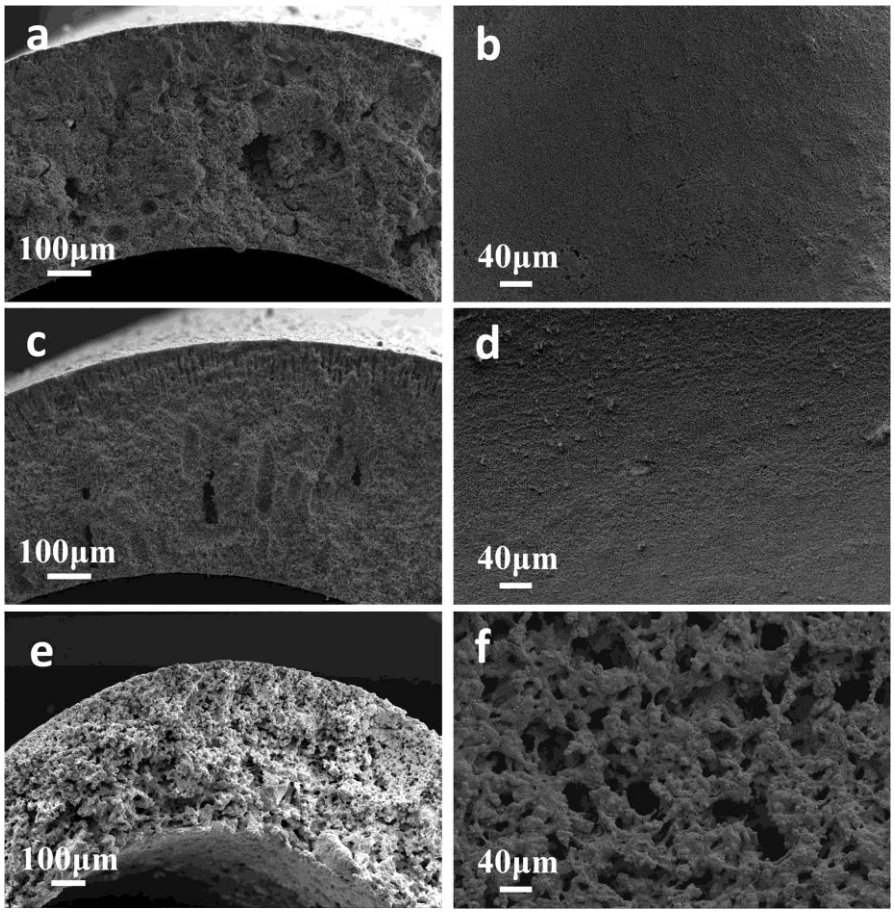

Figure 6.1 SEM photograph for the cross-sectional and inner surface of the anode support fabricated using PESf (a)-(b), PEI (c)-(d) and PESf-PEI blend (e)-(f) as polymer binder, respectively.

From this result, a domain of the pores can be observed, which further proves that the

sample fabricated with polymer blend has the microstructure with gradient porosity. Previously, continuously graded anode has been proved to improve the electrochemical performance of the cell [129]. Therefore, the sample fabricated with polymer blend, which has graded microstructure and porous inner surface, is more suitable for the MT-SOFC fabrication.

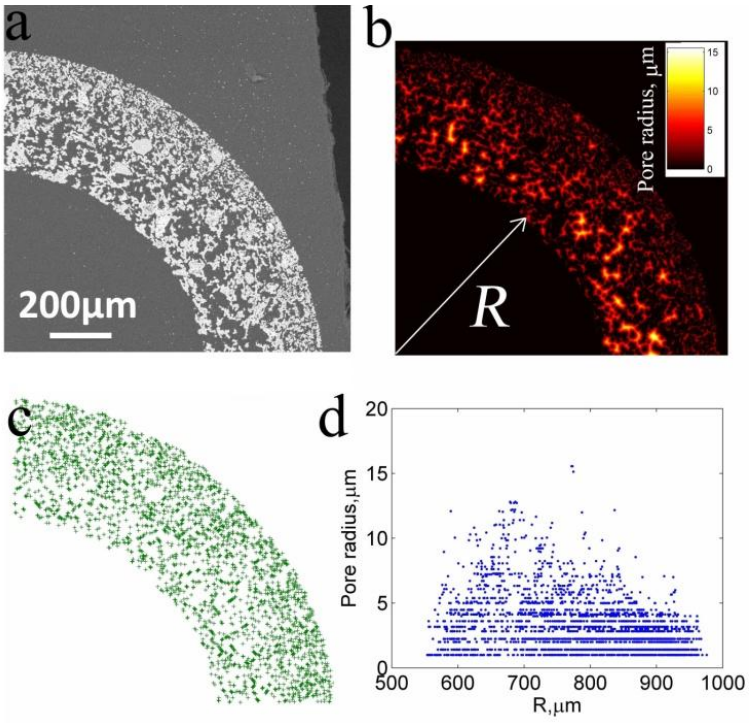

Figure 6.2 The procedure of microstructure analysis: (a) shows the raw BSE microscopy of anode fabricated with blend polymer, (b) shows the segmentation of pores labeled with different radius, (c) is the distribution of the centre of the pores, (d) shows the pore radius distribution against the distance to the centre of the circular cross section.

Besides the microstructure, materials composition of the anode support is another important factor that can affect the cell performance. Leo *et al.* [126] reported that the sulfur containing PESf polymer can introduce sulfide impurity into the ceramic sample and can affect the ion diffusion in the ceramic sample negatively. Since sulfur-containing PESf was used as polymer binder in this study, it is necessary to examine the material composition of the prepared NiO-YSZ anode support. The samples fabricated with

different polymer binders were analyzed using XPS after sintered at 1450 ^{o}C for 5 hours, and high resolution narrow scans were taken of the S regions. The XPS result is shown in Figure 6.3. No sulfur peaks at 168.85ev (SO_4^{2-}) or 162ev (S^{2-}) were observed for all of these samples, indicating that no sulfur impurities were present in the anode support after high temperature sintering process when employing PESf or the PESf-PEI blend polymer as binder.

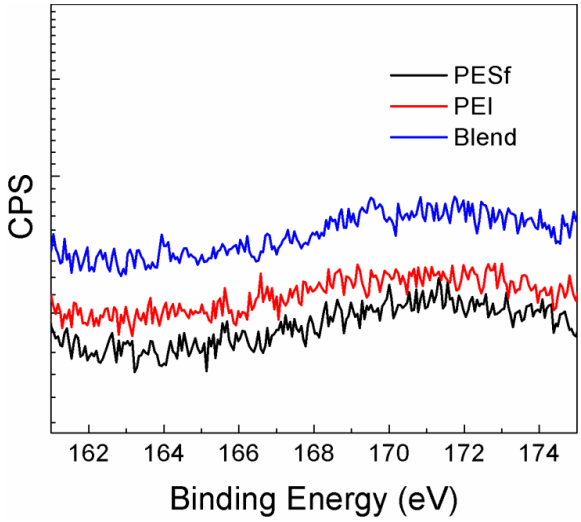

Figure 6.3 XPS spectra characterization of NiO-YSZ anode sintered at 1450 ^{o}C for 5 hours.

MT-SOFCs were prepared using the NiO-YSZ anode supports fabricated with different polymer binders. The cells were tested at 750 ^{o}C with humidified hydrogen (3 vol% H_2O) as fuel gas and ambient air as oxidant. Figure 6.4 (a) shows the voltage-current characteristic curves of the cells with three different NiO-YSZ anode substrates. For cells fabricated with PESf, PEI and PESf-PEI polymer blend, the open circuit voltages (OCV) are 1.05V, 1.03V and 1.03V respectively. Cells fabricated with polymer blend show a peak power density of 630 mWcm^{-2} at 750 ^{o}C, and the cell performance is significantly improved comparing with cells fabricated with PEI (210 mWcm^{-2}) and PESf (330

mWcm^{-2}) polymer binders. The enhanced cell performance can be ascribed to the unique porous microstructure shown in Figure 6.1. The large pores near the inner side of the tubular anode support are expected to significantly facilitate the transportation of fuel gas. Furthermore, the finer microstructure adjacent to the electrolyte can enlarge the triple phase boundaries (TPBs) and increase the active sites for the anodic electrochemical reaction. Consequently, both the concentration polarization and the activation polarization are reduced. As shown in Figure 6.4 (b), cells fabricated with PESf-PEI polymer blend have smaller polarization resistance than the cells fabricated using either PESf or PEI polymber binder.

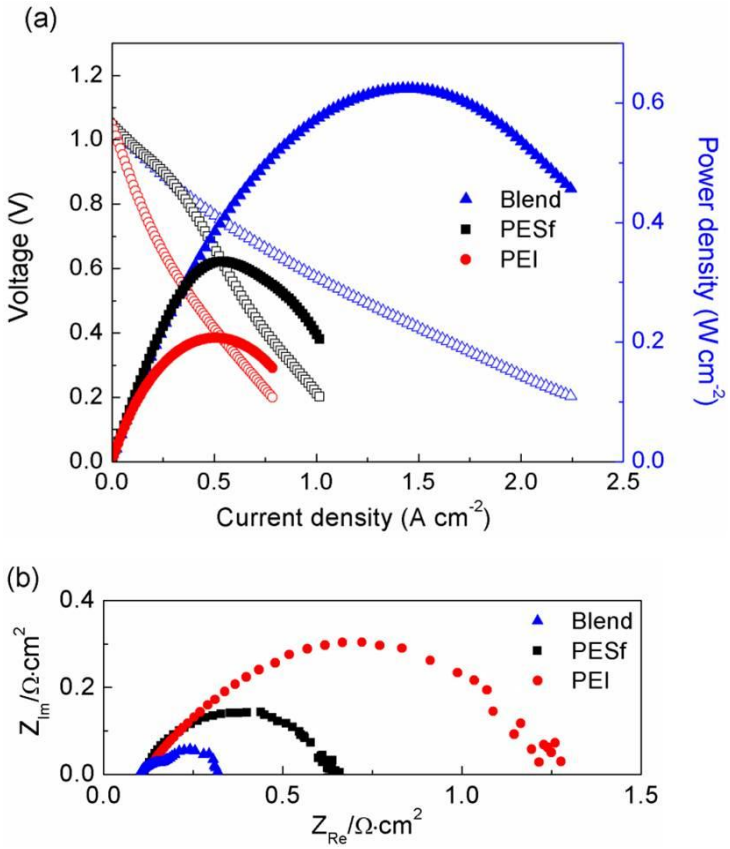

Figure 6.4 Current-voltage and power density curves (a) and impedance spectra (b) for cells fabricated with different polymer binder, tested at 750 ^{o}C.

6.4 SUMMARY

PESf-PEI polymer blend was employed to fabricate NiO-YSZ anode support for MT-SOFCs. Tubular samples fabricated with PESf-PEI polymer blend shows distinctly porous inner surface and microstructure with continuous gradient porosity. XPS analysis shows that NiO-YSZ anode support does not contain observable sulfide impurity when using either PESf or PESf-PEI polymer blend as polymer binder. Comparing with the cells fabricated with PEI and PESf, cells based on the novel microstructured anode fabricated with PESf-PEI polymer blend show much higher cell power output, and the cell power density reached 630 $mWcm^{-2}$ at 750 ^{o}C using hydrogen as fuel. The enhanced cell performance indicates that adopting blend polymer as binder is a promising strategy for SOFC anode fabrication.

CHAPTER7 FUTURE WORK

7.1 BACKGROUND

Solid oxide fuel cell (SOFC) has attracted many attentions due to its high energy conversion efficiency, low emission and flexible fuel selection [1]. In the past decades, several configurations of SOFC have been developed such as electrolyte-supported, cathode-supported and anode-supported SOFC. Among them, the anode-supported SOFC has been extensively investigated due to its high performance and lower operation temperature [135]. However, with the thick anode layer, the polarization resistance arising from the gas transportation in the porous anode will be increased significantly. Therefore, the anode microstructure should be optimized. Previously, anode with graded microstructure was developed [129], the coarser microstructure close to the fuel gas side can ensure a fast gas diffusion, while the layer with lower porosity, which adjacent to the electrolyte, can enlarge the triple-phase boundaries (TPB) for the anodic electrochemical reaction. To fabricate the anode with such graded microstructure, the phase inversion method, which was regarded as an efficient approach to fabricate the polymeric membrane [26], has been adopted for the SOFC, especially the micro-tubular SOFC (MT-SOFC) fabrication [55]. Via the phase inversion method, symmetrical microstructure consists of finger-like pores and sponge-lie pores can be formed. It is believed that the finger-like pores can function as a set of microchannels then facilitate

the gas diffusion to the active site in the sponge-like region of the anode. Based on the asymmetric microstructure, the cell performance has been significantly improved, Othman *et. al.* [59] claimed a peak power density of 2.23 Wcm^{-2} at 600^{o}C for the MT-SOFC with a LSCF-CGO/CGO/NiO-CGO configuration and ascribed the enhancement of the electrochemical performance to the unique microstructure obtained through the phase inversion method. Although it has been experimentally proved that the anode with asymmetric microstructure can effectively increase the electrochemical performance of the SOFC [59]. There is still no quantitive analysis that can directly show the advantage of the asymmetric microstructured anode over the conventional anode with homogonous pore distribution.

In this chapter, anode supports with asymmetric and homogenous microstructure were fabricated by the phase inversion method respectively. Cells fabricated based on these two types of anode supports were tested at 750 ^{o}C using several fuel gas with different hydrogen partial pressure. The performance of the cells was modeled and various parameters were achieved by fitting the I-V curve. The effect of the anode microstructure on the cell performance was discussed.

7.2 EXPERIMENTAL

The tubular anode supports were fabricated by the phase inversion method [77]. NiO and YSZ powders were fully mixed in the weight ratio of 6:4 and ball milled using ethanol as mill media for more than 24 hours then dried. The polymer binder PESf was dissolved into the NMP solvent (1:7 in weight ratio), then the prepared NiO-YSZ powders were dispersed into the polymer solution (1:1 in weight ratio) and also ball milled for 24 hours to achieve the homogenous casting slurry. Water was selected as the

non-solvent in the external coagulant, two types of anode supports were prepared by triggering the precipitation process at different temperatures. At room temperature (28^{o}C), tube with asymmetrical microstructure was prepared, while at 85^{o}C, anode support with homogenous distributed porosity was obtained. Cells fabricated based on the two types of cells were denoted as cell-a and cell-b respectively. The prepared tubes were pre-sintered at 1200 ^{o}C for 2 hours to obtain enough mechanical strength for the electrolyte fabrication. The YSZ thin film was deposited on the pre-sintered tubular samples using dip-coating method then sintered at 1450 ^{o}C for 5 hours to achieve the dense electrolyte. The $(La_{0.80}Sr_{0.20})_{0.95}MnO_{3-x}$ (LSM, Fuelcellmaterials, USA)-YSZ composite cathode was fabricated by brush painting method and sintered at 1100 ^{o}C for 2 hours. The microstructure of the prepared anode supports was examined by SEM (Zeiss Ultra plus FESEM). The cell measurement was carried out at 750 ^{o}C at 1 atm total pressure and constant flow rate (40 SCCM) of the hydrogen or mixture hydrogen fuel. The cell performance was measured using fuel gas with different hydrogen partial pressures (97 vol%, 72.8 vol%, 48.5 vol%, 24.3 vol%, 12.1 vol%), the fuel gas contains 3vol% H_2O and the balance gas is nitrogen. The current-voltage (I-V) curve of the two types of cells was measured at different hydrogen partial pressure by multi-channel VersaSTAT (Princeton Applied Research).

7.3 RESULT AND DISCUSSION

7.3.1 Characterization of the anode supported MT-SOFC

Figure 7.1 shows microstructure of the two types of anode supports, Figure 7.1 (a) is the anode support fabricated at room temperature, the typical asymmetric microstructure consisting of finger-like layer and sponge-like layer can be seen. While, for Figure 7.1 (b),

the anode prepared at higher temperature has a microstructure with homogenously distributed porosity. Similar result has been reported by Wang *et.al.* [81], higher precipitation temperature eliminates the formation of the macrovoids during the phase separation process. The measured I-V curve and current power density (I-P) curve of cell-a and cell-b are shown from Figure 7.2 to Figure 7.3, respectively. For both cells, with the diluted fuel gas, the open circuit voltage (OCV) decreases and the peak power density decreases as well. It can also be seen that with the same fuel gas composition, cell-a shows better cell performance than cell-b.

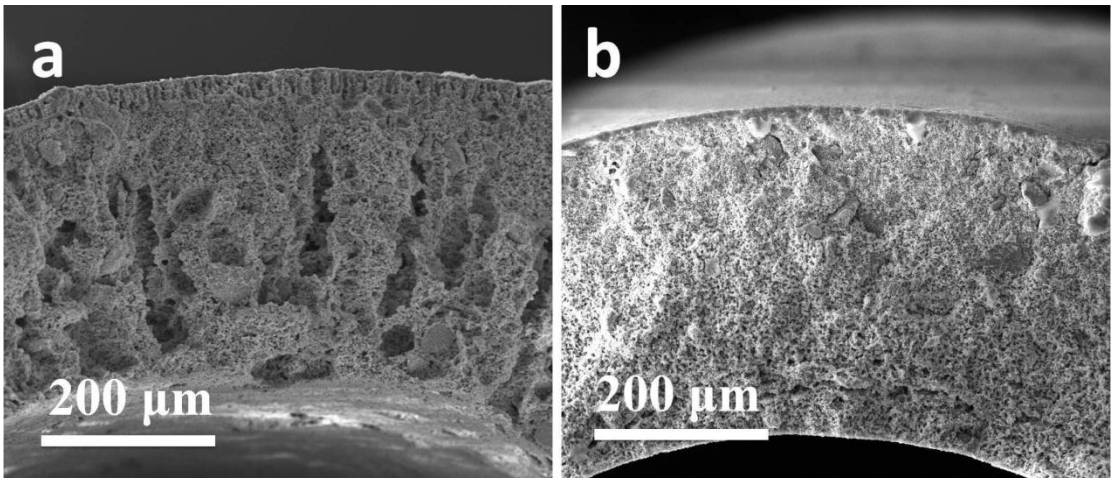

Figure 7.1 The SEM picture of pre-sintered anode supports fabricated at room temperature (a) and 85 ^{o}C (b).

7.3.2Polarization model

The relationship of current density (i) and the operating cell voltage (V_c) can be expressed as:

$$V_c = V_0 - iR_i - \eta_{act} - \eta_{a,conc} - \eta_{c,conc} - \eta_{leak} \qquad (7.1)$$

Where i is the current density (Acm^{-2}), R_i is the area specific ohmic resistance (Ωcm^2), V_o is the theoretical OCV (V), η_{act} is the activation polarization (V), $\eta_{a,conc}$ and $\eta_{c,conc}$ are the anodic and cathodic polarization (V) respectively. η_{leak} is the overpotential resulting from

the imperfect sealing (V).

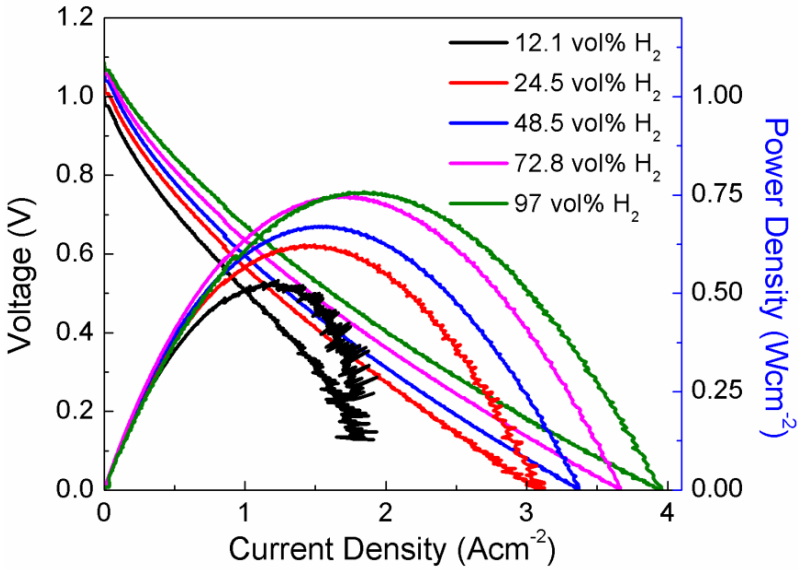

Figure 7.2 The current density-voltage (I-V) curve and current density-power density (I-P) curve of cell-a measured at different anodic atmosphere.

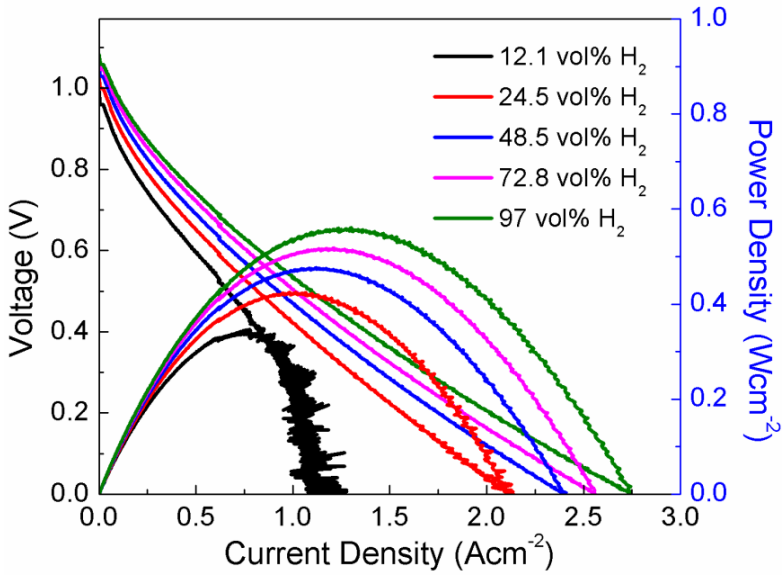

Figure 7.3 The current density-voltage (I-V) curve and current density-power density (I-P) curve of cell-b measured at different anodic atmosphere.

The main contribution of R_i is believed to be the ohmic resistance of the electrolyte, it

also includes the ohmic resistance of the electrodes and contact resistance generating from the interface between each layer of the SOFC.

The V_o can be calculated by the Nernst equation, and the calculated result and the measured value are shown in Figure 7.4, the discrepancy between the theoretical voltage and the measured OCV is believed to result from the imperfect sealing, which is described as η_{leak} in Ep. 7.1.

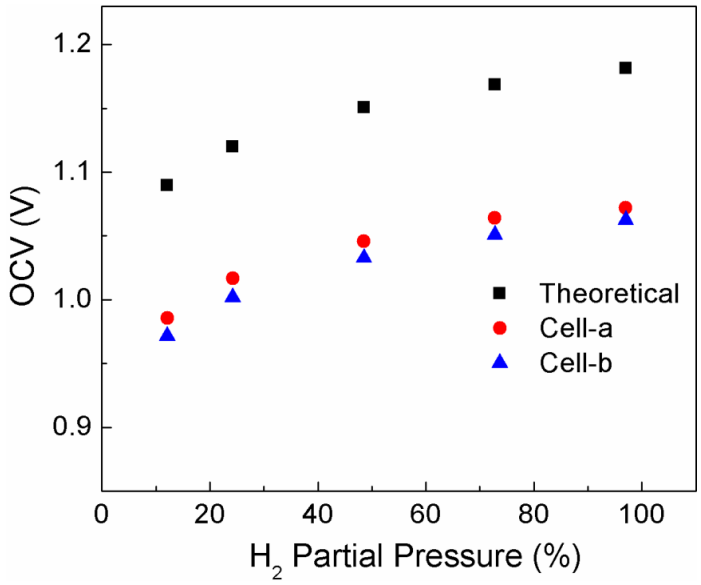

Figure 7.4 The theoretical voltage of SOFC at 750°C with different anodic atmosphere and measured OCV of cell-a and cell-b.

The activation polarization (η_{act}) arises from the charge transfer at the interface of the electrodes and electrolyte, the relationship between activation polarization and current density can be described by the Butler-Volmer equation

$$i = i_0 \exp\left(\frac{\alpha n \eta_{act} F}{RT}\right) - i_0 \exp\left(-\frac{(1-\alpha) n \eta_{act} F}{RT}\right) \qquad (7.2)$$

Where F is the Faraday constant, R is the universal gas constant, i_0 is the exchange current density, α is the transfer coefficient, n is the number of the electrons involving in the basic reaction of the SOFC operation. In this work, the electron transferred per

reaction is 1. For the transfer coefficient, a symmetrical activation barrier has been proposed by Chen [15] and the transfer coefficient is assigned to be 0.5. Then, the equation can be expressed as

$$i = i_0 \exp\left(\frac{0.5\eta_{act}F}{RT}\right) - i_0 \exp\left(-\frac{0.5\eta_{act}F}{RT}\right) \qquad (7.3)$$

To rewrite the equation, an equation with ($0.5\eta_{act}F/RT$) as the function can be achieved.

$$\left[\exp\left(\frac{0.5\eta_{act}F}{RT}\right)\right]^2 - \left(\frac{i}{i_0}\right)\left[\exp\left(\frac{0.5\eta_{act}F}{RT}\right)\right] - 1 = 0 \qquad (7.4)$$

Solving the equation, the result is given as

$$\exp\left(\frac{0.5\eta_{act}F}{RT}\right) = \frac{1}{2}\left[\left(\frac{i}{i_0}\right) + \sqrt{\left(\frac{i}{i_0}\right)^2 + 4}\right] \qquad (7.5)$$

Further, the relationship between the activation polarization and the current density can be expressed as [136]

$$\eta_{act} = \frac{2RT}{F}\ln\left\{\frac{1}{2}\left[\left(\frac{i}{i_0}\right) + \sqrt{\left(\frac{i}{i_0}\right)^2 + 4}\right]\right\} \qquad (7.6)$$

The η_{act} in this equation represent the activation polarization contributed from both the cathode and anode.

The concentration polarization is generated by the mass transportation through the porous electrodes. It can be caused by operating at high current density or the insufficient porosity of the electrode. In this instant, the depletion of the reactant and the accumulation of the product species in the electrode active layer lead to the performance loss.

The cathodic concentration polarization can be expressed as [16]:

$$\eta_{c,conc} = -\frac{RT}{4F}\ln\left(\frac{p'_{o_2(i)}}{p^0_{o_2}}\right) = -\frac{RT}{4F}\ln\left(1-\frac{i}{i_{cs}}\right) \qquad (7.7)$$

Where $P^0_{o_2}$ is the oxygen partial pressure outside of the cathode surface and $P'_{o_{2(i)}}$ is the oxygen partial pressure at the interface between the cathode and electrolyte. i_{cs} is the cathode limit current density, when the current density reaches to the i_{cs} , the $P'_{o_{2(i)}}$ is zero. The i_{cs} can be describe as [16]:

$$i_{cs} = \frac{4FP^0_{O_2}D^{eff}_{O_2-N_2}}{\left(\frac{P-P^0_{O_2}}{P}\right)RTl_c} \qquad (7.8)$$

According to the equation, it can be seen that the cathode limit current density is determined by the oxygen partial pressure ($P^0_{o_2}$), total pressure of cathode side (P), thickness of cathode layer (l_c) and $D^{eff}_{O_2-N_2}$ is the effective binary diffusivity of O_2 in O_2 and N_2 system. In this work, it is assumed that the cathode limit current density will not be affected when changing the anodic atmosphere, therefore, the cathodic concentration polarization should be a constant for each cells tested at different fuel compositions.

For the anodic concentration polarization, it can be expressed as:

$$\eta_{a,conc} = -\frac{RT}{2F}\ln\left(\frac{p'_{H_2(i)}p^0_{H_2O}}{p^0_{H_2}p'_{H_2O(i)}}\right) = -\frac{RT}{2F}\ln\left(1-\frac{i}{i_{as}}\right)+\frac{RT}{2F}\ln\left(1+\frac{p^0_{H_2}i}{p^0_{H_2O}i_{as}}\right) \qquad (7.9)$$

Where $P'_{H_{2(i)}}$ is the hydrogen partial pressure at the interface between anode and electrolyte, $P'_{H_2O_{(i)}}$ is the partial pressure of water vapor at the interface between anode and electrolyte, $P^0_{H_2}$ and $P^0_{H_2O}$ are the hydrogen partial pressure and the partial pressure of water vapor outside the anode, respectively. i_{as} is the anodic limit current density and can be described as

$$i_{as} = \frac{2FP^0_{H_2} D^{eff}_{H_2-H_2O-N_2}}{RTl_a} \qquad (7.10)$$

$D^{eff}_{H_2-H_2O-N_2}$ is the effective ternary diffusivity of H_2 in H_2, N_2 and H_2O system. l_a is the thickness of the anode.

In summary, the relationship of current density (i) and the operating cell voltage (V_c) can be rewritten as:

$$V_c = V_0 - iR_i - \frac{2RT}{F}\ln\left\{\frac{1}{2}\left[\left(\frac{i}{i_0}\right)+\sqrt{\left(\frac{i}{i_0}\right)^2+4}\right]\right\} + \frac{RT}{2F}\ln\left(1-\frac{i}{i_{as}}\right) - \frac{RT}{2F}\ln\left(1+\frac{p^o_{H_2} i}{p^o_{H_2O} i_{as}}\right) + \frac{RT}{4F}\ln\left(1-\frac{i}{i_{cs}}\right) - \eta_{leak} \qquad (7.11)$$

The measured I-V curve data were fitted using the Eq. 11, and then the value of R_i, i_0, i_{as} and i_{cs} can be obtained.

7.3.3 Evaluation of the electrochemical result

Figure 7.5 and Figure 7.6 show the cell test results and the fitting curves. The parameters achieved by the model fitting are listed in Table 7.1. Based on the calculated results, the two MT-SOFCs show the similar ohmic resistance value. The cathode limit current density value of the two cells is 87.29 Acm^{-2} (cell-a) and 1822 Acm^{-2} (cell-b) at all of the anodic atmosphere, respectively. According to Ep. 7.7, the cathodic concentration polarization of the two cells can be calculated and the result is shown in Figure 7.7, it can be seen that the contribution of the cathodic concentration polarization is negligible due to their extremely small value.

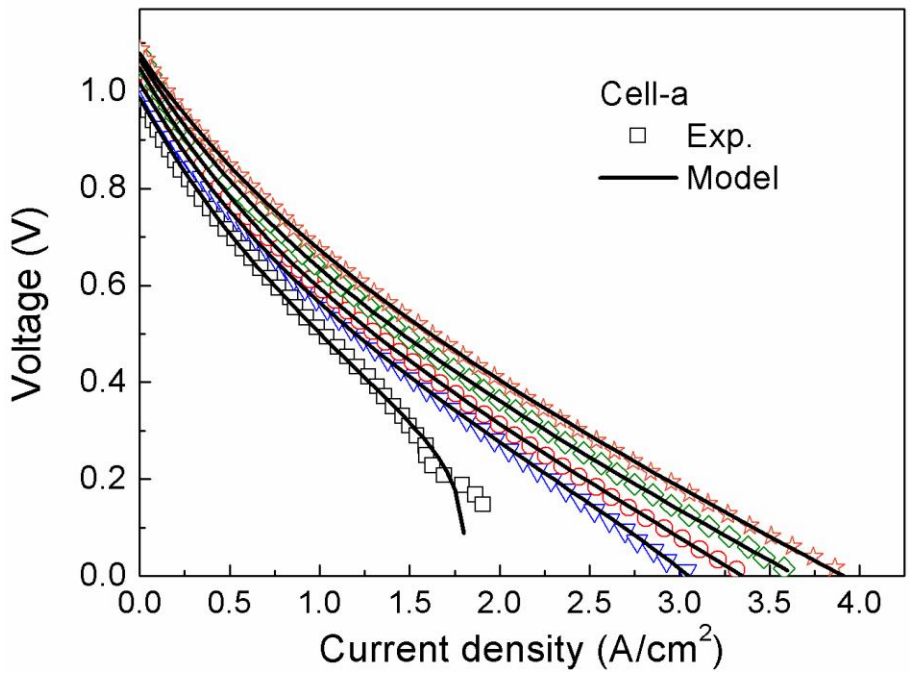

Figure 7.5 The measured and fitted I-V curve of cell-a.

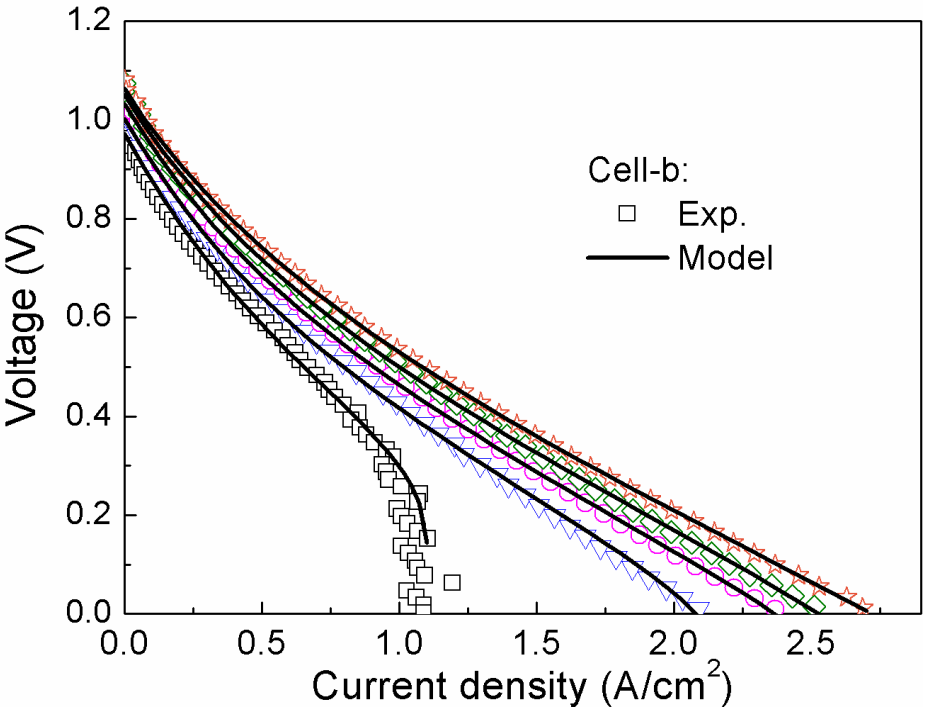

Figure 7.6 The measured and fitted I-V curve of cell-b.

Table 7.1 Curve-fitting result of cell-a and cell-b tested at 750 ^{o}C with different fuel gas

anode gas H_2 Vol%	i_{cs}, Acm^{-2} cell-a/ cell-b	i_0, Acm^{-2} cell-a/ cell-b	i_{as}, Acm^{-2} cell-a/ cell-b	R_i, Ωcm^2 cell-a/ cell-b	η_{leak},V cell-a/ cell-b
97	87.29/ 1822	0.3705/ 0.2402	6.613/ 3.368	0.1248/ 0.153	0.1025/ 0.1179
72.8	87.29/ 1822	0.3047/ 0.2126	5.679/ 2.902	0.1248/ 0.153	0.1025/ 0.1179
48.5	87.29/ 1822	0.2576/ 0.1784	4.432/ 2.689	0.1248/ 0.153	0.1025/ 0.1179
24.5	87.29/ 1822	0.2406/ 0.1499	3.456/ 2.214	0.1248/ 0.153	0.1025/ 0.1179
12.1	87.29/ 1822	0.2232/ 0.1405	1.809/ 1.107	0.1248/ 0.153	0.1025/ 0.1179

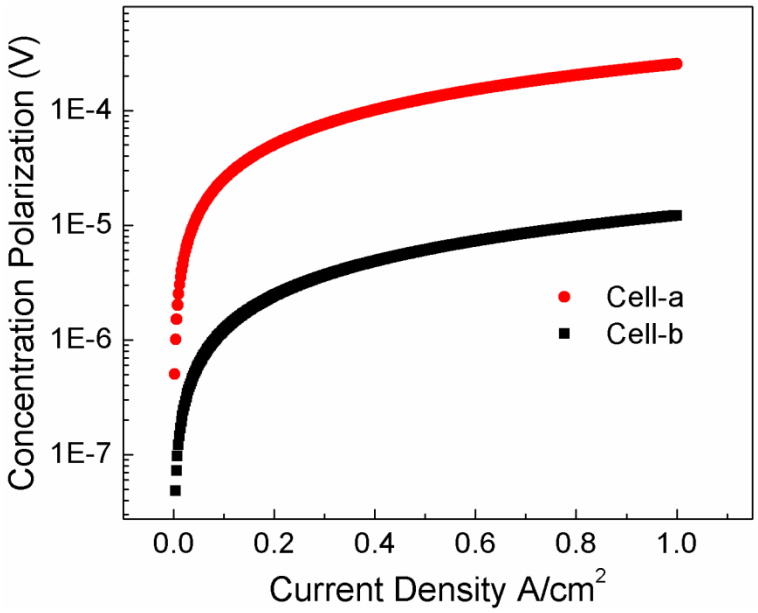

Figure 7.7 The cathodic concentration polarization of cell-a and cell-b

The anode limit current density is believed to be affected by the anode microstructure. From the fitting result, it can be seen that cell-a with the asymmetric microstructured anode shows larger anode limit current density value than cell-b, when using hydrogen or

hydrogen mixture as the fuel gas. For the cell tested at diluted hydrogen gas, the anodic concentration polarization can be calculated by Ep. 7.9. Figure 7.8 shows the anodic concentration polarization of cell-a and cell-b operated at fuel gas with 12.1 vol% hydrogen partial pressure. It can be seen that cell-a shows smaller anodic activation polarization than cell-b when using diluted hydrogen gas at high current density.

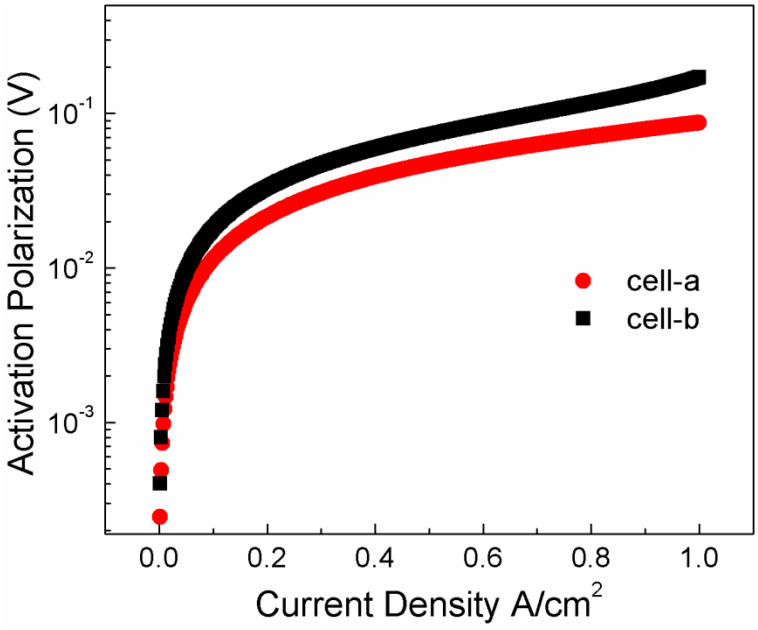

Figure 7.8 The anodic activation polarization of cell-a and cell-b with 12.1 vol% hydrogen as fuel gas.

The exchange current density obtained from the model using the Butler-Volmer equation is contributed by the anodic and cathodic activation polarization. At high hydrogen partial pressure, the activation polarization is dominated by the cathodic contribution and the anodic contribution is negligible. Therefore, $i_o \approx i_c$, $i_c \geq i_a$ and the value of the activation polarization can be equivalent to the cathodic activation polarization, when using 97 vol% hydrogen as the fuel gas. Then, as the hydrogen partial pressure drops, the anodic activation polarization increases while the cathodic activation polarization will not be affected. The charge transfer resistance can be expressed as

$$R_{ct} = \left[\frac{RT}{Fi_0} \right] \qquad (7.12)$$

The total charge transfer resistance of the cell can be regarded as a series connected cathode charge-transfer resistance, $R_{ct,c}$, and anodic charge-transfer resistance, $R_{ct,a}$ and can be described as

$$R_{ct} = R_{ct,c} + R_{ct,a} \qquad (7.13)$$

Thus, when using 97 vol% hydrogen as fuel gas, the cathodic activation polarization can be calculated by Ep7.12. And then, for different fuel gas composition, the anodic activation polarization can be calculated based on Ep7.13, the result is shown in Table 7.2.

Table 7.2 Charge-transfer resistances at various fuel compositions.

$p^o_{H_2}$/atm	Cell	$R_{ct,c}/\Omega cm^2$	$R_{ct,a}/\Omega cm^2$	$R_{ct}/\Omega cm^2$
0.97	Cell-a	0.238	0	0.238
	Cell-b	0.367	0	0.367
0.7275	Cell-a	0.238	0.0513	0.2893
	Cell-b	0.367	0.0476	0.4236
0.485	Cell-a	0.238	0.1041	0.3421
	Cell-b	0.367	0.1271	0.4941
0.2425	Cell-a	0.238	0.1283	0.3663
	Cell-b	0.367	0.2210	0.588
0.12125	Cell-a	0.238	0.1569	0.3949
	Cell-b	0.367	0.2603	0.6273

According to the calculated result, it can be seen that cell-a has smaller exchange current density than cell-b at different fuel gas composition. As mentioned above, when using 97vol% hydrogen as the fuel gas, the total activation polarization is mainly attributed by the cathode. Therefore, the result shows that cell-a shows relatively better cathode performance than cell-b. For the anode, it can be seen that as the hydrogen partial pressure decreases, the discrepancy between cell-a and cell-b increases. It indicates that

the anode with asymmetric microstructure shows advantages over the homogenous microstructured anode when using diluted hydrogen as fuel gas.

7.4 SUMMARY

MT-SOFCs with different microstructure were fabricated by phase inversion method at different temperature. The I-V curves measured at different anodic atmosphere were fitted by a polarization model. The contribution of cathode and anode of the cells was separated. Based on the calculated result, it can be concluded that the anode support with asymmetric microstructure can provide decreased anodic concentration polarization as well as activation polarization.

REFERENCE

[1] E.P. Murray, T. Tsai, S.A. Barnett, Nature, 400 (1999) 649-651.

[2] http://science.nasa.gov/science-news/science-at-nasa/2003/18mar_fuelcell/

[3] M. Mogensen, N. M. Sammes, G. A. Tompsett, Solid State Ionics, 129 (2000) 63-94.

[4] B.C.H. Steele, Solid State Ionics, 129 (2000) 95-110.

[5] P.N. Huang, A. Petric, J. Electrochem. Soc., 134 (1996) 1644-1648.

[6] K. Huang, R.S. Tichy ,J.B. Goodenough, J. Am. Ceram. Soc., 81 (1998) 2565-2575.

[7] M. Juhl, S. Primdahl, C. Manon, M. Mogensen, J. Power Sources, 61 (1996) 173-181.

[87] T. Kobayashi, M. Rikukawa, K. Sanui, N. Ogata, Solid State Ionics, 106 (1998) 255-261.

[9] S. Zha, P. Tsang, Z. Cheng, M. Liu, J. Solid State Chem., 178 (2005) 1844-1850.

[10] D.H. Archer, L. Elikan, R.L. Zahradnik, in: B.S. Baker (Ed.), Hydrocarbon Fuel Cell Technologies, Academic Press, New York, 1965.

[11] K. Kendall, Proceedings of the International Forum on Fine Ceramics. International Forum on Fine Ceramics, Japan Fine Ceramics Center, Nagoya, 1992.

[12] K. Kendall, M. Prica, 1st European SOFC Forum, Luzern, Switzerland, 1994.

[13] Y. Liu, S.I. Hashimoto, H. Nishino, K. Takei, M. Mori, T. Suzuki, Y. Funahashi, J. Power Sources, 174 (2007) 95-102.

[14] K.S. Howe, G.J. Thompson, K. Kendall, J. Power Sources, 196 (2011) 1677-1686.

[15] S.H Chan, K.A . Khor, Z.T. Xia, J. Power Sources, 93 (2001) 130-140.

[16]J.W. Kim, A.V. Virkar, K.Z. Fung, K. Mehta, S.C.Singhal, J. Electrochem. Soc.,146 (1999) 69-78.

[17] Y. Jiang, A.V. Virkar, J. Electrochem. Soc. 150 (2003) A942-A951.

[18] http://physics.mff.cuni.cz/kfpp/povrchy/method/fc-principles

[19] Feng Zhao, Anil V. Virkar, J. Power Sources, 141 (2005) 79-95.

[20] P. Holtappels, C. Sorof, M.C. Verbraeken, S. Rambert, U. Vogt, FUEL CELLS, 06 (2006) 113-116.

[21] C.M. An, J.H. Song, I. Kang, N. Sammes, J. Power Sources, 195 (2010) 821-824.

[22] C. Jin, C. Yang, F. Chen, J. Membr. Sci., 363 (2010) 250-255.

[23] Y. Chen, J. Bunch, T. Li, Z. Mao, F. Chen, J. Power Sources, 213 (2012) 93-99.

[24] C. Yang, C. Jin, F. Chen, Electrochem. Commun., 12 (2010) 657-660.

[25]S. Loeb, S. Sourirajan, Saline Water Conversion—II, Advances in Chemistry Series Vol. 38, American Chemical Society, 1963, Ch. 9.

[26] S.P. Deshmukh, K. Li, J. Membr. Sci., 150 (1998) 75-85.

[27] W. He, H. Huang, J. Gao, L. Winnubst, C. Chen, J. Membr. Sci., 452 (2014) 294-299.

[28] W. Kools, PhD thesis, Chemical Engineering, University of Twente (1998)

[29] H. Strathmann, K. Kock, P. Amar, R.W. Baker, Desalination, 16 (1975) 179-203.

[30] C.A. Smolders, A.J. Reuvers, R.M. Boom, I.M. Wienk, J. Membr. Sci., 73 (1992) 259-275.

[31] M. Ulbricht, Polymer, 47 (2006) 2217-2262.

[32] I.C. Kim, H.G. Yoon, K.H. Lee, J. Appl. Polym. Sci., 84 (2002) 1300-1307.

[33] H.J. Kim, R.K. Tyagi, A.E. Fouda, K. Jonasson, J. Appl. Polym. Sci., 62 (1996) 621-629.

[34] Q.Z. Zheng, P. Wang, Y.N. Yang, D.J. Cui, J. Membr. Sci., 286 (2006) 7-11.

[35] M. Amirilargani, E. Saljoughi, T. Mohammadi, M.R. Moghbeli, Polym. Eng. Sci., 50 (2010) 885-893.

[36] D. Y. Xing, N. Peng, T. S. Chung, Ind. Eng. Chem. Res. 49 (2010) 8761–8769

[37] I.C. Kim, K. H. Lee, J. Appl. Polym. Sci., 89 (2003) 2562–2566.

[38] B. Wang, Z. Lai, J. Membr. Sci., 405–406 (2012) 275–283.

[39] M.L. Yeow, 1, Y. Liu, K. Li, J. Membr. Sci., 258 (2005) 16–22.

[40] M. Zeni, R. Riveros , J.F. de Souza, K. Mello , C. Meireles , G.R. Filho, Desalination, 221 (2008) 294–297.

[41] D.J. Lin, C.L. Chang, C.K. Lee, L.P. Cheng, Eur. Polym. J., 42 (2006) 2407–2418.

[42] S. Mei, C. Xiao, Xi. Hu, J. Appl. Polym. Sci., 120 (2011)557–562.

[43] L. Yu, F. Yang, M. Xiang, RSC Adv. 4 (2014) 42391–42402.

[44] Z.L. Xu, F. A. Qusay, J. Membr. Sci., 233 (2004) 101–111.

[45] A. Deng, A. Chen, S. Wang, Y Li, Y. Liua, X. Cheng,Z. Zhao, D. Lin, J. Supercrit. Fluids, 77 (2013) 110–116.

[46] R. Ruaan, T. Chang, D. Wang, J. Polym. Sci., Part B: Polym. Phys., 37 (1999) 1495–1502.

[47] M. A. Frommer, R. M. Messalem, Ind. Eng. Chem. Prod. Res. Develop., 12 (1973) 328-333.

[48] A. Bottino, G. C. Roda, G. Capannelli, S. Munari, J. Membr. Sci., 57 (1991) l-20.

[49] A.J. Reuvers, C.A. Smolders, J. Membrane Sci., 34 (1987) 67-86.

[50] Y. Zhang, H. Wang, B. Yan, Y. Zhang, P. Yin, G. Shen, R. Yu J. Mater. Chem., 18 (2008) 4442–4449.

[51] J.G. Wijmans, H.J.J. Rutten, and C.A. Smolders, J. Polym. Sci. Polym. Phys. Ed., 23 (1985)1941-1955.

[52] C. Gonzalez-Obeso, W. Song, M.A. Rodriguez-Perez, Mater Sci. Forum, 730-732 (2013) 44-49.

[53] T. Suzuki, Y. Funahashi, T. Yamaguchi, Y. Fujishiro, M. Awano, Solid State Ionics, 180 (2008) 546-549.

[54] N. Yang, X. Tan, Z. Ma, J. Power Sources, 183 (2008) 14-19.

[55] C. Yang, W. Li, S. Zhang, L. Bi, R. Peng, C. Chen, W. Liu, J. Power Sources 187 (2009) 90-92.

[56] X. Zhang, B. Lin, Y. Ling, Y. Dong, G. Meng, X. Liu, J. Alloys Compd. 497 (2010) 386-389.

[57] X. Zhang, B. Lin, Y. Ling, Y. Dong, G. Meng, X. Liu, Int. J. Hydrogen Energy, 35 (2010) 8654-8662.

[58] D. Zhou, S. Peng, Y. Wei, Z. Li, H. Wang, J. Alloys Compd. 523 (2012) 134–138.

[59] M.H. D.Othman, N. Droushiotis, Z. Wu, G. Kelsall ,K. Li, Adv. Mater. 23 (2011) 2480-2483.

[60] S. Peng, D. Zhou, Y. Wei, Z. Li, H. Wang, J. Membr. Sci.,417–418 (2012) 80-86.

[61] D. Ding, Z. Liu, L. Li, C. Xia, Electrochem. Commun., 10 (2008) 1295-1298.

[62] K. Kendall, M. Palin, J. Power Sources, 71 (1998) 268-270.

[63] Y. Du, N.M. Sammes, G.A. Tompsett, D. Zhang, J. Swan, M. Bowden, J. Electrochem. Soc., 150 (2003) A74-A78.

[64] T. Suzuki, T. Yamaguchi, Y. Fujishiro, M. Awano, J. Power Sources, 160 (2006) 73-77.

[65] X. Tan, N. Liu, B. Meng, S. Liu, J. Membr. Sci., 378 (2011) 308-318.

[66] X. Dong, W. Jin, N. Xu, K. Li, Chem. Commun., 47 (2011) 10886-10902.

[67] T. Suzuki, Z. Hasan, Y. Funahashi, T. Yamaguchi, Y. Fujishiro, M. Awano, Science, 325 (2009) 852-855.

[68] F. Zhao, C. Jin, C. Yang, S. Wang, F. Chen, J. Power Sources, 196 (2011) 688-691.

[69] C. Jin, J. Liu, L. Li, Y. Bai, J. Membr. Sci., 341 (2009) 233-237.

[70] T. H. Young, L. W. Chen, Desalination, 103(1995) 233-247.

[71] M.T. So, F.R. Eirich, H. Strathmann, R.W. Bake, J. Polym. Sci. Polym. Lett. Ed. 11 (1973) 201

[72] B.E. Poling, J.M. Prausnitz, J.P. O'Connell, The properties of Gases and Liquids, 5th edition, Mc raw-Hill, New York, 2001, Ch. 11, 24.

[73] B.C.H. Steele, Nature, 400 (1999) 619-621.

[74] N.Q. Minh, J. Am. Ceram. Soc., 76 (1993) 563-588.

[75] S.C. Singhal, Solid State Ionics, 152-153 (2002) 405-410.

[76] I.P. Kilbride, J. Power Sources, 61 (1996) 167-171.

[77] C. Yang, C. Jin, F. Chen, Electrochim. Acta, 56 (2010) 80-84.

[78] B. He, Y. Ling, J. Xu, L. Zhao, J. Cheng, J. Power Sources, 258 (2014) 391-394.

[79]T. Li, Z. Wu, K. Li, J. Power Sources, 251 (2014) 145-151.

[80] X. Meng , X. Gong, Y. Yin, N. Yang, X. Tan, Z. F. Ma, Int. J. Hydrogen Energy, 38 (2013) 6780-6788.

[81] H. Wang, J. Liu, Int. J. Hydrogen Energy, 37 (2012) 4339-4345.

[82] S. Liu, K. Li, R. Hughes, Ceram. Int., 29 (2003) 875-881.

[83] S. Liu, X. Tan, K. Li, R. Hughes, J. Membr. Sci., 193 (2001) 249-260.

[84] B.F.K. Kingsbury, K. Li, J. Membr. Sci., 328 (2009) 134-140.

[85] J. Barzin, B. Sadatnia, J. Membr. Sci., 325 (2008) 92-97.

[86] M.H.D. Othman, N. Droushiotis, Z. Wu, G. Kelsall, K. Li, J. Power Sources, 205 (2012) 272-280.

[87] C. Chen, M. Liu, L. Yang, M. Liu, Int. J. Hydrogen Energy, 36 (2011) 5604-5610.

[88] T. Talebi, M. H. Sarrafi, M. Haji, B. Raissi, A. Maghsoudipour, Int. J. Hydrogen Energy, 35 (2010) 9440-9447.

[89] K. Chen, X. Chen, Z. Lu, N. Ai, X. Huang, W. Su, Electrochim. Acta, 53 (2008) 7825-7830.

[90] D. Panthi, A. Tsutsumi, Sci. Rep., 4 (2014) 5754-5759.

[91] R. Barfod, M. Mogensen, T. Klemensø, A. Hagen, Y. L. Liu, P. V. Hendriksen, J. Electrochem. Soc.,154 (2007) B371-B378.

[92] K. Hendrix, M. Vaneynde, G. Koeckelberghs, I.F.J. Vankelecom, J. Membr. Sci. 447 (2013) 96-106.

[93] X. Huang, J. Power Sources, 216 (2012) 216-221.

[94] J. Liu, S. Zhang, W. Wang, J. Gao, W. Liu, C. Chen, J. Power Sources 217 (2012) 287-290.

[95] R.M. Boom, I.M. Wienk, Th. van den Boomgaard, C.A. Smolders, J. Membr. Sci., 73 (1992) 277-292.

[96] D. Wang, K. Li, W.K. Teo, J. Membr. Sci., 178 (2000) 13-23.

[97] M. Han, S. Nam, J. Membr. Sci., 202 (2002) 55-61.

[98] B. Chakrabarty, A.K. Ghoshal, M.K. Purkait, J. Membr. Sci., 309 (2008) 209-221.

[99] J. H. Kim, K. H. Lee, J. Membr. Sci., 138 (1998) 153-163.

[100] W. Yin, B. Wen, X. Meng, X. Tan, J. Alloys Compd. 476 (2009) 566-570.

[101] N. Droushiotis, F.D. Grande, M.H.D. Othman, K. Kanawka, U. Doraswami, I.S. Metcalfe, K. Li, G. Kelsall, Fuel Cells 14 (2014) 200-211.

[102] C.W. Yao, R.P. Burford, A.G. Fane, C.J.D. Fell, J. Membr. Sci. 38 (1988) 113-125.

[103] R.M. Boom, Th. van den Boomgaard, C.A. Smolders, Macromolecules, 27 (1994) 2034-2040.

[104] R. M. Boom, H. W. Reinders, H. H. W Rolevink, Th. van den Boomgaard, C. A. Smolders, Macromolecules, 27 (1994) 2041-2044.

[105] H. Ohya, S. Shiki, H. Kawakami, J. Membr. Sci., 326 (2009) 293-302.

[106] P.C. Hidber, T.J. Graule, L.J. Gauckler, J. Eur. Ceram. Soc., 17 (1997) 239-249.

[107] U. Paik, V. A. Hackley, H.W. Lee, J. Am. Ceram. Soc., 82(1999) 833-840.

[108] B. Tang, D. Wu, T. Xu, J. Appl. Polym. Sci., 98 (2005) 2414-2421.

[109] H. Wang, C. Tablet, J. Caro, J. Membr. Sci., 322 (2008) 214-217.

[110]T. Liu, C. Ren, S. Fang, Y. Wang, F. Chen, ACS. Appl. Mater. Interfaces, 6 (2014) 1 8853-18860.

[111] C. Ren, T. Liu, Y. Mao, P. Maturavongsadit, J. A. Luckanagul, Q. Wang, F. Chen, Electrochim. Acta, 149 (2014) 159-166.

[112] M.H.D. Othman, N. Droushiotis, Z. Wu, G. Kelsall, K. Li, J. Power Sources, 196 (2011) 5035-5044.

[113] Y. Lin, R. Ran, Y. Zheng, Z. Shao, W. Jin, N. Xu, J. Ahn, J. Power Sources, 180 (2008) 15-22.

[114] Y. Lin, C. Su, C. Huang, J. S. Kim, C. Kwak, Z. Shao, J. Power Sources, 197 (2012) 57-64.

[115] Y. Lin, R. Ran, D. Chen, Z. Shao, J. Power Sources, 195 (2010) 4700-4703.

[116]W. Li, J. Liu, C. Chen, J. Membr. Sci., 340 (2009) 266-271.

[117] N. Droushiotis, A. Torabi, M.H.D. Othman T.H. Etsell , G.H. Kelsall, J. Appl. Electrochem., 42 (2012) 517-526.

[118] C. Buysse, A. Kovalevsky, F. Snijkers, A. Buekenhoudt, S. Mullens, J. Luyten, J. Kretzschmar, S. Lenaerts, J. Membr. Sci., 359 (2010) 86-92.

[119] L. Yang, S.Z. Wang, K. Blinn, M.F. Liu, Z. Liu, Z. Cheng, M.L. Liu, Science, 326 (2009) 126-129.

[120] K.D. Kreuer, Solid State Ionics, 97 (1997) 1 –15.

[121] E. Klein , J.K. Smith, Ind. Eng. Chem. Prod. Res. Develop., 11 (1972) 207-210.

[122] C. Mu, Y. Su, M. Sun, W. Chen, Z. Jiang, J. Membr. Sci., 350 (2010) 293-300.

[123] G. Bakeri, T. Matsuura, A. T. Ismail, J. Membr. Sci., 383 (2011) 159-169.

[124]T. S. Chung, Z. L. Xu. J. Membr. Sci., 147 (1998) 35-47.

[125] J.Y. Lai, F.C. Lin, C.C. Wang, D.M. Wang, J. Membr. Sci., 118 (1996) 49-61.

[126] A. Leo, S. Smart, S. Liu, J. C. D. da Costa, J. Membr. Sci. 368 (2011) 64-68.

[127] A.V. Virkar, J. Chen, C.W. Tanner, J.W. Kim, Solid State Ionics, 131 (2000) 189-198.

[128] H. Sumi, T. Yamaguchi, T. Suzuki, H. Shimada, K. Hamamoto, Y. Fujishiro, Electrochem. Commun.,49 (2014) 34-37.

[129] Z. Wang, N. Zhang, J. Qiao, K. Sun, P. Xu, Electrochem. Commun., 11 (2009) 1120-1123.

[130] Z. Wang, J. Qian, J. Cao, S. Wang, T. Wen, J. Alloys Compd., 437 (2007) 264-268.

[131] Y. Chen, Q. Liu, Z. Yang, F. Chen, M. Han, RSC Adv., 2 (2012) 12118-12121.

[132] L. Chen, M. Yao, C. Xia, Electrochem. Commun., 38 (2014) 114-116.

[133] Y. Zhang, M. Ni, C. Xia, F. Chen, J. Am. Ceram. Soc., 97 (2014) 2580-2589.

[134] G.C. Kapantaidakis, G.H. Koops, J. Membr. Sci., 204 (2002) 153-171.

[135] S. de Souza, S.J. Visco, and L.C. De Jonghe, Solid State Ionics, 98 (1997) 57-61.

[136] P. W. Li and M. K. Chyu, J. Heat Transfer, 127 (2005) 1344-1362.